Cell

Article

Sex-dependent effects in the aged melanoma tumor microenvironment influence invasion and resistance to targeted therapy

Graphical abstract

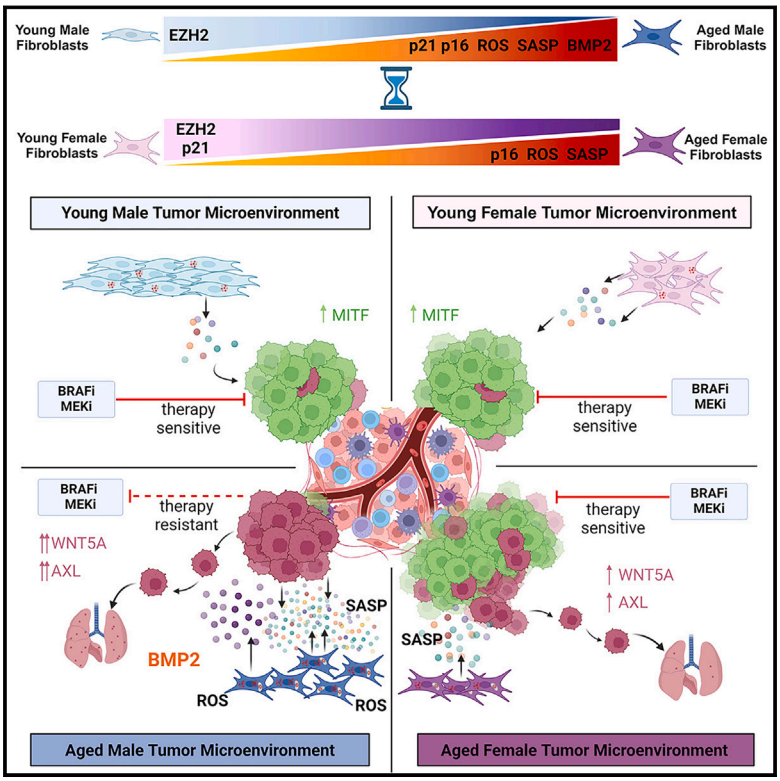

Highlights

- Skin fibroblasts show age- and sex-specific changes in proliferation and stress response
- Male fibroblasts age faster due to elevated ROS levels
- BMP2 is secreted in the aged male dermal microenvironment
- BMP2 promotes slow-cycling, invasive, targeted therapy-resistant melanoma tumors

Authors

Yash Chhabra, Mitchell E. Fane, Sneha Pramod, ..., Joel C. Sunshine, Hongkai Ji, Ashani T. Weeraratna

Correspondence

yash.chhabra@fccc.edu (Y.C.), aweerar1@jhu.edu (A.T.W.)

In brief

Aging-driven and sex-dependent molecular changes in skin fibroblasts drive the emergence of invasive and therapy-resistant melanomas in male mice.

Chhabra et al., 2024, Cell *187*, 6016–6034
October 17, 2024
https://doi.org/10.1016/j.cell.2024.08.013

CellPress

CellPress

Cell

Article

Sex-dependent effects in the aged melanoma tumor microenvironment influence invasion and resistance to targeted therapy

Yash Chhabra,[1,2,*] Mitchell E. Fane,[1,2] Sneha Pramod,[1] Laura Hüser,[1] Daniel J. Zabransky,[1,3] Vania Wang,[1] Agrani Dixit,[1] Ruzhang Zhao,[4] Edwin Kumah,[1] Megan L. Brezka,[1] Kevin Truskowski,[1,2] Asmita Nandi,[1] Gloria E. Marino-Bravante,[1] Alexis E. Carey,[1] Naina Gour,[5] Devon A. Maranto,[3] Murilo R. Rocha,[1] Elizabeth I. Harper,[1] Justin Ruiz,[1] Evan J. Lipson,[3] Elizabeth M. Jaffee,[3,6] Kristin Bibee,[7] Joel C. Sunshine,[7] Hongkai Ji,[4] and Ashani T. Weeraratna[1,3,8,*]

[1]Department of Biochemistry and Molecular Biology, Johns Hopkins Bloomberg School of Public Health, Baltimore, MD 21205, USA
[2]Cancer Signaling and Microenvironment, Fox Chase Cancer Center, Philadelphia, PA 19111, USA
[3]Department of Oncology, Sidney Kimmel Comprehensive Cancer Center, Johns Hopkins University, Baltimore, MD 21205, USA
[4]Department of Biostatistics, Johns Hopkins Bloomberg School of Public Health, Baltimore, MD 21205, USA
[5]Department of Neuroscience, Johns Hopkins University School of Medicine, Baltimore, MD 21205, USA
[6]The Cancer Convergence Institute, Johns Hopkins University School of Medicine, Baltimore, MD 21205, USA
[7]Department of Dermatology, Johns Hopkins University School of Medicine, Baltimore, MD 21287, USA
[8]Lead contact
*Correspondence: yash.chhabra@fccc.edu (Y.C.), aweerar1@jhu.edu (A.T.W.)
https://doi.org/10.1016/j.cell.2024.08.013

SUMMARY

There is documented sex disparity in cutaneous melanoma incidence and mortality, increasing disproportionately with age and in the male sex. However, the underlying mechanisms remain unclear. While biological sex differences and inherent immune response variability have been assessed in tumor cells, the role of the tumor-surrounding microenvironment, contextually in aging, has been overlooked. Here, we show that skin fibroblasts undergo age-mediated, sex-dependent changes in their proliferation, senescence, ROS levels, and stress response. We find that aged male fibroblasts selectively drive an invasive, therapy-resistant phenotype in melanoma cells and promote metastasis in aged male mice by increasing AXL expression. Intrinsic aging in male fibroblasts mediated by EZH2 decline increases BMP2 secretion, which in turn drives the slower-cycling, highly invasive, and therapy-resistant melanoma cell phenotype, characteristic of the aged male TME. Inhibition of BMP2 activity blocks the emergence of invasive phenotypes and sensitizes melanoma cells to BRAF/MEK inhibition.

INTRODUCTION

Age is an independent, poor prognostic factor in melanoma.[1,2] Older patients (>55 years) account for 40% of melanoma diagnoses,[3] often diagnosed at advanced stages, with decreased melanoma-specific survival[4] compared with younger patients. Although melanoma incidence is rising, mortality rates have declined due to early detection and breakthroughs in targeted and immune checkpoint inhibitor therapies.[5] However, these treatments are not typically curative for patients with advanced-stage disease in part due to acquired resistance to targeted therapies, which can occur within months of treatment, and variable responses to immunotherapy.[6–11] This is especially true in aged cohorts.[12,13] Elderly patients, further, are underrepresented in randomized clinical trials due to enhanced toxicity and poor efficacy.[14,15]

Sex has also emerged as an independent prognostic variable in cutaneous melanoma.[16] Men have a higher melanoma incidence and mortality rate than women, even when corrected for patient behavioral attributes.[17–20] In cutaneous melanoma, the underlying biological mechanisms responsible for sex disparity are unknown and complicated by clinical variables such as anatomical site, skin phototype,[16] body mass index,[21] and variability in immune responses.[22] Recent studies in young mice (aged 7–14 weeks) have shown that activation of non-canonical estrogen receptor (*GPER/GPR30*) or pharmacological inhibition of androgen receptor improves responses to immune checkpoint inhibitors[23] and *BRAF/MEK*-targeted therapies,[24] respectively. However, it remains unknown if these endocrinal modulations extrapolate to aged mice.

Several clinical studies have confirmed that nodal and distant melanoma metastasis is less frequent in females than males,[20,25] and males have decreased relapse-free survival.[26,27] Sex- and age-dependent epigenetic regulation can dictate metabolic, immune, senescence, oxidative stress, and DNA damage response (DDR) programs[28] of the surrounding tumor stroma, which could

potentially impact the metastatic cascade. In fact, several studies have highlighted sex dimorphism in biological aging that favors females across humans, primates, and rodents.[29–31] Therefore, understanding the fundamental differences in molecular circuitry between a male vs. female tumor microenvironment (TME) is warranted to determine the underlying molecular basis of melanoma progression and therapy resistance. More importantly, exposing age- and sex-specific regulators at the TME level will potentially identify novel targetable avenues and enable prediction of therapeutic responses to personalize treatment strategies.

We previously demonstrated that aging microenvironments promote melanoma invasion and metastasis as a result of altered fibroblast secretomes, and these changes contribute to inferior age-dependent clinical outcomes.[12,13,32,33] However, we did not assess the effects of sex. Men experience faster and/or earlier aging-associated detrimental programs likely ascribed to hormonal changes and other factors.[22,34,35] Here, we report that dermal fibroblasts have sex-specific changes with age that differentially impact melanoma cells in both a sex- and age-related manner. We also show a novel effect of bone morphogenetic protein 2 (BMP2) as a sex-dependent and age-associated secreted factor from the aged male dermal microenvironment that promotes metastatic dissemination and resistance to BRAF/MEK targeted therapy.

RESULTS

Age-associated replicative senescence in primary dermal fibroblasts is sex dependent

To study differences in the dermal microenvironment with age and sex, we used human primary dermal fibroblasts isolated from non-sun-exposed skin of healthy donors as part of the Baltimore Longitudinal Study of Aging[36] and stratified them as young (<35 years) or aged (>55 years) and male or female based on fibroblast karyotyping. Since fibroblast lineages can have distinct morphology, expression profiles, and functions,[37] we assessed mRNA expression levels of established papillary (PDPN) and reticular (TGM2, COL11A1, CNN1, CD36, CDH2) markers[37] and found no significant differences across the groups (Figure S1A). In addition, no consistent sex- or age-dependent upregulation of cancer-associated fibroblast markers[38,39] was evident among the four cohorts of young male, aged male, young female, and aged female donor-derived fibroblasts (Figure S1B).

To avoid effects from sex steroids or estrogenic activity from bovine serum and phenol red,[40] we performed cellular assays in phenol red-free and charcoal-stripped serum. BrdU incorporation demonstrated lower proliferation in young female fibroblasts compared with young males, similar to aged fibroblasts (Figures 1A and 1B), while senescence-associated β-galactosidase (SA-βgal) staining confirmed higher senescence in young female fibroblasts (Figures 1C and 1D). Only male fibroblasts showed significant age-related decrease in proliferation and increase in SA-βgal positivity as observed earlier.[13] Young female fibroblasts had increased senescence markers (p16, p21) and decreased proliferation indicators (-retinoblastoma (RB) phosphorylation; cyclin-dependent kinase-4 [CDK4]) compared with young males (Figures 1E and 1F). Increase in age-mediated p21, an early senescence marker,[41] was higher in male fibroblasts, while p16 was elevated in aged fibroblasts regardless of sex. Aged fibroblasts showed high endogenous activation of p38 mitogen-activated protein kinase (MAPK) and ERK1/2 pathways without sex-specific differences (Figure 1E). Both p38 and pERK1/2 MAPK activation pathways have been shown to act as damage-sensing pathways and promote the maintenance of a senescence phenotype.[42–45]

To confirm sex-based differences in fibroblast replicative capacity, at least two fibroblast lines from all four cohorts were subjected to 10 serial passages (termed early vs. late) and assessed for growth and senescence differences. Serial passaging of fibroblasts confirmed an overall decline in proliferation (Figures S1C and S1D) and increase in senescence (Figures S1E and S1F). Male fibroblasts showed greater reduction in proliferation (Figure S1G), and young males showed the highest increase in senescence (Figure S1H). Late-passage male fibroblasts had higher p21 increase and pRB decrease (Figure S1I). All late-passage cell lines showed a consistent increase in p38 and ERK1/2 activation but failed to upregulate p16 expression (Figure S1I), suggesting early senescent phase after ten serial passages.

Fibroblasts from the same donor taken 10–12 years apart showed slower proliferation (Figures 1G and 1H) and increased senescence (Figures 1I and 1J) in females <55 years. Males had faster age-mediated proliferation decline (Figure S1J). Immunoblotting revealed age-mediated p16 increase in males and p21 decrease in females (Figure 1K). ERK1/2 activation increased in males but decreased in females with age (Figure 1K), suggesting the existence of sex-specific signaling pathways in regulating DDR. Aged male fibroblast-conditioned media (CM) showed significantly higher levels of chemokine ligand-12 (CXCL12), interleukin (IL)-6, IL-18, thrombospondin-1 (TSP1), angiogenin (ANG), and CXCL1 than aged female fibroblasts (Figures 1L and 1M), associated with the senescence-associated secretory phenotype (SASP),[46,47] suggesting faster intrinsic aging-related dysfunction in the aged male dermal microenvironment.

Elevated oxidative stress in aged male dermal fibroblasts promotes the acquisition of an SASP

The SASP is associated with a persistent DDR[48] and is not a consequence of p16 activation,[49] suggesting that it is separate from growth arrest. Age-associated decline in telomere length was sex-independent (Figure S2A), suggesting that reduced replicative capacity in young female fibroblasts was not due to telomere shortening. Reactive oxygen species (ROS) levels were significantly elevated in aged male fibroblasts compared with other cohorts (Figures 2A and 2B). Mitochondrial ROS increased with age, showing robust sex differences in age-matched fibroblasts (Figures 2C and 2D). Aged male fibroblasts exhibited a higher percentage of nuclei with >2 p53 binding protein-1 (53BP1) foci, indicating DDR engagement (Figures 2E and 2F). Further, immunoblot analysis of aged fibroblasts revealed elevated expression of superoxide dismutase1 (SOD1), mitochondria-specific SOD (SOD2), and caveolin1 (CAV1) (Figure S2B)[50] in the aged male cohort. Elevated c-Jun-N-terminal kinase (JNK) activation in the absence of external stress stimuli

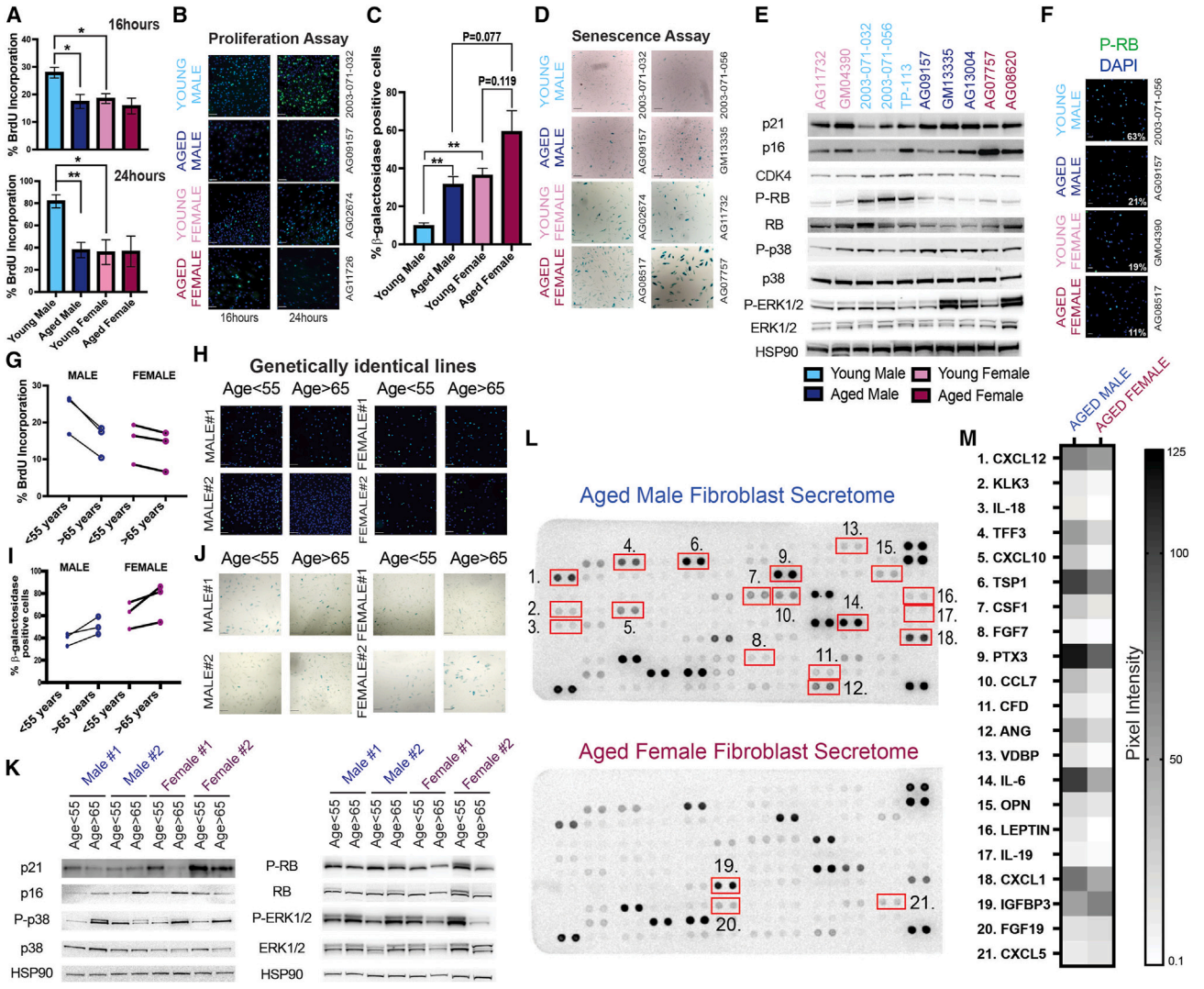

Figure 1. Age-associated replicative senescence in primary dermal fibroblasts is sex-dependent

(A) Quantification of BrdU incorporation as percentage BrdU-positive nuclei (green) in age- and sex-stratified fibroblasts over indicated time points. BrdU was added in media supplemented with charcoal-depleted serum and devoid of phenol red (**$p < 0.01$, *$p < 0.05$, $n = 3$).

(B) Representative immunofluorescent images of BrdU incorporation for 16 and 24 h from (A). Scale bars show 100 μm.

(C) Quantification of SA-βgal positive cells in age- and sex-stratified fibroblasts (**$p < 0.01$, $n = 3$).

(D) Representative images of SA-βgal assay from (C). Scale bars show 100 μm.

(E) Immunoblot for SASP proteins in age- and sex-stratified fibroblasts. Heat shock protein-90 (HSP90) was used as loading control.

(F) Representative immunofluorescence image of active RB (pRB-green) and nuclei (DAPI) in age- and sex-stratified fibroblasts, indicating the percentage of p-RB positive nuclei ($n = 2$). Scale bar shows 50 μm.

(G) Quantification of BrdU incorporation in genetically identical fibroblasts from the same donor (<55 and >65 years) stratified by sex, represented as paired analysis (before and after) ($n = 2$).

(H) Representative images of BrdU incorporation from (G). Scale bars show 100 μm.

(I) Quantification of SA-βgal positive cells in genetically identical fibroblasts from the same donor (<55 and >65 years) stratified by sex, represented as paired analysis (before and after) ($n = 2$).

(J) Representative images of SA-βgal assay from (I). Scale bars show 100 μm.

(K) Immunoblot of senescence phenotype-associated proteins in genetically identical fibroblasts from the same donor (<55 and >65 years) stratified by sex. HSP90 was used as loading control.

(L) Representative chemokine array blot on the conditioned media derived from aged male and female fibroblasts normalized by cell number. Significantly altered chemokines between the two groups are marked (red box) and numbered ($n = 2$).

(M) Heatmap of significantly altered chemokines numbered in (L) measured from densitometry analysis (arbitrary units).

Values are presented as mean ± SEM.

See also Figure S1.

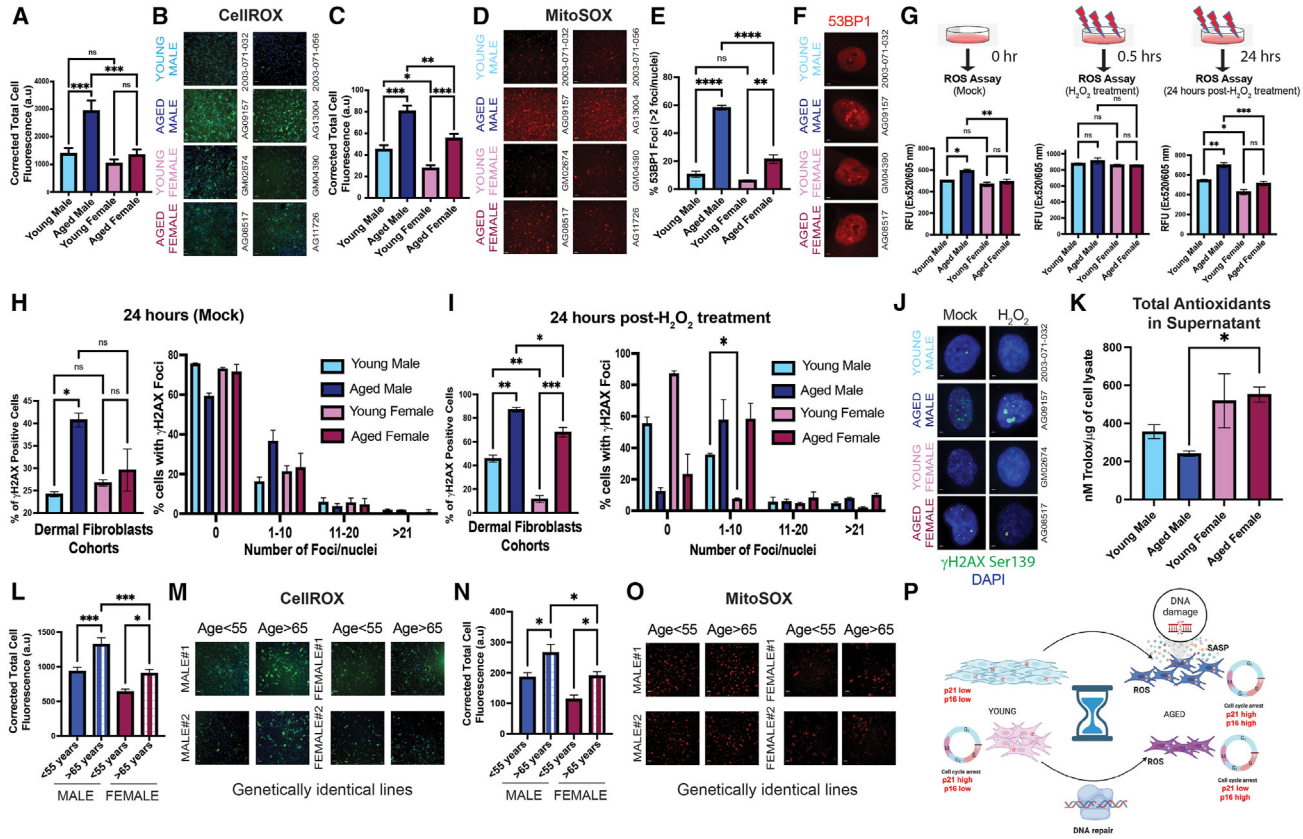

Figure 2. Elevated oxidative stress in aged male dermal fibroblasts promotes acquisition of an SASP

(A) Quantification of CellROX-green in age- and sex-stratified fibroblasts measured as corrected total cell fluorescence (arbitrary units) (***$p < 0.001$, $n = 3$).

(B) Representative images of CellROX-green-stained age- and sex-stratified fibroblasts from (A). Scale bars show 100 μm.

(C) Quantification of MitoSOX-red in age- and sex-stratified fibroblasts measured as corrected total cell fluorescence (arbitrary units) (***$p < 0.001$, **$p < 0.01$, *$p < 0.05$, $n = 3$).

(D) Representative images of MitoSOX-red-stained age- and sex-stratified fibroblasts from (C). Scale bars show 100 μm.

(E) Quantification of 53BP1 foci in age- and sex-stratified fibroblasts measured as percentage of nuclei with >2 foci (****$p < 0.0001$, **$p < 0.01$, $n = 3$).

(F) Representative immunofluorescent images of 53BP1 foci (red) in age- and sex-stratified fibroblasts from (E). Scale bars show 5 μm.

(G) Quantification of ROS levels in age- and sex-stratified fibroblasts; PBS treated (mock), 30 min after acute (2 mM) hydrogen peroxide treatment, and 24 h after hydrogen peroxide (2 mM for 30 min) treatment (***$p < 0.001$, **$p < 0.01$, *$p < 0.05$, $n = 3$).

(H) Quantification of γH2Ax foci in fibroblasts treated with PBS (mock) and measured as percentage γH2Ax positive nuclei with foci >2 per nuclei and as percentage of cells with indicated number of foci per nuclei (*$p < 0.05$, $n = 2$).

(I) Quantification of γH2Ax foci in fibroblasts 24 h after 30 min of hydrogen peroxide (2 mM) treatment and measured as percentage γH2Ax positive nuclei with foci >2 per nuclei and as percentage of cells with indicated number of foci per nuclei (***$p < 0.001$, **$p < 0.01$, *$p < 0.05$, $n = 2$).

(J) Representative immunofluorescent images of γH2Ax (Ser139) in age- and sex-stratified fibroblasts treated with PBS (mock) or 24 h post-hydrogen peroxide treatment from (H) and (I). Scale bars show 5 μm.

(K) Total antioxidants in conditioned media derived from age- and sex-stratified fibroblasts measured by ELISA (*$p < 0.05$, $n = 3$).

(L) Quantification of CellROX-green in genetically identical fibroblasts from the same donor (<55 and >65 years) stratified by sex and represented as corrected total cell fluorescence (arbitrary units) (***$p < 0.001$, *$p < 0.05$, $n = 3$).

(M) Representative images of CellROX-green from (L). Scale bars show 100 μm.

(N) Quantification of MitoSOX-red in genetically identical fibroblasts from the same donor (<55 and >65 years) stratified by sex and represented as corrected total cell fluorescence (arbitrary units) (*$p < 0.05$, $n = 3$).

(O) Representative images of MitoSOX-red from (N). Scale bars show 100 μm.

(P) Schematic representation of intrinsic differences in age- and sex-stratified fibroblasts. Created with Biorender.com.

Values are presented as mean ± SEM.

See also Figure S2.

was observed in young male fibroblasts (Figure S2B). Aged male fibroblasts showed persistent oxidative stress in ROS assays before (0 h) and after (0.5 and 24 h) acute hydrogen peroxide treatment (Figure 2G). Following an acute hydrogen peroxide treatment of 0.5 h, ROS levels were consistently elevated in all fibroblast lines (Figure 2G, middle graph). While other fibroblast lines returned to baseline ROS levels 24 h post-treatment, aged male fibroblasts could not alleviate ROS or repair damage.

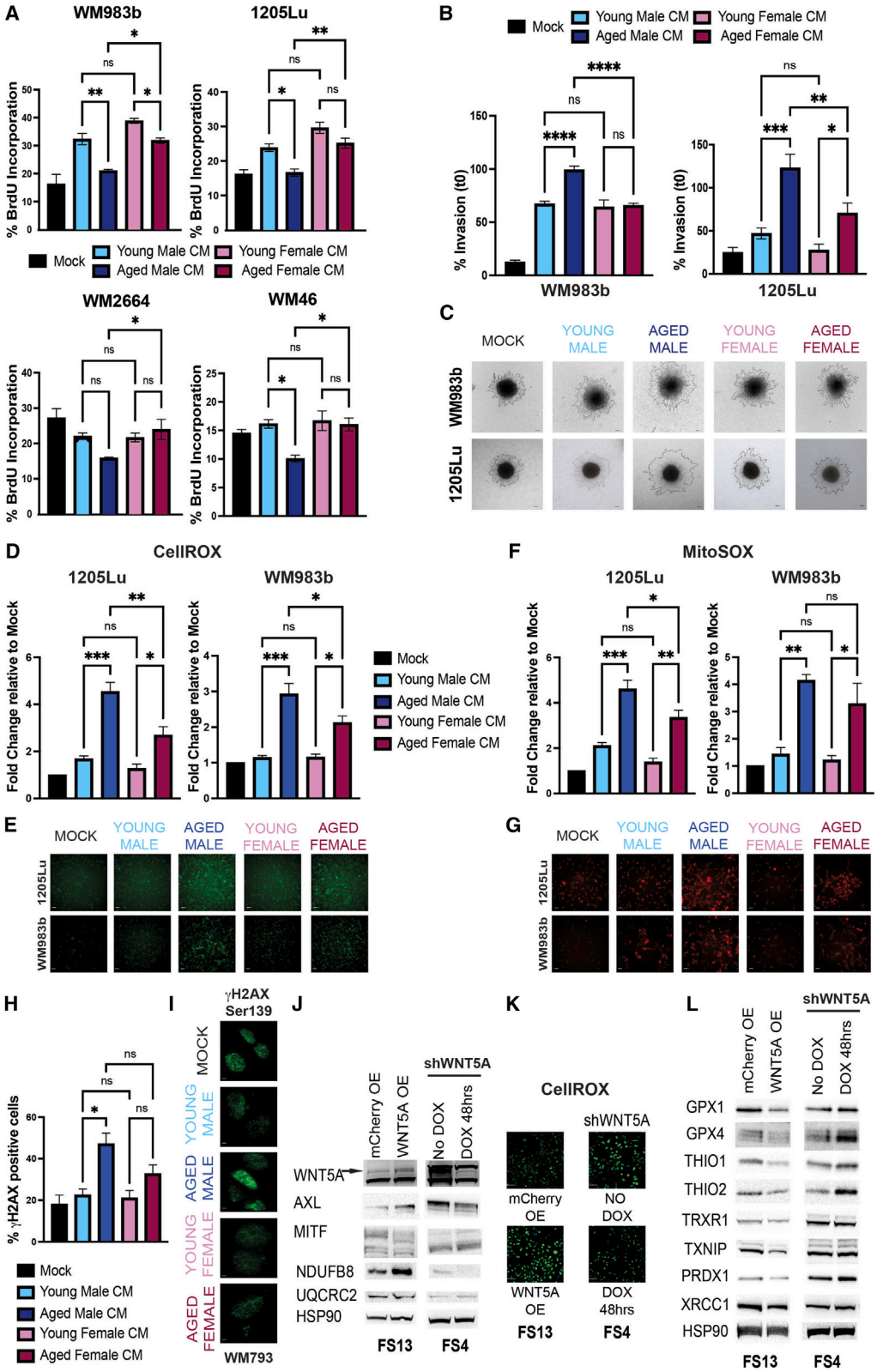

(legend on next page)

Aged male fibroblasts also exhibited a higher percentage of unresolved γH2Ax foci 24 h after treatment (Figures 2H–2J), indicating impaired DNA repair capacity. Young female fibroblasts demonstrated faster DNA damage clearance, supported by high levels of redox proteins (Figures S2C and S2D) and elevated total antioxidants in their secreted media (Figure 2K).

Finally, we assessed the ROS levels in genetically identical fibroblast lines, i.e., cell lines derived from the same donor, 10–12 years apart. Cellular ROS significantly increased with age in males, with only a modest increase in females (Figures 2L and 2M), while mitochondrial ROS modestly increased with age across both sexes (Figures 2N and 2O). In addition, CellROX analysis in serially passaged cell lines showed an overall increase in cellular ROS levels at late passage, with greater increase in male fibroblasts than in age-matched female fibroblasts (Figure S2E). Mitochondrial ROS levels did not increase significantly in female fibroblast lines following serial passaging but showed an increasing trend in male fibroblasts (Figure S2F). Overall, our data suggest that female fibroblasts promote repair during aging due to reduced replicative capacity from higher endogenous p21 expression, while male fibroblasts accrue ROS and exhibit persistent DDR, which potentiates the early SASP identified in aged male fibroblasts (Figure 2P).

Aged male fibroblasts promote maximal invasion and oxidative stress in melanoma cells relative to female fibroblasts

Our previous study assessed the effect of the aged dermal microenvironment on melanoma cell behavior[13] but did not consider sex as a variable. We examined the impact of age- and sex-dependent fibroblast differences on male- and female-derived melanoma cell growth and invasion using CM from all four fibroblast cohorts. Most melanoma lines showed reduced proliferation in aged male fibroblast-derived CM compared with young male and aged female CM (Figure 3A). Invasion analysis of melanoma spheroids (highly invasive 1205Lu and poorly invasive WM983b, WM2664) revealed that cells exposed to aged male-derived CM consistently showed the highest increase in invasion (Figures 3B, 3C, and S3A). Previous work from our laboratory has shown that aged dermal fibroblasts promote a "phenotype switch" in melanoma cells, resulting in a slower-cycling, highly invasive population,[32,51,52] characterized by differential wingless-related integration site (WNT) signaling. Non-canonical WNT signaling through AXL receptor tyrosine kinase drives a slow-cycling, highly invasive phenotype in melanoma cells. We found that this phenotype switch, characterized by increased AXL expression, was most prominent in melanoma cells treated with CM from aged male fibroblasts (Figure S3B). Our results show that secreted factors from aged male fibroblasts drive the highest magnitude of invasiveness in melanoma cells, which was corroborated using CM from genetically identical fibroblast lines (Figure S3C).

We next assessed whether fibroblasts could alter oxidative stress in melanoma cells. While the ROS levels in melanoma cells, as measured by CellROX and MitoSOX, increased with age, they were most pronounced after incubation in CM (48 h) from aged male fibroblasts, which was exacerbated by reduction in apurinic/apyrimidinic endonuclease 1 (APE1), a redox effector and base excision repair enzyme (Figures 3D–3G and S3D). Immunofluorescence analysis of γH2Ax (Ser139) foci measurements also revealed elevated damage in melanoma cells when subjected to aged male CM (Figures 3H and 3I). These data suggest that stromal cells in the aged male TME induce more oxidative stress in melanoma tumors relative to the female TME.

Figure 3. Aged male fibroblasts promote maximal invasion and oxidative stress in melanoma cells

(A) Quantification of BrdU incorporation represented as percentage BrdU-positive nuclei (green) in male (WM983b, 1205Lu) and female (WM2664, WM46) melanoma cells subjected to conditioned media from age- and sex-stratified fibroblasts for 48 h. Normal growth media was used as mock control. BrdU was added to the media in the last hour (**$p < 0.01$, *$p < 0.05$, $n = 3$).

(B) Quantification of melanoma spheroids subjected to conditioned media from age- and sex-stratified fibroblasts for 24 (1205Lu) or 72 h (WM983b). Normal growth media was used as mock control. Invasion represented as percent invasion relative to 0 h (****$p < 0.0001$, ***$p < 0.001$, **$p < 0.01$, *$p < 0.05$, $n = 3$).

(C) Representative bright-field images of melanoma spheroid invasion from (B) with invasive area outlined in black. Images taken at 24 (1205Lu) and 72 h (WM983b) post collagen-embedding. Scale bars show 100 μm.

(D) Quantification of CellROX-green in melanoma cell lines 1205Lu and WM983b treated with conditioned media from age- and sex-stratified fibroblasts for 48 h and measured as corrected total cell fluorescence (arbitrary units). Normal growth media was used as mock, and data are represented as fold change relative to mock (***$p < 0.001$, **$p < 0.01$, *$p < 0.05$, $n = 3$).

(E) Representative images of CellROX-green in melanoma cells subjected to conditioned media age- and sex-stratified fibroblasts from (D). Scale bars show 100 μm.

(F) Quantification of MitoSOX-red in melanoma cell lines 1205Lu and WM983b treated with conditioned media from age- and sex-stratified fibroblasts for 48 h and measured as corrected total cell fluorescence (arbitrary units). Normal growth media was used as mock, and data are represented as fold change relative to mock (***$p < 0.001$, **$p < 0.01$, *$p < 0.05$, $n = 3$).

(G) Representative images of MitoSOX-red in melanoma cells subjected to conditioned media from age- and sex-stratified fibroblasts from (F). Scale bars show 100 μm.

(H) Quantification of γH2Ax (Ser139) measured as percentage γH2Ax positive nuclei in WM793 melanoma cells subjected to conditioned media from age- and sex-stratified fibroblasts for 48 h. Normal growth media was used as mock (*$p < 0.05$, $n = 3$).

(I) Representative images of γH2Ax (Ser139) in WM793 subjected to conditioned media from age- and sex-stratified fibroblasts from (H). Scale bars show 10 μm.

(J) Immunoblot confirming WNT5A overexpression (OE) in FS13 melanoma line with mCherry OE as control and 48 h doxycycline (DOX) treatment (1 μg/mL) of FS4 melanoma line transduced with DOX-inducible WNT5A short hairpin RNA (shRNA) vector. WNT5A levels (active WNT5a form indicated by black arrow) correlate positively with OXPHOS complex I (NDUFB8) with no change in complex III (UQCRC2). HSP90 was used as loading control.

(K) Representative images of CellROX-green following modulation of WNT5A expression from (J). Scale bars show 100 μm.

(L) Immunoblot analysis of indicated redox proteins following WNT5A modulation from (J). HSP90 was used as loading control.

Values are presented as mean ± SEM.

See also Figure S3.

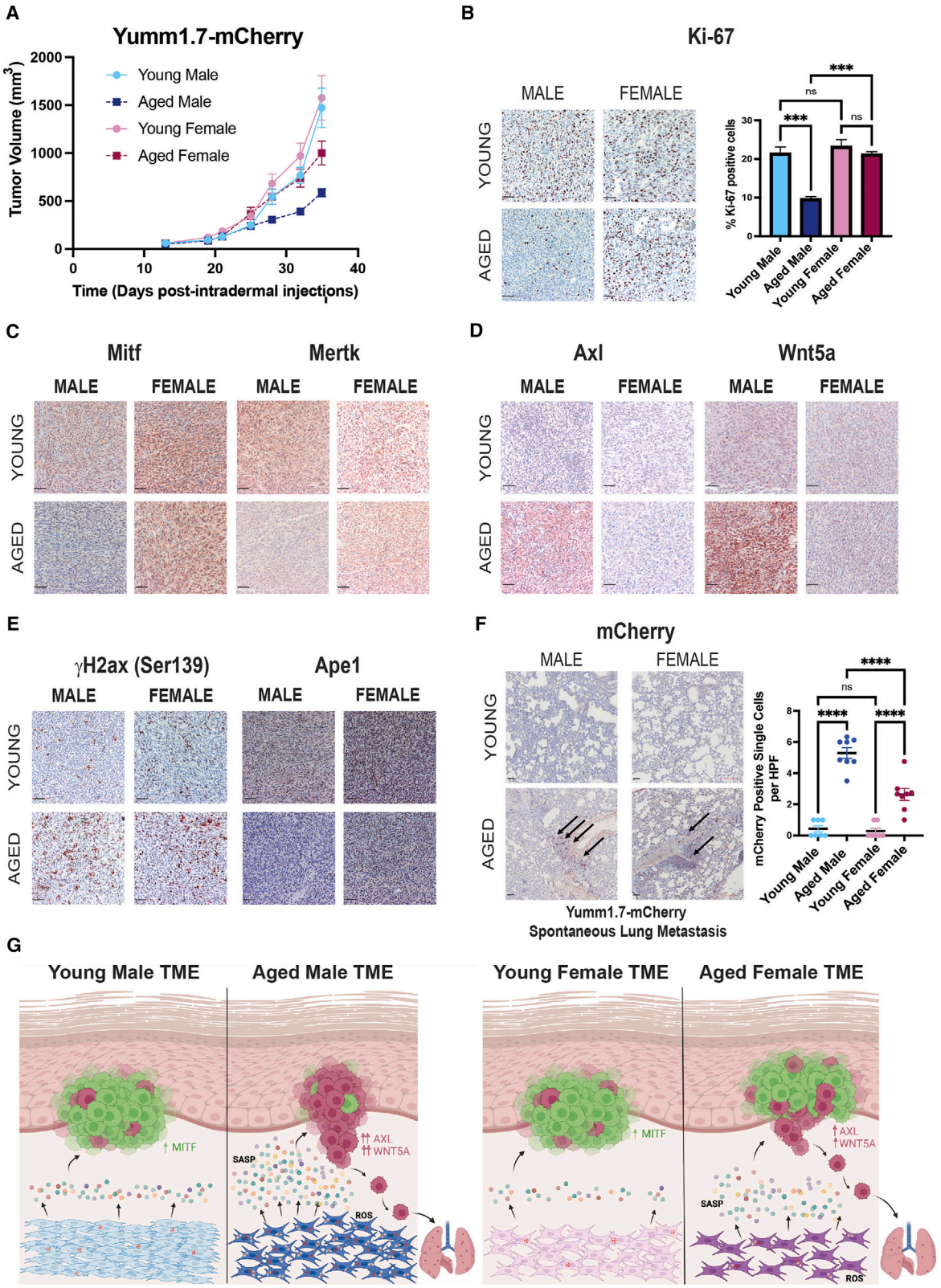

(legend on next page)

We observed higher endogenous ROS and DNA damage in 1205Lu and WM793 (WNT5A^{high} lines), and since WNT5A can regulate AXL,[32] we investigated whether there was a correlation between WNT5A and ROS levels using genetic manipulation of endogenous WNT5A expression. Overexpression of WNT5A in FS13 (WNT5A^{low} line) and doxycycline (DOX)-induced repression of WNT5A in FS4 (WNT5A^{high} melanoma line) mediated an increase in the expression of complex I subunit (NADH:ubiquinone oxidoreductase subunit B8 [NDUFB8]) with no change in complex III subunit (UQCRC2) in melanoma cells (Figure 3J). This relative abundance of complex I vs. complex III has been associated with increased ROS production.[53] Modulation of endogenous WNT5A expression positively regulated ROS levels (Figure 3K). Further, increases in WNT5A expression promoted a reduction in redox genes involved in detection and DDR programs, which was rescued by decreasing WNT5A expression (Figure 3L). Analysis of the redox pathway genes in The Cancer Genome Atlas Program (TCGA) cohort further confirms that a high WNT5A and AXL signature correlates with a reduced redox gene signature (Figure S3E). This suggests that aged male fibroblast-mediated phenotype switching toward WNT5A^{high}/AXL^{high} expression promotes increased oxidative stress.

Age and sex of the host microenvironment regulate melanoma growth and metastasis *in vivo*

To assess host effects *in vivo*, we injected male and female immunocompetent young (8 weeks) and aged (>52 weeks) C57BL/6 mice intradermally with a male murine melanoma cell line, Yumm1.7 (BRAF^{V600E}PTEN$^{-/-}$/CDKN2A$^{-/-}$),[54] and a female murine melanoma cell line, BSC9AJ2 (BRAF^{V600E}/Trp53^{R172H}),[55] both expressing mCherry fluorescent protein. Tumor growth analysis in Yumm1.7-mCherry revealed that within each sex, tumors grew slower in aged mice than young mice (Figures 4A, S4A, and S4B). In aged males, tumor growth was significantly less than in aged female mice, but we found no significant difference in tumor growth between young males and young or aged female mice (Figures 4A and S4B). A similar trend was observed in faster-growing BSC9AJ2 tumors, with reduced tumor growth in aged male mice compared with young males and young and aged females (Figures S4C–S4E). Interestingly, there were no significant differences in tumor growth between young and aged females (Figure S4D). Measurement of Ki-67 positive nuclei confirmed a reduced proliferative capacity in aged male primary tumors across Yumm1.7 (Figure 4B) and BSC9AJ2 (Figure S4F) models. We next assessed key markers regulating proliferative (MITF, MERTK) vs. invasive melanoma states (WNT5A, AXL).[32,51,56] Immunohistochemistry (IHC) showed reduced Mitf and Mertk expression and elevated Wnt5a and Axl expression in aged male tumors (Figures 4C, 4D, S4G, and S4H; Data S1). These tumors also showed elevated γH2ax (Ser139) and reduced Ape1 expression (Figures 4E and S4I; Data S1). Further analysis of Yumm1.7 tumors in aged male mice confirmed a slow-cycling phenotype with increased p53, Sod1, 53bp1, and Nrf2 activation and reduced Xrcc1 expression (Figures S5A–S5E; Data S1). Elevated protein nitrosylation levels were also detected in aged male primary tumors, confirming that these tumors undergo higher ROS-mediated damage (Figure S5F; Data S1).

We have shown high WNT5A and AXL expression promotes increased melanoma dissemination to the lung.[32,52] In the Yumm1.7 model, aged mice showed spontaneous pulmonary micrometastases (<10 cells/lesion), while young mice did not (Figure 4F). Interestingly, aged female lungs exhibited immune cell infiltration (CD45^{+} cells) near metastasizing melanoma cells (Figure S5G). The BSC9AJ2 model showed similar age-related increases in lung micrometastases, with significantly more in aged male lungs than aged female lungs (Figure S5H). The CD45^{+} immune cell populations were not observed in the BSC9AJ2 model, suggesting that this was an immunogenic response to a "male" melanoma line in the aged female lung. This was confirmed by time course analysis of Yumm1.7 cells in aged mice, which revealed higher initial immune infiltration in female lungs that decreased over time, while male lungs showed lower, constant immune infiltration and earlier melanoma seeding (Figures S5I and S5J). Our data suggest that the age- and sex-dependent TME promotes a slow-cycling, invasive state in aged male hosts, facilitating efficient metastatic pulmonary dissemination (Figure 4G).

Age and sex of the host microenvironment regulate therapy response and resistance

The role of sex in targeted therapy resistance in the TME has only recently been assessed,[24] but not in the context of aging. Previous studies from our lab showed aged dermal fibroblasts promote therapy resistance,[12,13] but sex was not considered as a

Figure 4. Age and sex of the host microenvironment regulate melanoma growth and metastasis *in vivo*

(A) Tumor growth measurement of male murine Yumm1.7-mCherry injected intradermally in immunocompetent C57BL/6 mice young (8 weeks) and aged (>52 weeks) across both sexes (n = 7 mice per group).

(B) Histological examination of Ki-67 (brown) in Yumm1.7-mCherry primary tumors and quantified as percentage Ki-67 positive nuclei (***$p < 0.001$, n = 5 tumors per group). Scale bars show 50 μm.

(C) Representative images of Yumm1.7-mCherry primary tumors stained for Mitf and Mertk expression (n = 4 tumors per group). Scale bars show 50 μm.

(D) Representative images of Yumm1.7-mCherry primary tumors stained for Axl and Wnt5a expression (n = 4 tumors per group). Scale bars show 50 μm.

(E) Representative images of Yumm1.7-mCherry primary tumors stained for γH2ax (Ser139) and Ape1 expression (n = 4 tumors per group). Scale bars show 50 μm.

(F) Representative images of lung metastasis stained with mCherry at 5 weeks post-intradermal injection of Yumm1.7-mCherry cells in young (8 weeks) and aged (>52 weeks) C57BL/6 mice across both sexes. Black arrow indicates mCherry-positive cells. Scale bars show 50 μm.

(G) Diagram summarizing differential effects of host sex and age dermal microenvironment on melanoma cell growth and invasion *in vivo*. Created with Biorender.com.

Values are presented as mean ± SEM.

See also Figures S4 and S5 and Data S1.

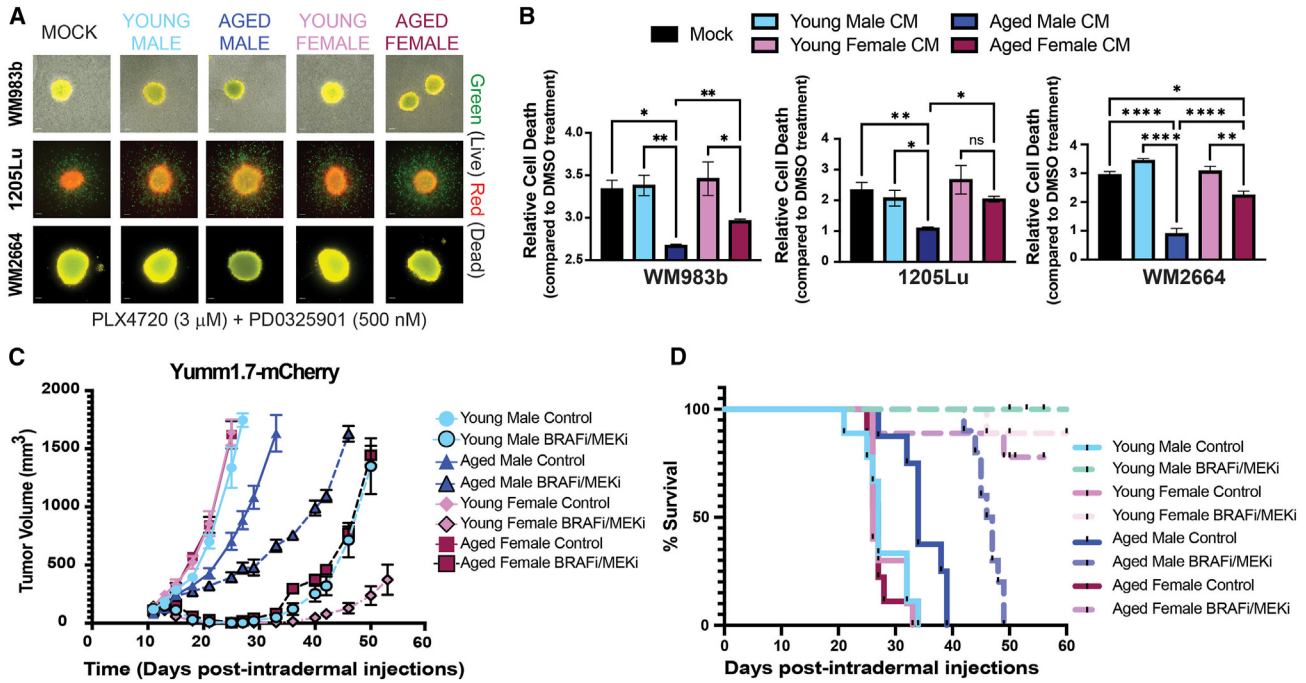

Figure 5. Age and sex of the host microenvironment regulate therapy response and resistance

(A) Viability assay on melanoma spheroids treated with age- and sex-stratified fibroblast-conditioned media in the presence of 3 μM PLX4720 (BRAFi) and 500 nM PD0325901 (MEKi) or DMSO (mock) for 48 h. Viability was assessed by staining with calcein-AM (green) and ethidium homodimer-1 (red/orange), indicating live and dead cells, respectively. Scale bars show 100 μm.

(B) Quantification of cell death (total intensity of ethidium homodimer-1) relative to spheroid area (calcein-AM) following BRAFi/MEKi treatment is represented as relative cell death compared with DMSO treatment (****$p < 0.0001$, **$p < 0.01$, *$p < 0.05$, $n = 3$).

(C) Tumor growth measurement of Yumm1.7-mCherry injected intradermally in immunocompetent C57BL/6 mice young (8 weeks) and aged (>52 weeks) across both sexes. Mice were randomized to receive diet containing control chow (control) or BRAFi/MEKi chow (200 mg/kg PLX4720 and 7 mg/kg PD0325901) *ad libitum* ($n = 7$ mice per control chow group and $n = 8$ mice per BRAFi/MEKi chow group).

(D) Kaplan-Meier survival curves for mice treated in (C), indicating the time taken for the tumor to reach a defined size of tumor volume 1,500 mm^3 or death with a day 50 cutoff, by which all aged male mice were euthanized.

Values are presented as mean ± SEM.

See also Figures S6 and S7 and Data S1.

variable. To assess age and sex effects on therapy response, we treated $BRAF^{V600E}$ mutant melanoma spheroids in fibroblast-derived CM with 3 μM PLX4720 (BRAF inhibitor [BRAFi]) plus 500 nM PD0325901 (MEK inhibitor [MEKi]). Melanoma cells in aged male fibroblast-derived CM showed reduced response to inhibition compared with other conditions (Figures 5A and 5B). CM from aged genetically identical male fibroblasts over 10–12 years imparted therapeutic resistance (Figures S6A and S6B), but CM from aged female fibroblasts did not.

In vivo, young (8 weeks) and aged (>52 weeks) C57BL/6 mice of both sexes were injected with Yumm1.7-mCherry melanoma cells and treated with BRAFi/MEKi (fed *ad libitum* with control chow or chow containing 200 mg/kg PLX4720 [BRAFi] and 7 mg/kg PD0325901 [MEKi]). Tumors in young and aged female mice on control chow reached endpoint earlier than aged males (Figures 5C, S6C, and S6D). With treatment, tumors in young male, young female, and aged female mice initially regressed, while aged male tumors were resistant. Tumors relapsed in aged female (19 days), young male (23 days), and later in young female (30 days) mice. BRAFi/MEKi therapy extended survival in females regardless of age, but only in young and not aged male mice (Figures 5D, S6E, and S6F), suggesting sex as an important determinant of targeted therapy response in melanoma.

We next evaluated the expression of therapy resistance drivers in primary tumors of mice fed control chow (naive) vs. BRAFi/MEKi chow (resistant). Tumor proliferation, measured by Ki-67, was similar to our earlier observations in therapy-naive mice (Figure 4B) and decreased in primary tumors across all BRAFi/MEKi-resistant cohorts (Figure S7A; Data S1). Therapy-resistant tumors across all cohorts increased expression of Wnt5a (Figure S7B; Data S1) and Axl (Figure S7C; Data S1) while reducing Mitf (Figure S7D; Data S1). While Wnt5a and Mitf levels increased and decreased, respectively, in the therapy-resistant tumors relative to naive tumors in aged males, Axl expression remained unchanged, suggesting that the dermal microenvironment in aged male mice is sufficient to elevate Axl independent of its upstream regulator Wnt5a. This is similar to the dermal fibroblast-mediated effect on melanoma cells, where elevated expression in AXL was detected independent of WNT5A increase (Figure S3B). Targeted therapy-resistant primary tumors

across all cohorts also showed increased expression of γH2ax (Ser139) foci, as well as reduced Ape1, with maximum oxidative stress in aged male tumors, further supporting the increase of an invasive WNT5A^{high}AXL^{high}MITF^{low} population (Figures S7E and S7F; Data S1).

BMP2 in the aged male dermal microenvironment promotes melanoma invasion and fibroblast senescence

We performed proteomics analysis (Table S1) on CM from primary human dermal fibroblasts. BMP2 was identified as exclusively elevated in the aged male fibroblast cohort, both at mRNA and secreted protein levels (Figures 6A–6C and S6A–S6C). However, immunoblotting detected no difference in BMP2 expression across the fibroblast cohorts (Figure S8A), suggesting that while endogenous protein expression does not change, it is secreted at a much higher rate. Other BMP family members (*BMP4*, *BMP6*, *BMP7*, *GDF6*) and receptors (*BMPR-1A*, *BMPR-1B*, *BMPR-2*), and the BMP modulator (*NOGGIN*) remained unaltered (Figure S8B). Neutralization of secreted BMP2 in aged dermal fibroblasts further confirmed BMP2 secretion was restricted to aged male fibroblasts (Figure S8C). BMP2 promotes a mesenchymal phenotype in melanoma cells[57] and drives neural crest migration of melanoma cells in chick embryos.[58–60] Melanoma cells responded to recombinant BMP2 (rBMP2) with increased suppressor of mothers against decapentaplegic-1/5 (SMAD1/5) activation in a dose- and time-dependent manner (Figures 6D, 6E, S8D, and S8E). Long-term rBMP2 treatment increased AXL, N-cadherin (CDH2), and MLC2 activation in melanoma lines, promoting a mesenchymal phenotype and suggesting that BMP2-driven cytoskeletal remodeling[61] may contribute to increased invasion (Figures 6F and S8F). rBMP2 reduced melanoma proliferation (Figures 6G and S8G) but increased invasion (Figures 6H, 6I, and S8H), mirroring the effects of aged male fibroblast-derived CM on melanoma cells (Figures 3A–3C and S3A). In fibroblasts, rBMP2 treatment increased p16 expression and reduced proliferation (Figures S9A and S9B) without affecting cellular or mitochondrial ROS (Figure S9C). This suggests that BMP2, secreted by aged male dermal fibroblasts, accelerates senescence in neighboring fibroblasts by driving p16 expression, leading to subsequent DNA damage accumulation and SASP development independent of BMP2.

We next assessed fibroblast lines across the four cohorts for changes in the key subunit of polycomb group genes (PcGs) and enhancer of zeste 2 polycomb repressive complex 2 subunit (EZH2). EZH2 plays a critical role in several cellular processes and mediates epigenetic gene silencing by catalyzing H3K27 trimethylation (H3K27me3), which promotes chromatin compaction and transcriptional repression.[62] Importantly, Ezh1/Ezh2-catalyzed H3K27me3 has recently been shown to regulate sex-dependent genetic programs; Ezh1/Ezh2 deficiency in murine liver directed a significant loss of sex-biased gene expression, particularly in males, and promoted liver fibrosis and cancer.[63] Further, loss of EZH2 in dermal fibroblasts induces senescence and drives SASP.[41] We found a significant decline in EZH2 and H3K27me3 expression with age, primarily in male fibroblasts (Figures 6J and 6K). EZH2 inhibition increased p16 levels and trended toward increased BMP2 expression (Figures 6L and 6M). Ataxia telangiectasia mutated (ATM) kinase is implicated in EZH2 decline.[41,64] ATM inhibition using KU-60019 increased EZH2 and decreased BMP2 in aged male fibroblasts (Figures S9D and S9E). Higher basal ATM phosphorylation was observed in aged male fibroblasts (Figure S9F). This suggests aged male dermal fibroblasts undergo faster intrinsic aging due to persistent DNA damage, promoting EZH2 and H3K27me3 decline via ATM activation, leading to elevated BMP2 secretion.

Modulation of BMP2 levels regulates tumor growth and therapy resistance

We found high circulating BMP2 levels in healthy males compared with age-matched (>55 years) females (Figure 7A), which tripled in male stage IV melanoma patients, which is associated with shorter survival (Figure 7B).[60] Age- and stage (I/II)-matched human melanoma tumors showed higher BMP2 expression in males (Figures 7C, S10A, and S10B). IHC of Yumm1.7 and BSC9AJ2 tumors revealed increased BMP2 in aged male mice (Figure 7D; Data S1). *In vitro*, Yumm1.7 showed rmBMP2-mediated Smad1/5 activation, reduced proliferation, and increased Cdh2 and Mlc2 activation (Figures S10C–S10E). Unlike in human lines, Wnt5a increased and Mitf decreased after 48 h of rmBMP2 treatment (Figure S10E). BMP2 can induce its own expression via positive feedback mechanisms.[65–67] Sustained rBMP2 treatment increased endogenous BMP2 expression in melanoma cell lines (Figure S10F).

To assess BMP2's effect on melanoma *in vivo*, young male C57BL/6 mice were injected with Yumm1.7-mCherry and treated with rmBMP2 (1 μg/mouse in PBS) or PBS. BMP2 treatment significantly reduced tumor growth (Figure 7E), similar to aged male mice (Figure 4A). IHC analysis showed rmBMP2 promoted a slow-cycling (reduced Ki-67 and Mitf), invasive (elevated Axl and Wnt5a) phenotype with increased DNA damage (elevated γH2ax Ser139) (Figure 7F; Data S1), resembling aged male primary tumors (Figures 4C–4E). Increased Erk1/2 and Smad1/5 activation was observed in rmBMP2-injected tumors (Figure 7F; Data S1). Similar Erk1/2 activation was seen in aged male cohorts, but without Smad1/5/8 activation (Figures S9G and S9H; Data S1), possibly due to overlap in transforming growth factor β (TGF-β) family receptor utilization and SMAD activation as seen across several cell types of the TME.[68,69] In addition, AXL, via its ligand GAS6[70] or activation of autocrine TGF-β,[71] can promote SMAD activation in the TME. Finally, assessment of murine lungs showed increased metastatic seeding and micrometastasis of melanoma cells in the lungs of mice injected with rmBMP2 (Figure 7G), confirming the role of BMP2 in mediating invasion and metastasis *in vivo*.

We evaluated rmBMP2's effect on melanoma spheroids subjected to BRAFi/MEKi treatment, finding that BMP2-primed spheroids were resistant (Figures 7H and S10G). To test this *in vivo*, we injected young (8 weeks) male C57BL/6 mice intradermally with Yumm1.7-mCherry and randomized them into two groups: rmBMP2 (1 μg/mouse) or PBS every alternate day. Once tumors were palpable, mice were further randomized to control chow or BRAFi/MEKi-containing chow *ad libitum*. Young male C57BL/6 mice injected with Yumm1.7-mCherry were treated with rmBMP2 or PBS, then randomized to control or

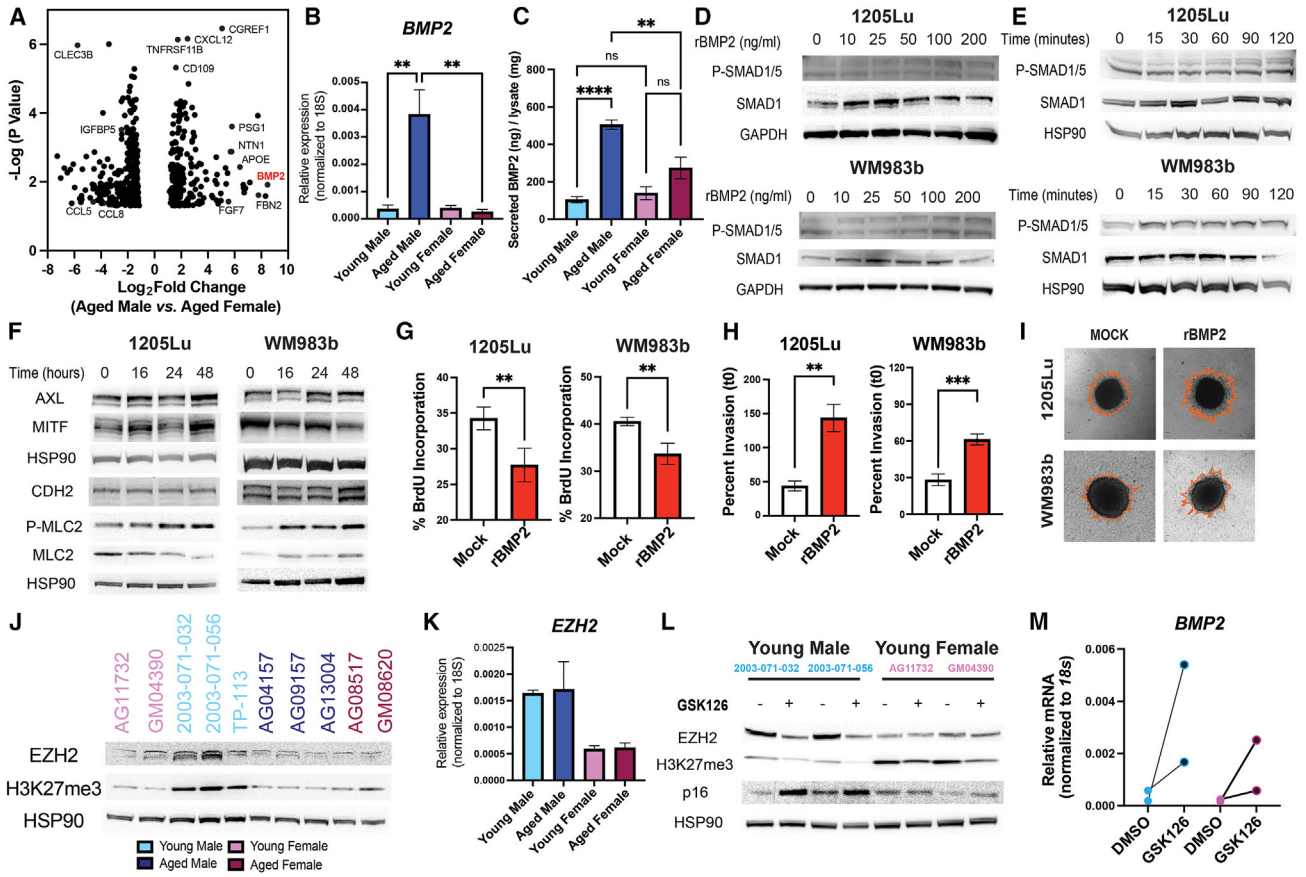

Figure 6. BMP2 in the aged male dermal microenvironment promotes melanoma invasion and fibroblast senescence

(A) Proteomics analysis on secreted proteins from healthy non-sun-exposed human dermal fibroblasts from two aged male and two aged female fibroblast lines, each in triplicate. A false discovery rate of less than 5% was considered significant. See also Table S1.

(B) Relative gene expression (RT-qPCR) of *BMP2* in age- and sex-stratified fibroblasts normalized to *18s* ($n = 3$).

(C) BMP2 ELISA on conditioned media (72 h) derived from age- and sex-stratified fibroblasts, quantified based on the fibroblast cell lysate protein amount (****$p < 0.0001$, **$p < 0.01$, $n = 3$).

(D and E) Immunoblot for recombinant BMP2 (rBMP2) treatment in melanoma lines (D) at indicated concentrations (for 30 min) and (E) at indicated time points (at 100 ng/mL). HSP90 or glyceraldehyde 3-phoshate dehydrogenase (GAPDH) was used as loading control.

(F) Immunoblot for proliferative (MITF), invasive (AXL, p-MLC2), and mesenchymal (CDH2) markers in melanoma cells treated with rBMP2 (100 ng/mL) at indicated time points. HSP90 was used as loading control.

(G) Quantification of BrdU incorporation in melanoma cells treated with rBMP2 (100 ng/mL) or PBS (mock) for 48 h. BrdU was added in the last hour (**$p < 0.01$, $n = 3$).

(H) Quantification of percent invasion of collagen-embedded melanoma spheroids subjected to rBMP2 treatment (100 ng/mL) or PBS (mock) for 24 (1205Lu) or 72 h (WM983b) (***$p < 0.001$, **$p < 0.01$, $n = 3$).

(I) Representative images from (H) for spheroid invasion following rBMP2 (100 ng/mL) or PBS (mock) treatment of melanoma cells. Invaded area is outlined in red. Images were taken at 24 (1205Lu) and 72 h (WM983b). Scale bars show 100 μm.

(J) Immunoblot of EZH2 and H3K27me3 in age- and sex-stratified dermal fibroblasts. HSP90 was used as loading control.

(K) Relative gene expression of *EZH2* in age- and sex-stratified dermal fibroblasts normalized to *18s* ($n = 3$).

(L) Immunoblot on two young male and female fibroblasts treated with EZH2 inhibitor, GSK126 (5 μM), or DMSO control for 4 days. HSP90 was used as loading control.

(M) Relative gene expression (RT-qPCR) of *BMP2* in two young male and female fibroblasts treated with EZH2 inhibitor, GSK126 (5 μM), or DMSO control for 4 days ($n = 2$).

Values are presented as mean ± SEM.

See also Figures S8 and S9.

BRAFi/MEKi chow. rmBMP2-treated tumors grew slower but showed earlier resistance to BRAFi/MEKi (Figure 7I). BRAFi/MEKi-resistant tumors had increased Bmp2 expression, highest in aged males (Figure 7J; Data S1). BRAFi-resistant melanoma lines showed increased BMP2, AXL, WNT5A, and reactivated ERK1/2 expression (Figures 7K and S10H), suggesting autocrine BMP2 secretion in resistant tumors, with continued dermal microenvironment secretion in aged males. Elevated BMP2 has also been reported in the BRAFi therapy-induced secretome of melanoma cells,[72] suggesting melanoma tumors, in

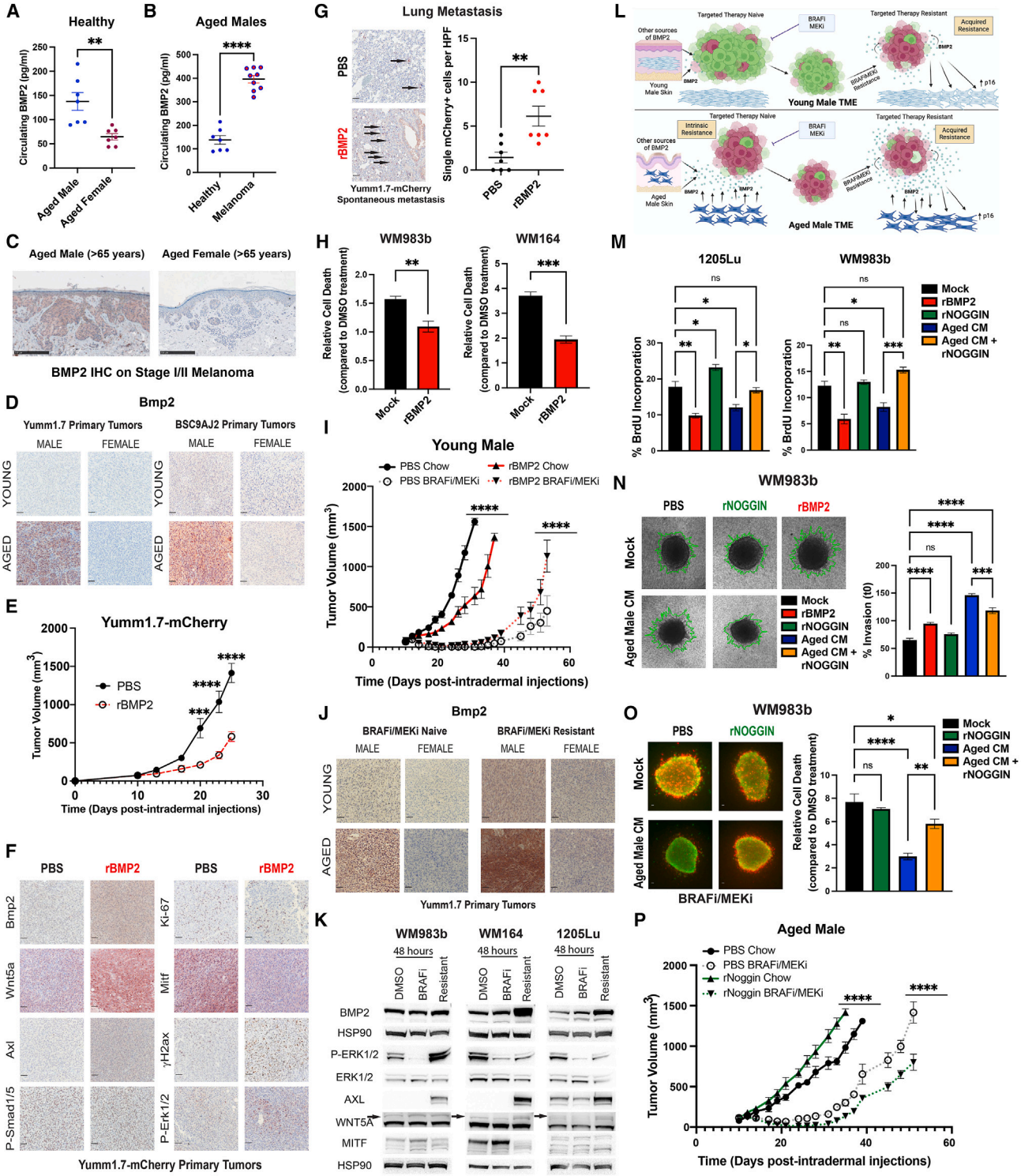

Figure 7. Modulation of BMP2 levels regulates tumor growth and therapy resistance

(A) ELISA on serum from age-matched (>55 years) healthy male ($n = 7$) and female subjects ($n = 7$) (**$p < 0.01$).

(B) ELISA on serum from age-matched (>55 years) healthy male ($n = 7$) and male patients with stage IV melanoma ($n = 9$) (****$p < 0.001$). ELISA ran concurrently with sample from (A).

(C) Histological analysis of BMP2 in age-matched stage I/2 human melanoma patients (>55 years) stratified by sex. Scale bars show 250 μm. See Figure S7A for corresponding H&E and Table S2.

(legend continued on next page)

conjunction with the aged dermal microenvironment, secrete BMP2 as a mechanism to evade suppression.

We transduced Yumm1.7 and BSC9AJ2 cells to express murine Bmp2 (mBmp2-mCherry) or empty vector control (mEV-mCherry). mBmp2-overexpressing cells showed elevated Erk1/2 and Smad1/5 activation, upregulation of Wnt5a or Axl, and slower proliferation (Figures S10I and S10J). *In vivo*, mBmp2-mCherry tumors became resistant early to BRAFi/MEKi therapy compared with mEV-mCherry tumors (Figures S11A and S11B). IHC analysis confirmed maximal Bmp2 expression in aged male tumors (Figures S11C and S11D). In the aged male cohort, Bmp2 overexpression showed no significant effect compared with control, supporting BMP2's role in providing intrinsic and acquired resistance to BRAF/MEK inhibition in aged male TME (Figure 7L).

Reduction in BMP2 activity in the aged dermal microenvironment reduces invasion and increases tumor sensitivity to targeted therapy

We next asked whether reduction in BMP2 levels could make tumors responsive to targeted therapy. Since no mBmp2 neutralization antibody was commercially available, we relied on naturally occurring BMP2 antagonists. NOGGIN binds BMP2 and BMP4 with high affinity,[73] preventing them from binding to their surface receptors and disabling their signal transduction in target cells.[74] Pretreatment with recombinant human NOGGIN (rhNOGGIN) (0.5 μg/mL) reduces rBMP2 (100 ng/mL)-mediated SMAD1/5 and ERK1/2 activation in WM983b melanoma cells (Figure S11E). rhNOGGIN with aged male fibroblast-derived CM inhibits AXL upregulation (Figure S11F). rhNOGGIN negates the reduction in proliferation imposed by aged male fibroblast CM (Figures 7M and S11G), reduces invasion in melanoma spheroids (Figures 7N and S11H), and increases responsiveness to BRAFi/MEKi (Figures 7O and S11I). *In vivo*, aged male C57BL/6 mice injected with Yumm1.7-mCherry and treated with rmNoggin showed increased tumor growth and greater response to BRAFi/MEKi, including complete regression in some mice and later relapse (Figure 7P). This supports that reducing BMP2 activity reverts melanoma tumors from a slow-cycling, invasive, therapy-resistant phenotype to a more proliferative, therapy-sensitive phenotype.

DISCUSSION

Recent studies have highlighted an age-independent female advantage following BRAF- and/or MEK-targeted therapy.[24,75] Studies highlighting sexually dimorphic biological aging have only just started to emerge due to overt use of male subjects in preclinical and clinical research.[76] Therefore, we have extended our work to include both sex and age to ascertain the role of the TME in cutaneous melanoma progression and therapy response. Limited evidence suggests that male C57BL/6 mice age faster

(D) Representative images of Yumm1.7-mCherry and BSC9AJ2-mCherry primary tumors from mice cohorts stained for Bmp2 ($n = 4$ mice per group). Scale bars show 50 μm.

(E) Tumor growth measurement of Yumm1.7-mCherry injected intradermally in immunocompetent C57BL/6 young male (8 weeks) mice and administered with recombinant murine Bmp2 (rmBmp2) (1 μg) or PBS intratumor every alternate day (****$p < 0.0001$, ***$p < 0.001$, $n = 7$ mice per group).

(F) Representative images of primary tumors from mice in (E) for Bmp2, Ki-67, Wnt5a, Mitf, Axl, γH2ax (Ser139), activated Smad1/5 (pSmad1/5), and activated Erk1/2 (pErk1/2) ($n = 5$ mice per group). Scale bars show 50 μm.

(G) Histological analysis of melanoma metastasis to the lung stained with mCherry (indicated with black arrows) in young male C57BL/6 mice from (E). Quantification of single melanoma cell metastasis per high-power field (HPF) (**$p < 0.01$, $n = 7$ mice per group). Scale bars show 50 μm.

(H) Quantification of cell death (total intensity of ethidium homodimer-1) relative to spheroid area (calcein-AM) following PBS or rBMP2 pretreatment (100 ng/mL) prior to BRAFi/MEKi inhibition is represented as relative cell death compared with DMSO treatment (***$p < 0.001$, **$p < 0.01$, $n = 4$).

(I) Tumor growth measurement of Yumm1.7-mCherry injected intradermally in immunocompetent C57BL/6 young male (8 weeks) mice and administered with rmBmp2 (1 μg per mouse) or PBS intratumor every alternate day. Mice were further randomized to receive diet containing control chow (chow) or BRAFi/MEKi chow (BRAFi/MEKi) *ad libitum* (****$p < 0.0001$, $n = 5$ mice per group).

(J) Representative images of Yumm1.7-mCherry primary tumors from mice fed control chow (naive) or BRAFi/MEKi chow (resistant) stained for Bmp2 ($n = 4$ mice per group). Scale bars show 50 μm.

(K) Immunoblot analysis of BMP2, ERK1/2 reactivation, invasive signature (AXL, WNT5A [black arrow]), and proliferative signature (MITF) in BRAFi (PLX4720) resistant melanoma cell lines maintained in PLX4720 for over 8 weeks in comparison with DMSO control and PLX4720 treatment (48 h). HSP90 was used as a loading control.

(L) Diagram of BMP2-mediated intrinsic resistance in the aged male tumor microenvironment and acquired resistance to targeted therapy in young male tumor microenvironment. Created with Biorender.com.

(M) Quantification of BrdU incorporation in melanoma lines subjected to PBS (mock), rBMP2 (100 ng/mL), and recombinant human NOGGIN (rhNOGGIN; 1 μg/mL) in normal growth media or conditioned media from aged male fibroblasts alone or in combination with rhNOGGIN for 48 h (***$p < 0.001$, **$p < 0.01$, *$p < 0.01$, $n = 3$).

(N) Representative images for WM983b spheroid invasion following treatment with PBS (mock), rhNOGGIN (1 μg/mL), and rBMP2 (100 ng/mL) in normal growth media, aged male fibroblast-derived conditioned media alone, or in combination with rhNOGGIN for 72 h. Invaded area is outlined in green. Quantification of melanoma spheroids shown as percent invasion relative to 0 h (****$p < 0.0001$, ***$p < 0.001$, $n = 4$). Scale bars show 100 μm.

(O) Viability assay on WM983b melanoma spheroids treated with normal growth media or aged male fibroblast-conditioned media in combination with rhNOGGIN or PBS with 3 μM PLX4720 (BRAFi) and 500 nM PD0325901 (MEKi) or DMSO (mock) for 48 h. Viability was assessed by staining with calcein-AM (green) and ethidium homodimer-1 (red/orange), indicating live and dead cells, respectively. Graph representing relative cell death (total intensity of ethidium homodimer-1 to spheroid area) following BRAFi/MEKi treatment compared with DMSO treatment (****$p < 0.0001$, **$p < 0.01$, $n = 3$). Scale bars show 50 μm.

(P) Tumor growth measurement of Yumm1.7-mCherry injected intradermally in C57BL/6 aged male (>52 weeks) mice and administered with rmNoggin (2 μg per mouse) or PBS intratumor every alternate day. Mice were further randomized to receive diet containing control chow (chow) or BRAFi/MEKi chow (BRAFi/MEKi) *ad libitum* (****$p < 0.0001$, $n = 5$ mice per group).

Values are presented as mean ± SEM.

See also Figures S10 and S11 and Data S1.

than age-matched female littermates.[30] While senescence is ubiquitous across the lifespan, it has long been considered an important hallmark of aging.[77] While aging promotes senescence, other factors like DNA damage can also induce it. Young female fibroblasts achieved senescence without SASP, while male fibroblasts proliferated until aging, then entered senescence with robust SASP. Aged C57BL/6 mice show higher senescence markers in males compared with females.[78] Interestingly, an accelerated aging phenotype has been reported in immune cell populations in men,[79] suggesting that the rate of chronological aging at the cellular level is potentially sexually dimorphic and would support the longer health and lifespan in females than males.[34,80]

Sexual dimorphism in melanoma is dependent on the differences in sex chromosomes and hormone levels.[81] Sex chromosomes and hormones impact the TME, including stromal cells. Increased mitochondrial ROS in aged male fibroblasts promotes mitochondrial dysfunction,[82] observed in melanoma cells exposed to aged fibroblast-derived CM and in aged mouse tumors. Elevated oxidative stress can increase tumor mutation burden, producing neoantigens[83] and predicting ICB efficacy in melanoma.[84,85] This high tumor mutation burden may explain better overall survival reported in male metastatic melanoma patients undergoing immune checkpoint blockade therapy.[21,86,87] Our data in the $BRAF^{V600E}$ mutant melanoma model clearly show that the differentially secreted factors within the TME can dictate therapy responses based on the age and sex of the host. It is also imperative to highlight that although to a lesser extent than aged male mice, aged female mice also showed a significant increase in lung metastasis as compared with young female mice. This emphasizes that melanoma progression is promoted by other sex-independent but age-dependent biochemical factors in the TME, which further suggests that the local microenvironment plays an even more important role in tumorigenesis.

One such secreted factor, BMP2, was selectively secreted by the aged male fibroblasts and may be epigenetically regulated. The *BMP2* gene resides in an area referred to as a "gene desert" and is essential for osteogenic, chondrogenic, and adipogenic programs.[88] Mouse embryonic fibroblasts transduced with oncogenic Ras and Raf have been shown to activate p16 (senescence) and Bmp2, accompanied by a reduction in Ezh2 enrichment and H3K27me3 repression around *Bmp2*.[89,90] In addition, decline in H3K27me3 promotes senescence via p16 upregulation and activates SASP genes without DDR.[41] Age-mediated decline in EZH2 and H3K27me3 in male fibroblasts increased BMP2, supporting a role for DDR and epigenetics in BMP2 induction. Increased BMP2 post-therapy resistance can facilitate premature senescence in neighboring fibroblasts. Primary melanomas express activated SMAD1/5/8, a marker of canonical BMP activity.[91] BMP2 mediates non-canonical ERK1/2 pathway in melanoma cells.[57] BMP2 likely promotes intrinsic resistance to targeted therapy through residual ERK1/2 activation. Treatment with NOGGIN, a known inhibitor of BMP2/4,[92] reduced BMP2 signaling, improving targeted therapy response and delaying tumor relapse in aged male tumors.

Our data on the sex-dependent role of aging TME highlights two key points: first, the importance of including sex and age as a variable in clinical trial design and preclinical animal models and, second, in melanoma prognosis and decision-making regarding choice of treatment modalities. Understanding sex differences in melanoma and intrinsic cellular changes with age will aid in identifying new pharmacological vulnerabilities toward personalized therapies that influence both tumor aggressiveness and treatment response.

Limitations of the study

Melanoma remains a hormone-responsive tumor, and while the effects of sex steroids and receptors on melanoma cells are recognized,[23,24,93–95] they can be contradictory. Within this context, the impact of physiological concentrations of sex hormones on dermal fibroblasts and melanoma TME in the context of aging remains unknown. Our study shows BMP2 secretion in the aged male TME is independent of the melanoma driver mutations; however, investigation of the effect BMP2 has on melanoma progression and therapy response in tumor cells harboring mutations other than $BRAF^{V600E}$ is warranted. Similarly, any effect of BMP2 on immune cells and tumor infiltration needs to be determined. Our study described BMP2-mediated resistance to BRAF/MEK inhibition and targeted therapy-induced increase in BMP2 secretion. However, we need to determine the effect of the dermal microenvironment secreted BMP2 on immune checkpoint therapy. It has been shown that sex plays a critical role in response to immune checkpoint blockade, and specifically, androgen receptor activity in T cells has been shown to inhibit response to checkpoint blockade.[96]

RESOURCE AVAILABILITY

Lead contact

Further information and requests for resources and reagents should be directed to and will be fulfilled by the lead contact, Dr. Ashani T. Weeraratna (aweerar1@jhu.edu).

Materials availability

All materials used in this study are commercially available, as specified in the key resources table. All unique/stable reagents generated in this study are available from the lead contact (aweerar1@jhu.edu) with a completed Materials Transfer Agreement.

Data and code availability

- Raw data for western blot figure panels were deposited on Mendeley at http://www.doi.org/10.17632/stdwp2tmy4.1.
- This manuscript does not report original code.
- Any additional information required to reanalyze the data reported in this paper is available from the lead contact upon request.

ACKNOWLEDGMENTS

We thank Mrs. Weiyun Sun for administrative assistance and Dr. Hsin-Yao Tang and Dr. David Speicher from Proteomics Facilities at Wistar Institute, supported by P30CA010815. We would like to thank the outstanding Histology Core Facilities of the Johns Hopkins Kimmel Cancer Center, supported by P30CA00697356 (NCI). Y.C. was supported by U01CA227550 (NCI). M.E.F. was supported by P01CA114046 (NCI), R01CA207935 (NCI), and K99CA263017 (NCI) and is currently supported by R00CA263017-02. G.E.M.-B. is supported by NRSA pre-doctoral fellowship 1F31CA261065-01A1 (NCI) and R01CA232256 (NCI). V.W. is supported by T32CA153952

(NIH). A.E.C. is supported by R01CA232256 (NCI) and GT15667 (HHMI). D.J.Z. is supported by the Conquer Cancer Foundation Young Investigator Award, the Cholangiocarcinoma Foundation Research Fellowship, MD Anderson GI SPORE Career Enhancement Program, the Maryland Cancer Moonshot Grant to the Johns Hopkins Medical Institutions (FY24), and NIH 5T32CA009071-40. K.B. and J.C.S. are recipients of Career Development Awards from the Dermatology Foundation. H.J. and R.Z. are supported by R01HG010889 (NIH). L.H. was supported by HU 2900/1-1 Deutsche Forschungsgemeinschaft (DFG). E.I.H. is supported by K00AG068527 (NIA). A.T.W. is supported by a Team Science Award from the Melanoma Research Alliance. A.T.W. is also supported by P01CA114046 (NCI), U01CA227550 (NCI), R01CA232256 (NCI), R01CA207935 (NCI), a Bloomberg Distinguished Professorship, and the EV McCollum Endowed Chair. We also thank the summer trainees and rotation students who participated in this study.

AUTHOR CONTRIBUTIONS

A.T.W. and Y.C. conceived the project. Y.C. designed the project and experiments. Y.C. performed, analyzed, and interpreted most of the experiments performed on dermal fibroblasts and was assisted by S.P., L.H., M.L.B., E.K., K.T., G.E.M.-B., and A.E.C. CM experiments were performed by Y.C., K.T., and E.I.H. Age- and sex-dependent mouse experiments were performed and interpreted by Y.C. and assisted by S.P., M.E.F., D.J.Z., N.G., and D.A.M. All rBMP2 and NOGGIN experiments *in vitro* and *in vivo* were performed by Y.C. and S.P. and assisted by L.H. and M.R.R. Immunohistochemistry was performed by Y.C., S.P., M.E.F., J.R., A.D., and A.N. BRAFi resistant cell lines were generated by Y.C. and V.W. Y.C. and M.E.F. performed bioinformatics analysis. ELISA was performed by Y.C., S.P., and L.H. Statistical analysis for mouse experiments was performed by R.Z. and H.J. Human serum was provided by E.J.L., and J.C.S. provided human melanoma sections. D.J.Z., E.M.J., and K.B. provided technical or material support. Y.C. and A.T.W. contributed to the writing of the manuscript. All authors reviewed the manuscript.

DECLARATION OF INTERESTS

A.T.W. is on the board of reGAIN Therapeutics and the Melanoma Research Foundation. E.M.J. reports other support from Abmeta, personal fees from Genocea, personal fees from Achilles, personal fees from DragonFly, personal fees from Candel Therapeutics, other support from the Parker Institute, grants and other support from Lustgarten, personal fees from Carta, grants and other support from Genentech, grants and other support from AstraZeneca, personal fees from NextCure, and grants and other support from Break Through Cancer outside of the submitted work. D.J.Z. reports grant funding (paid to Johns Hopkins University) from Roche/Genentech. Y.C. and M.E.F. are affiliated with the Cancer Signaling and Microenvironment program, FoxChase Cancer Center, Philadelphia, PA, USA.

STAR★METHODS

Detailed methods are provided in the online version of this paper and include the following:

SUPPLEMENTAL INFORMATION

Supplemental information can be found online at https://doi.org/10.1016/j.cell.2024.08.013.

Received: January 23, 2023
Revised: February 19, 2024
Accepted: August 7, 2024
Published: September 6, 2024

REFERENCES

1. Balch, C.M., Soong, S.J., Gershenwald, J.E., Thompson, J.F., Coit, D.G., Atkins, M.B., Ding, S., Cochran, A.J., Eggermont, A.M.M., Flaherty, K.T., et al. (2013). Age as a prognostic factor in patients with localized melanoma and regional metastases. Ann. Surg. Oncol. *20*, 3961–3968. https://doi.org/10.1245/s10434-013-3100-9.
2. Cavanaugh-Hussey, M.W., Mu, E.W., Kang, S., Balch, C.M., and Wang, T. (2015). Older age is associated with a higher incidence of melanoma death but a lower incidence of sentinel lymph node metastasis in the SEER databases (2003–2011). Ann. Surg. Oncol. *22*, 2120–2126. https://doi.org/10.1245/s10434-015-4538-8.
3. Leiter, U., Eigentler, T., and Garbe, C. (2014). Epidemiology of skin cancer. Adv. Exp. Med. Biol. *810*, 120–140. https://doi.org/10.1007/978-1-4939-0437-2_7.
4. Enninga, E.A.L., Moser, J.C., Weaver, A.L., Markovic, S.N., Brewer, J.D., Leontovich, A.A., Hieken, T.J., Shuster, L., Kottschade, L.A., Olariu, A., et al. (2017). Survival of cutaneous melanoma based on sex, age, and stage in the United States, 1992–2011. Cancer Med. *6*, 2203–2212. https://doi.org/10.1002/cam4.1152.
5. Atkins, M.B., Curiel-Lewandrowski, C., Fisher, D.E., Swetter, S.M., Tsao, H., Aguirre-Ghiso, J.A., Soengas, M.S., Weeraratna, A.T., Flaherty, K.T., Herlyn, M., et al. (2021). The state of melanoma: emergent challenges and opportunities. Clin. Cancer Res. *27*, 2678–2697. https://doi.org/10.1158/1078-0432.CCR-20-4092.
6. Hugo, W., Shi, H., Sun, L., Piva, M., Song, C., Kong, X., Moriceau, G., Hong, A., Dahlman, K.B., Johnson, D.B., et al. (2015). Non-genomic and immune evolution of melanoma acquiring MAPKi resistance. Cell *162*, 1271–1285. https://doi.org/10.1016/j.cell.2015.07.061.
7. Hugo, W., Zaretsky, J.M., Sun, L., Song, C., Moreno, B.H., Hu-Lieskovan, S., Berent-Maoz, B., Pang, J., Chmielowski, B., Cherry, G., et al. (2016). Genomic and transcriptomic features of response to anti-PD-1 therapy in metastatic melanoma. Cell *165*, 35–44. https://doi.org/10.1016/j.cell.2016.02.065.
8. Jerby-Arnon, L., Shah, P., Cuoco, M.S., Rodman, C., Su, M.J., Melms, J.C., Leeson, R., Kanodia, A., Mei, S., Lin, J.R., et al. (2018). A cancer cell program promotes T cell exclusion and resistance to checkpoint blockade. Cell *175*, 984–997.e24. https://doi.org/10.1016/j.cell.2018.09.006.
9. Moriceau, G., Hugo, W., Hong, A., Shi, H., Kong, X., Yu, C.C., Koya, R.C., Samatar, A.A., Khanlou, N., Braun, J., et al. (2015). Tunable-combinatorial mechanisms of acquired resistance limit the efficacy of BRAF/MEK cotargeting but result in melanoma drug addiction. Cancer Cell *27*, 240–256. https://doi.org/10.1016/j.ccell.2014.11.018.

10. Larkin, J., Chiarion-Sileni, V., Gonzalez, R., Grob, J.J., Rutkowski, P., Lao, C.D., Cowey, C.L., Schadendorf, D., Wagstaff, J., Dummer, R., et al. (2019). Five-year survival with combined Nivolumab and ipilimumab in advanced melanoma. N. Engl. J. Med. *381*, 1535–1546. https://doi.org/10.1056/NEJMoa1910836.

11. Long, G.V., Eroglu, Z., Infante, J., Patel, S., Daud, A., Johnson, D.B., Gonzalez, R., Kefford, R., Hamid, O., Schuchter, L., et al. (2018). Long-term outcomes in patients with BRAF V600-mutant metastatic melanoma who received Dabrafenib combined with trametinib. J. Clin. Oncol. *36*, 667–673. https://doi.org/10.1200/JCO.2017.74.1025.

12. Alicea, G.M., Rebecca, V.W., Goldman, A.R., Fane, M.E., Douglass, S.M., Behera, R., Webster, M.R., Kugel, C.H., 3rd, Ecker, B.L., Caino, M.C., et al. (2020). Changes in aged fibroblast lipid metabolism induce age-dependent melanoma cell resistance to targeted therapy via the fatty acid transporter FATP2. Cancer Discov. *10*, 1282–1295. https://doi.org/10.1158/2159-8290.CD-20-0329.

13. Kaur, A., Webster, M.R., Marchbank, K., Behera, R., Ndoye, A., Kugel, C.H., 3rd, Dang, V.M., Appleton, J., O'Connell, M.P., Cheng, P., et al. (2016). sFRP2 in the aged microenvironment drives melanoma metastasis and therapy resistance. Nature *532*, 250–254. https://doi.org/10.1038/nature17392.

14. Garcovich, S., Colloca, G., Sollena, P., Andrea, B., Balducci, L., Cho, W.C., Bernabei, R., and Peris, K. (2017). Skin cancer epidemics in the elderly as an emerging issue in geriatric oncology. Aging Dis. *8*, 643–661. https://doi.org/10.14336/AD.2017.0503.

15. Fane, M., and Weeraratna, A.T. (2020). How the ageing microenvironment influences tumour progression. Nat. Rev. Cancer *20*, 89–106. https://doi.org/10.1038/s41568-019-0222-9.

16. Lasithiotakis, K., Leiter, U., Meier, F., Eigentler, T., Metzler, G., Moehrle, M., Breuninger, H., and Garbe, C. (2008). Age and gender are significant independent predictors of survival in primary cutaneous melanoma. Cancer *112*, 1795–1804. https://doi.org/10.1002/cncr.23359.

17. Cook, M.B., Dawsey, S.M., Freedman, N.D., Inskip, P.D., Wichner, S.M., Quraishi, S.M., Devesa, S.S., and McGlynn, K.A. (2009). Sex disparities in cancer incidence by period and age. Cancer Epidemiol. Biomarkers Prev. *18*, 1174–1182. https://doi.org/10.1158/1055-9965.EPI-08-1118.

18. Cook, M.B., McGlynn, K.A., Devesa, S.S., Freedman, N.D., and Anderson, W.F. (2011). Sex disparities in cancer mortality and survival. Cancer Epidemiol. Biomarkers Prev. *20*, 1629–1637. https://doi.org/10.1158/1055-9965.EPI-11-0246.

19. Joosse, A., Collette, S., Suciu, S., Nijsten, T., Lejeune, F., Kleeberg, U.R., Coebergh, J.W.W., Eggermont, A.M.M., and de Vries, E. (2012). Superior outcome of women with stage I/II cutaneous melanoma: pooled analysis of four European Organisation for Research and Treatment of Cancer phase III trials. J. Clin. Oncol. *30*, 2240–2247. https://doi.org/10.1200/JCO.2011.38.0584.

20. Joosse, A., de Vries, E., Eckel, R., Nijsten, T., Eggermont, A.M.M., Hölzel, D., Coebergh, J.W.W., and Engel, J.; Munich Melanoma Group (2011). Gender differences in melanoma survival: female patients have a decreased risk of metastasis. J. Invest. Dermatol. *131*, 719–726. https://doi.org/10.1038/jid.2010.354.

21. McQuade, J.L., Daniel, C.R., Hess, K.R., Mak, C., Wang, D.Y., Rai, R.R., Park, J.J., Haydu, L.E., Spencer, C., Wongchenko, M., et al. (2018). Association of body-mass index and outcomes in patients with metastatic melanoma treated with targeted therapy, immunotherapy, or chemotherapy: a retrospective, multicohort analysis. Lancet Oncol. *19*, 310–322. https://doi.org/10.1016/S1470-2045(18)30078-0.

22. Klein, S.L., and Flanagan, K.L. (2016). Sex differences in immune responses. Nat. Rev. Immunol. *16*, 626–638. https://doi.org/10.1038/nri.2016.90.

23. Natale, C.A., Li, J., Zhang, J., Dahal, A., Dentchev, T., Stanger, B.Z., and Ridky, T.W. (2018). Activation of G protein-coupled estrogen receptor signaling inhibits melanoma and improves response to immune checkpoint blockade. eLife *7*, e31770. https://doi.org/10.7554/eLife.31770.

24. Vellano, C.P., White, M.G., Andrews, M.C., Chelvanambi, M., Witt, R.G., Daniele, J.R., Titus, M., McQuade, J.L., Conforti, F., Burton, E.M., et al. (2022). Androgen receptor blockade promotes response to BRAF/MEK-targeted therapy. Nature *606*, 797–803. https://doi.org/10.1038/s41586-022-04833-8.

25. Mervic, L. (2012). Time course and pattern of metastasis of cutaneous melanoma differ between men and women. PLoS One *7*, e32955. https://doi.org/10.1371/journal.pone.0032955.

26. Joosse, A., Collette, S., Suciu, S., Nijsten, T., Patel, P.M., Keilholz, U., Eggermont, A.M.M., Coebergh, J.W.W., and de Vries, E. (2013). Sex is an independent prognostic indicator for survival and relapse/progression-free survival in metastasized stage III to IV melanoma: a pooled analysis of five European Organisation for Research and Treatment of Cancer randomized controlled trials. J. Clin. Oncol. *31*, 2337–2346. https://doi.org/10.1200/JCO.2012.44.5031.

27. Tas, F., and Erturk, K. (2019). Relapse patterns in patients with local and regional cutaneous melanoma. Clin. Transl. Oncol. *21*, 412–419. https://doi.org/10.1007/s12094-018-1938-9.

28. Rubin, J.B. (2022). The spectrum of sex differences in cancer. Trends Cancer *8*, 303–315. https://doi.org/10.1016/j.trecan.2022.01.013.

29. Bronikowski, A.M., Altmann, J., Brockman, D.K., Cords, M., Fedigan, L.M., Pusey, A., Stoinski, T., Morris, W.F., Strier, K.B., and Alberts, S.C. (2011). Aging in the natural world: comparative data reveal similar mortality patterns across primates. Science *331*, 1325–1328. https://doi.org/10.1126/science.1201571.

30. Davis, E.J., Lobach, I., and Dubal, D.B. (2019). Female XX sex chromosomes increase survival and extend lifespan in aging mice. Aging Cell *18*, e12871. https://doi.org/10.1111/acel.12871.

31. Zarulli, V., Barthold Jones, J.A., Oksuzyan, A., Lindahl-Jacobsen, R., Christensen, K., and Vaupel, J.W. (2018). Women live longer than men even during severe famines and epidemics. Proc. Natl. Acad. Sci. USA *115*, E832–E840. https://doi.org/10.1073/pnas.1701535115.

32. Fane, M.E., Chhabra, Y., Alicea, G.M., Maranto, D.A., Douglass, S.M., Webster, M.R., Rebecca, V.W., Marino, G.E., Almeida, F., Ecker, B.L., et al. (2022). Stromal changes in the aged lung induce an emergence from melanoma dormancy. Nature *606*, 396–405. https://doi.org/10.1038/s41586-022-04774-2.

33. Kaur, A., Ecker, B.L., Douglass, S.M., Kugel, C.H., 3rd, Webster, M.R., Almeida, F.V., Somasundaram, R., Hayden, J., Ban, E., Ahmadzadeh, H., et al. (2019). Remodeling of the collagen matrix in aging skin promotes melanoma metastasis and affects immune cell motility. Cancer Discov. *9*, 64–81. https://doi.org/10.1158/2159-8290.CD-18-0193.

34. Hägg, S., and Jylhävä, J. (2021). Sex differences in biological aging with a focus on human studies. eLife *10*, e63425. https://doi.org/10.7554/eLife.63425.

35. Haupt, S., Caramia, F., Klein, S.L., Rubin, J.B., and Haupt, Y. (2021). Sex disparities matter in cancer development and therapy. Nat. Rev. Cancer *21*, 393–407. https://doi.org/10.1038/s41568-021-00348-y.

36. Park, H.W. (2013). Biological aging and social characteristics: gerontology, the Baltimore city hospitals, and the National Institutes of Health. J. Hist. Med. Allied Sci. *68*, 49–86. https://doi.org/10.1093/jhmas/jrr048.

37. Korosec, A., Frech, S., Gesslbauer, B., Vierhapper, M., Radtke, C., Petzelbauer, P., and Lichtenberger, B.M. (2019). Lineage identity and location within the dermis determine the function of papillary and reticular fibroblasts in human skin. J. Invest. Dermatol. *139*, 342–351. https://doi.org/10.1016/j.jid.2018.07.033.

38. Sahai, E., Astsaturov, I., Cukierman, E., DeNardo, D.G., Egeblad, M., Evans, R.M., Fearon, D., Greten, F.R., Hingorani, S.R., Hunter, T., et al. (2020). A framework for advancing our understanding of cancer-associated fibroblasts. Nat. Rev. Cancer *20*, 174–186. https://doi.org/10.1038/s41568-019-0238-1.

39. Chhabra, Y., and Weeraratna, A.T. (2023). Fibroblasts in cancer: unity in heterogeneity. Cell *186*, 1580–1609. https://doi.org/10.1016/j.cell.2023.03.016.

40. Berthois, Y., Katzenellenbogen, J.A., and Katzenellenbogen, B.S. (1986). Phenol red in tissue culture media is a weak estrogen: implications concerning the study of estrogen-responsive cells in culture. Proc. Natl. Acad. Sci. USA *83*, 2496–2500. https://doi.org/10.1073/pnas.83.8.2496.

41. Ito, T., Teo, Y.V., Evans, S.A., Neretti, N., and Sedivy, J.M. (2018). Regulation of cellular senescence by polycomb chromatin modifiers through distinct DNA damage- and histone methylation-dependent pathways. Cell Rep. *22*, 3480–3492. https://doi.org/10.1016/j.celrep.2018.03.002.

42. Freund, A., Patil, C.K., and Campisi, J. (2011). P38MAPK is a novel DNA damage response-independent regulator of the senescence-associated secretory phenotype. EMBO J. *30*, 1536–1548. https://doi.org/10.1038/emboj.2011.69.

43. Kim, H.S., Song, M.C., Kwak, I.H., Park, T.J., and Lim, I.K. (2003). Constitutive induction of p-Erk1/2 accompanied by reduced activities of protein phosphatases 1 and 2A and MKP3 due to reactive oxygen species during cellular senescence. J. Biol. Chem. *278*, 37497–37510. https://doi.org/10.1074/jbc.M211739200.

44. Todd, D.E., Densham, R.M., Molton, S.A., Balmanno, K., Newson, C., Weston, C.R., Garner, A.P., Scott, L., and Cook, S.J. (2004). ERK1/2 and p38 cooperate to induce a p21Cip1-dependent G1 cell cycle arrest. Oncogene *23*, 3284–3295. https://doi.org/10.1038/sj.onc.1207467.

45. Alimirah, F., Pulido, T., Valdovinos, A., Alptekin, S., Chang, E., Jones, E., Diaz, D.A., Flores, J., Velarde, M.C., Demaria, M., et al. (2020). Cellular senescence promotes skin carcinogenesis through p38MAPK and p44/42MAPK signaling. Cancer Res. *80*, 3606–3619. https://doi.org/10.1158/0008-5472.CAN-20-0108.

46. Coppé, J.P., Desprez, P.Y., Krtolica, A., and Campisi, J. (2010). The senescence-associated secretory phenotype: the dark side of tumor suppression. Annu. Rev. Pathol. *5*, 99–118. https://doi.org/10.1146/annurev-pathol-121808-102144.

47. Schafer, M.J., Zhang, X., Kumar, A., Atkinson, E.J., Zhu, Y., Jachim, S., Mazula, D.L., Brown, A.K., Berning, M., Aversa, Z., et al. (2020). The senescence-associated secretome as an indicator of age and medical risk. JCI Insight *5*, e133668. https://doi.org/10.1172/jci.insight.133668.

48. Rodier, F., Coppé, J.P., Patil, C.K., Hoeijmakers, W.A.M., Muñoz, D.P., Raza, S.R., Freund, A., Campeau, E., Davalos, A.R., and Campisi, J. (2009). Persistent DNA damage signalling triggers senescence-associated inflammatory cytokine secretion. Nat. Cell Biol. *11*, 973–979. https://doi.org/10.1038/ncb1909.

49. Coppé, J.P., Rodier, F., Patil, C.K., Freund, A., Desprez, P.Y., and Campisi, J. (2011). Tumor suppressor and aging biomarker p16(INK4a) induces cellular senescence without the associated inflammatory secretory phenotype. J. Biol. Chem. *286*, 36396–36403. https://doi.org/10.1074/jbc.M111.257071.

50. Trimmer, C., Sotgia, F., Whitaker-Menezes, D., Balliet, R.M., Eaton, G., Martinez-Outschoorn, U.E., Pavlides, S., Howell, A., Iozzo, R.V., Pestell, R.G., et al. (2011). Caveolin-1 and mitochondrial SOD2 (MnSOD) function as tumor suppressors in the stromal microenvironment: a new genetically tractable model for human cancer associated fibroblasts. Cancer Biol. Ther. *11*, 383–394. https://doi.org/10.4161/cbt.11.4.14101.

51. Hoek, K.S., Eichhoff, O.M., Schlegel, N.C., Döbbeling, U., Kobert, N., Schaerer, L., Hemmi, S., and Dummer, R. (2008). In vivo switching of human melanoma cells between proliferative and invasive states. Cancer Res. *68*, 650–656. https://doi.org/10.1158/0008-5472.CAN-07-2491.

52. Webster, M.R., Fane, M.E., Alicea, G.M., Basu, S., Kossenkov, A.V., Marino, G.E., Douglass, S.M., Kaur, A., Ecker, B.L., Gnanapradeepan, K., et al. (2020). Paradoxical role for wild-type p53 in driving therapy resistance in melanoma. Mol. Cell *77*, 633–644.e5. https://doi.org/10.1016/j.molcel.2019.11.009.

53. Lopez-Fabuel, I., Le Douce, J., Logan, A., James, A.M., Bonvento, G., Murphy, M.P., Almeida, A., and Bolaños, J.P. (2016). Complex I assembly into supercomplexes determines differential mitochondrial ROS production in neurons and astrocytes. Proc. Natl. Acad. Sci. USA *113*, 13063–13068. https://doi.org/10.1073/pnas.1613701113.

54. Meeth, K., Wang, J.X., Micevic, G., Damsky, W., and Bosenberg, M.W. (2016). The YUMM lines: a series of congenic mouse melanoma cell lines with defined genetic alterations. Pigment Cell Melanoma Res. *29*, 590–597. https://doi.org/10.1111/pcmr.12498.

55. Viros, A., Sanchez-Laorden, B., Pedersen, M., Furney, S.J., Rae, J., Hogan, K., Ejiama, S., Girotti, M.R., Cook, M., Dhomen, N., et al. (2014). Ultraviolet radiation accelerates BRAF-driven melanomagenesis by targeting TP53. Nature *511*, 478–482. https://doi.org/10.1038/nature13298.

56. Fane, M.E., Chhabra, Y., Hollingsworth, D.E.J., Simmons, J.L., Spoerri, L., Oh, T.G., Chauhan, J., Chin, T., Harris, L., Harvey, T.J., et al. (2017). NFIB mediates BRN2 driven melanoma cell migration and invasion through regulation of EZH2 and MITF. EBioMedicine *16*, 63–75. https://doi.org/10.1016/j.ebiom.2017.01.013.

57. Gao, J., Muroya, R., Huang, F., Nagata, K., Shin, M., Nagano, R., Tajiri, Y., Fujii, S., Yamaza, T., Aoki, K., et al. (2021). Bone morphogenetic protein induces bone invasion of melanoma by epithelial-mesenchymal transition via the Smad1/5 signaling pathway. Lab. Invest. *101*, 1475–1483. https://doi.org/10.1038/s41374-021-00661-y.

58. Busch, C., Drews, U., Garbe, C., Eisele, S.R., and Oppitz, M. (2007). Neural crest cell migration of mouse B16-F1 melanoma cells transplanted into the chick embryo is inhibited by the BMP-antagonist noggin. Int. J. Oncol. *31*, 1367–1378. https://doi.org/10.3892/ijo.31.6.1367.

59. Sinnberg, T., Levesque, M.P., Krochmann, J., Cheng, P.F., Ikenberg, K., Meraz-Torres, F., Niessner, H., Garbe, C., and Busch, C. (2018). Wnt-signaling enhances neural crest migration of melanoma cells and induces an invasive phenotype. Mol. Cancer *17*, 59. https://doi.org/10.1186/s12943-018-0773-5.

60. Sinnberg, T., Niessner, H., Levesque, M.P., Dettweiler, C., Garbe, C., and Busch, C. (2018). Embryonic bone morphogenetic protein and nodal induce invasion in melanocytes and melanoma cells. Biol. Open *7*, bio032656. https://doi.org/10.1242/bio.032656.

61. Orgaz, J.L., Crosas-Molist, E., Sadok, A., Perdrix-Rosell, A., Maiques, O., Rodriguez-Hernandez, I., Monger, J., Mele, S., Georgouli, M., Bridgeman, V., et al. (2020). Myosin II reactivation and cytoskeletal remodeling as a hallmark and a vulnerability in melanoma therapy resistance. Cancer Cell *37*, 85–103.e9. https://doi.org/10.1016/j.ccell.2019.12.003.

62. Cao, R., Wang, L., Wang, H., Xia, L., Erdjument-Bromage, H., Tempst, P., Jones, R.S., and Zhang, Y. (2002). Role of histone H3 lysine 27 methylation in Polycomb-group silencing. Science *298*, 1039–1043. https://doi.org/10.1126/science.1076997.

63. Lau-Corona, D., Bae, W.K., Hennighausen, L., and Waxman, D.J. (2020). Sex-biased genetic programs in liver metabolism and liver fibrosis are controlled by EZH1 and EZH2. PLOS Genet. *16*, e1008796. https://doi.org/10.1371/journal.pgen.1008796.

64. Li, J., Hart, R.P., Mallimo, E.M., Swerdel, M.R., Kusnecov, A.W., and Herrup, K. (2013). EZH2-mediated H3K27 trimethylation mediates neurodegeneration in Ataxia-telangiectasia. Nat. Neurosci. *16*, 1745–1753. https://doi.org/10.1038/nn.3564.

65. Chandler, R.L., Chandler, K.J., McFarland, K.A., and Mortlock, D.P. (2007). Bmp2 transcription in osteoblast progenitors is regulated by a distant 3′ enhancer located 156.3 kilobases from the promoter. Mol. Cell. Biol. *27*, 2934–2951. https://doi.org/10.1128/MCB.01609-06.

66. Christiaen, L., Stolfi, A., and Levine, M. (2010). BMP signaling coordinates gene expression and cell migration during precardiac mesoderm development. Dev. Biol. *340*, 179–187. https://doi.org/10.1016/j.ydbio.2009.11.006.

67. Schwarting, T., Schenk, D., Frink, M., Benölken, M., Steindor, F., Oswald, M., Ruchholtz, S., and Lechler, P. (2016). Stimulation with bone morphogenetic protein-2 (BMP-2) enhances bone-tendon integration in vitro. Connect. Tissue Res. *57*, 99–112. https://doi.org/10.3109/03008207.2015.1087516.

68. Martinez-Hackert, E., Sundan, A., and Holien, T. (2021). Receptor binding competition: A paradigm for regulating TGF-beta family action. Cytokine Growth Factor Rev. *57*, 39–54. https://doi.org/10.1016/j.cytogfr.2020.09.003.

69. Ramachandran, A., Vizán, P., Das, D., Chakravarty, P., Vogt, J., Rogers, K.W., Müller, P., Hinck, A.P., Sapkota, G.P., and Hill, C.S. (2018). TGF-beta uses a novel mode of receptor activation to phosphorylate SMAD1/5 and induce epithelial-to-mesenchymal transition. eLife *7*, e31756. https://doi.org/10.7554/eLife.31756.

70. Novoyatleva, T., Rai, N., Kojonazarov, B., Veeroju, S., Ben-Batalla, I., Caruso, P., Shihan, M., Presser, N., Götz, E., Lepper, C., et al. (2021). Deficiency of Axl aggravates pulmonary arterial hypertension via BMPR2. Commun. Biol. *4*, 1002. https://doi.org/10.1038/s42003-021-02531-1.

71. Reichl, P., Dengler, M., van Zijl, F., Huber, H., Führlinger, G., Reichel, C., Sieghart, W., Peck-Radosavljevic, M., Grubinger, M., and Mikulits, W. (2015). Axl activates autocrine transforming growth factor-beta signaling in hepatocellular carcinoma. Hepatology *61*, 930–941. https://doi.org/10.1002/hep.27492.

72. Obenauf, A.C., Zou, Y., Ji, A.L., Vanharanta, S., Shu, W., Shi, H., Kong, X., Bosenberg, M.C., Wiesner, T., Rosen, N., et al. (2015). Therapy-induced tumour secretomes promote resistance and tumour progression. Nature *520*, 368–372. https://doi.org/10.1038/nature14336.

73. Botchkarev, V.A. (2003). Bone morphogenetic proteins and their antagonists in skin and hair follicle biology. J. Invest. Dermatol. *120*, 36–47. https://doi.org/10.1046/j.1523-1747.2003.12002.x.

74. Groppe, J., Greenwald, J., Wiater, E., Rodriguez-Leon, J., Economides, A.N., Kwiatkowski, W., Affolter, M., Vale, W.W., Izpisua Belmonte, J.C., and Choe, S. (2002). Structural basis of BMP signalling inhibition by the cystine knot protein Noggin. Nature *420*, 636–642. https://doi.org/10.1038/nature01245.

75. Pala, L., De Pas, T., Pagan, E., Minucci, S., Catania, C., Digiacomo, N., Cocorocchio, E., Laszlo, D., Di Muzio, A., Barigazzi, C., et al. (2023). Improved outcomes in women with BRAF-mutant melanoma treated with BRAF/MEK-targeted therapy across randomized clinical trials. A systematic review and meta-analysis. Semin. Oncol. *50*, 34–39. https://doi.org/10.1053/j.seminoncol.2023.03.003.

76. Smarr, B., and Kriegsfeld, L.J. (2022). Female mice exhibit less overall variance, with a higher proportion of structured variance, than males at multiple timescales of continuous body temperature and locomotive activity records. Biol. Sex Differ. *13*, 41. https://doi.org/10.1186/s13293-022-00451-1.

77. López-Otín, C., Blasco, M.A., Partridge, L., Serrano, M., and Kroemer, G. (2013). The hallmarks of aging. Cell *153*, 1194–1217. https://doi.org/10.1016/j.cell.2013.05.039.

78. Yousefzadeh, M.J., Zhao, J., Bukata, C., Wade, E.A., McGowan, S.J., Angelini, L.A., Bank, M.P., Gurkar, A.U., McGuckian, C.A., Calubag, M.F., et al. (2020). Tissue specificity of senescent cell accumulation during physiologic and accelerated aging of mice. Aging Cell *19*, e13094. https://doi.org/10.1111/acel.13094.

79. Márquez, E.J., Chung, C.H., Marches, R., Rossi, R.J., Nehar-Belaid, D., Eroglu, A., Mellert, D.J., Kuchel, G.A., Banchereau, J., and Ucar, D. (2020). Sexual-dimorphism in human immune system aging. Nat. Commun. *11*, 751. https://doi.org/10.1038/s41467-020-14396-9.

80. Austad, S.N., and Fischer, K.E. (2016). Sex differences in lifespan. Cell Metab. *23*, 1022–1033. https://doi.org/10.1016/j.cmet.2016.05.019.

81. Clocchiatti, A., Cora, E., Zhang, Y., and Dotto, G.P. (2016). Sexual dimorphism in cancer. Nat. Rev. Cancer *16*, 330–339. https://doi.org/10.1038/nrc.2016.30.

82. Rong, Z., Tu, P., Xu, P., Sun, Y., Yu, F., Tu, N., Guo, L., and Yang, Y. (2021). The mitochondrial response to DNA damage. Front. Cell Dev. Biol. *9*, 669379. https://doi.org/10.3389/fcell.2021.669379.

83. Wang, P., Chen, Y., and Wang, C. (2021). Beyond tumor mutation burden: tumor neoantigen burden as a biomarker for immunotherapy and other types of therapy. Front. Oncol. *11*, 672677. https://doi.org/10.3389/fonc.2021.672677.

84. Ning, B., Liu, Y., Wang, M., Li, Y., Xu, T., and Wei, Y. (2022). The predictive value of tumor mutation burden on clinical efficacy of immune checkpoint inhibitors in melanoma: A systematic review and meta-analysis. Front. Pharmacol. *13*, 748674. https://doi.org/10.3389/fphar.2022.748674.

85. Van Allen, E.M., Miao, D., Schilling, B., Shukla, S.A., Blank, C., Zimmer, L., Sucker, A., Hillen, U., Foppen, M.H.G., Goldinger, S.M., et al. (2015). Genomic correlates of response to CTLA-4 blockade in metastatic melanoma. Science *350*, 207–211. https://doi.org/10.1126/science.aad0095.

86. Kudura, K., Basler, L., Nussbaumer, L., and Foerster, R. (2022). Sex-related differences in metastatic melanoma patients treated with immune checkpoint inhibition. Cancers (Basel) *14*, 5145. https://doi.org/10.3390/cancers14205145.

87. Jang, S.R., Nikita, N., Banks, J., Keith, S.W., Johnson, J.M., Wilson, M., and Lu-Yao, G. (2021). Association between sex and immune checkpoint inhibitor outcomes for patients with melanoma. JAMA Netw. Open *4*, e2136823. https://doi.org/10.1001/jamanetworkopen.2021.36823.

88. Rogers, M.B., Shah, T.A., and Shaikh, N.N. (2015). Turning bone morphogenetic protein 2 (BMP2) on and off in mesenchymal cells. J. Cell. Biochem. *116*, 2127–2138. https://doi.org/10.1002/jcb.25164.

89. Fujimoto, M., Mano, Y., Anai, M., Yamamoto, S., Fukuyo, M., Aburatani, H., and Kaneda, A. (2016). Epigenetic alteration to activate Bmp2-Smad signaling in Raf-induced senescence. World J. Biol. Chem. *7*, 188–205. https://doi.org/10.4331/wjbc.v7.i1.188.

90. Kaneda, A., Fujita, T., Anai, M., Yamamoto, S., Nagae, G., Morikawa, M., Tsuji, S., Oshima, M., Miyazono, K., and Aburatani, H. (2011). Activation of Bmp2-Smad1 signal and its regulation by coordinated alteration of H3K27 trimethylation in Ras-induced senescence. PLOS Genet. *7*, e1002359. https://doi.org/10.1371/journal.pgen.1002359.

91. Gramann, A.K., Frantz, W.T., Dresser, K., Gomes, C.B.F., Lian, C.G., Deng, A., and Ceol, C.J. (2021). BMP signaling promotes neural crest identity and accelerates melanoma onset. J. Invest. Dermatol. *141*, 2067–2070.e1. https://doi.org/10.1016/j.jid.2021.01.021.

92. McMahon, J.A., Takada, S., Zimmerman, L.B., Fan, C.M., Harland, R.M., and McMahon, A.P. (1998). Noggin-mediated antagonism of BMP signaling is required for growth and patterning of the neural tube and somite. Genes Dev. *12*, 1438–1452. https://doi.org/10.1101/gad.12.10.1438.

93. Ma, M., Ghosh, S., Tavernari, D., Katarkar, A., Clocchiatti, A., Mazzeo, L., Samarkina, A., Epiney, J., Yu, Y.R., Ho, P.C., et al. (2021). Sustained androgen receptor signaling is a determinant of melanoma cell growth potential and tumorigenesis. J. Exp. Med. *218*, e20201137. https://doi.org/10.1084/jem.20201137.

94. Wang, Y., Ou, Z., Sun, Y., Yeh, S., Wang, X., Long, J., and Chang, C. (2017). Androgen receptor promotes melanoma metastasis via altering the miRNA-539-3p/USP13/MITF/AXL signals. Oncogene *36*, 1644–1654. https://doi.org/10.1038/onc.2016.330.

95. Markman, J.L., Porritt, R.A., Wakita, D., Lane, M.E., Martinon, D., Noval Rivas, M., Luu, M., Posadas, E.M., Crother, T.R., and Arditi, M. (2020). Loss of testosterone impairs anti-tumor neutrophil function. Nat. Commun. *11*, 1613. https://doi.org/10.1038/s41467-020-15397-4.

96. Guan, X., Polesso, F., Wang, C., Sehrawat, A., Hawkins, R.M., Murray, S.E., Thomas, G.V., Caruso, B., Thompson, R.F., Wood, M.A., et al. (2022). Androgen receptor activity in T cells limits checkpoint blockade efficacy. Nature *606*, 791–796. https://doi.org/10.1038/s41586-022-04522-6.

97. O'Connell, M.P., Marchbank, K., Webster, M.R., Valiga, A.A., Kaur, A., Vultur, A., Li, L., Herlyn, M., Villanueva, J., Liu, Q., et al. (2013). Hypoxia induces phenotypic plasticity and therapy resistance in melanoma via

the tyrosine kinase receptors ROR1 and ROR2. Cancer Discov. *3*, 1378–1393. https://doi.org/10.1158/2159-8290.CD-13-0005.

98. Webster, M.R., Xu, M., Kinzler, K.A., Kaur, A., Appleton, J., O'Connell, M.P., Marchbank, K., Valiga, A., Dang, V.M., Perego, M., et al. (2015). Wnt5A promotes an adaptive, senescent-like stress response, while continuing to drive invasion in melanoma cells. Pigment Cell Melanoma Res. *28*, 184–195. https://doi.org/10.1111/pcmr.12330.
99. Kugel, C.H., 3rd, Douglass, S.M., Webster, M.R., Kaur, A., Liu, Q., Yin, X., Weiss, S.A., Darvishian, F., Al-Rohil, R.N., Ndoye, A., et al. (2018). Age correlates with response to anti-PD1, reflecting age-related differences in intratumoral effector and regulatory T-cell populations. Clin. Cancer Res. *24*, 5347–5356. https://doi.org/10.1158/1078-0432.CCR-18-1116.
100. Chhabra, Y., Yong, H.X.L., Fane, M.E., Soogrim, A., Lim, W., Mahiuddin, D.N., Kim, R.S.Q., Ashcroft, M., Beatson, S.A., Ainger, S.A., et al. (2018). Genetic variation in IRF4 expression modulates growth characteristics, tyrosinase expression and interferon-gamma response in melanocytic cells. Pigment Cell Melanoma Res. *31*, 51–63. https://doi.org/10.1111/pcmr.12620.
101. Debacq-Chainiaux, F., Erusalimsky, J.D., Campisi, J., and Toussaint, O. (2009). Protocols to detect senescence-associated beta-galactosidase (SA-betagal) activity, a biomarker of senescent cells in culture and in vivo. Nat. Protoc. *4*, 1798–1806. https://doi.org/10.1038/nprot.2009.191.
102. McCloy, R.A., Rogers, S., Caldon, C.E., Lorca, T., Castro, A., and Burgess, A. (2014). Partial inhibition of Cdk1 in G 2 phase overrides the SAC and decouples mitotic events. Cell Cycle *13*, 1400–1412. https://doi.org/10.4161/cc.28401.
103. Cox, J., and Mann, M. (2008). MaxQuant enables high peptide identification rates, individualized p.p.b.-range mass accuracies and proteome-wide protein quantification. Nat. Biotechnol. *26*, 1367–1372. https://doi.org/10.1038/nbt.1511.
104. Storey, J.D., and Tibshirani, R. (2003). Statistical significance for genomewide studies. Proc. Natl. Acad. Sci. USA *100*, 9440–9445. https://doi.org/10.1073/pnas.1530509100.
105. Fritsch, F.N., and Carlson, R.E. (1980). Monotone piecewise cubic interpolation. SIAM J. Numer. Anal. *17*, 238–246. https://doi.org/10.1137/0717021.
106. Davison, A.C., and Hinkley, D.V. (1997). Bootstrap Methods and Their Application (Cambridge University Press) https://doi.org/10.1017/CBO9780511802843.
107. Ndoye, A., Budina-Kolomets, A., Kugel, C.H., 3rd, Webster, M.R., Kaur, A., Behera, R., Rebecca, V.W., Li, L., Brafford, P.A., Liu, Q., et al. (2017). ATG5 mediates a positive feedback loop between Wnt signaling and autophagy in melanoma. Cancer Res. *77*, 5873–5885. https://doi.org/10.1158/0008-5472.CAN-17-0907.
108. Schneider, C.A., Rasband, W.S., and Eliceiri, K.W. (2012). NIH Image to ImageJ: 25 years of image analysis. Nat. Methods *9*, 671–675. https://doi.org/10.1038/nmeth.2089.
109. Schindelin, J., Arganda-Carreras, I., Frise, E., Kaynig, V., Longair, M., Pietzsch, T., Preibisch, S., Rueden, C., Saalfeld, S., Schmid, B., et al. (2012). Fiji: an open-source platform for biological-image analysis. Nat. Methods *9*, 676–682. https://doi.org/10.1038/nmeth.2019.
110. Bankhead, P., Loughrey, M.B., Fernández, J.A., Dombrowski, Y., McArt, D.G., Dunne, P.D., McQuaid, S., Gray, R.T., Murray, L.J., Coleman, H.G., et al. (2017). QuPath: open source software for digital pathology image analysis. Sci. Rep. *7*, 16878. https://doi.org/10.1038/s41598-017-17204-5.

STAR★METHODS

KEY RESOURCES TABLE

REAGENT or RESOURCE	SOURCE	IDENTIFIER
Antibodies		
CDKN1A (p21)	Proteintech	10355-1-AP; RRID: AB_2077682
CDKN2A (p16)	Millipore Sigma	ZRB1437; RRID:AB_3492112
Total OXPHOS antibody cocktail	Abcam	ab110413; RRID:AB_2629281
P-ATM (Ser1981) (D25E5)	Cell Signaling	13050; RRID:AB_2798100
ATM (D2E2)	Cell Signaling	2873; RRID:AB_2062659
BMP2	Bioss	BS-1012R:RRID:AB_10857217
CD90	Cell Signaling	13801; RRID:AB_2798316
P-RB (Ser807/811) (D20B12)	Cell Signaling	8516; RRID:AB_11178658
RB	Cell Signaling	9309; RRID:AB_823629
WNT5A biotin-labeled	R&D Systems	BAF645; RRID:AB_2215593
WNT5A (for IHC)	R&D Systems	AF645; RRID:AB_2288488
AXL	Bioss	BS-5180R; RRID:AB_11110961
MERTK	Abcam	ab184086; RRID:AB_3492113
NRF2 (Ser40)	Bioss	BSM-52179; RRID:AB_3492114
Ki-67	Novus Biologicals	NB600-1252; RRID:AB_2142376
53BP1	Novus Biologicals	BB100-304; RRID:AB_3155982
N-Cadherin	Cell Signaling	13116; RRID:AB_2687616
P-SMAD1/5 (Ser463/Ser465)	Thermo Scientific	700047; RRID:AB_2532276
SMAD1	Cell Signaling	9743; RRID:AB_2107780
XRCC1	Cell Signaling	76998; RRID:AB_2936252
P-p38 MAPK (Thr180/Tyr182)	Cell Signaling	4511; RRID:AB_2139682
p38 MAPK	Cell Signaling	9212; RRID:AB_330713
TP53	Bioss	BS-8687R; RRID:AB_3492116
MITF (for IHC)	Bioss	BS-1990R; RRID:AB_10854743
MITF (D5G7V)	Cell Signaling	12590; RRID:AB_2616024
mCherry	Abcam	ab167453; RRID:AB_2571870
p53	Cell Signaling	2527; RRID:AB_10695803
Phospho Histone H2Ax (Ser139) (20E3) (γH2Ax)	Cell Signaling	9718; RRID:AB_2118009
CAVEOLIN1	Cell Signaling	3267; RRID:AB_2275453
Phospho p44/42 MAPK (ERK1/2) (Thr202/Tyr204) (D13.14.4E)	Cell Signaling	4370; RRID:AB_2315112
P44/p42 (ERK1/2)	Cell Signaling	9102; RRID:AB_330744
Phospho Myosin Light Chain 2 (Ser19)	Cell Signaling	3671; RRID:AB_330248
Myosin Light Chain 2	Cell Signaling	8505; RRID:AB_2728760
Phospho JNK (Thr183/Tyr185) (81E11)	Cell Signaling	4668; RRID:AB_823588
JNK	Cell Signaling	9252; RRID:AB_2250373
PDGFR-α	Cell Signaling	3174; RRID:AB_2162345
PDGFR-β	Cell Signaling	3169; RRID:AB_2162497
FAP	Cell Signaling	66562; RRID:AB_2904193
VIMENTIN	Cell Signaling	5741; RRID:AB_10695459
EZH2	Cell Signaling	5246; RRID:AB_10694683
H3K27me3	Cell Signaling	9733; RRID:AB_2616029
APE1	Cell Signaling	10519; RRID:AB_3064913
SOD1	Cell Signaling	37385; RRID:AB_3073954

(*Continued on next page*)

Continued

REAGENT or RESOURCE	SOURCE	IDENTIFIER
SOD2	Cell Signaling	13141; RRID:AB_2636921
SOD3	Santa Cruz Biotechnology	sc-271170; RRID:AB_10611183
CDK4 (D9G3E)	Cell Signaling	12790; RRID:AB_2631166
CD45	Abcam	ab10558; RRID:AB_442810
BrdU (Bu20a)	Cell Signaling	5292; RRID:AB_10548898
Nitrotyrosine	Millipore Sigma	AB5411; RRID: AB_177459
HSP90	Cell Signaling	4877; RRID:AB_2233307
GAPDH (14C10)	Cell Signaling	2118; RRID:AB_561053
Thioredoxin1	Cell Signaling	2429; RRID:AB_2272594
Redox Homeostasis Signaling Antibody Kit	Cell Signaling	16815; RRID:AB_3493878
Streptavidin Ab	Fischer Scientific	NC9705430; RRID:AB_3493547
Anti-rabbit IgG, HRP linked	Cell Signaling	7074; RRID:AB_2099233
Anti-mouse IgG, HRP linked	Cell Signaling	7076; RRID:AB_330924
Alexa Fluor 647 Goat anti-Rabbit IgG (H+L)	Thermo Scientific	A21245; RRID:AB_2535813
Alexa Fluor 488 Goat anti-Rabbit IgG (H+L)	Thermo Scientific	A11008; RRID:AB_143165
Alexa Fluor 647 Goat anti-Mouse IgG (H+L)	Thermo Scientific	A21235; RRID:AB_2535804
Alexa Fluor 488 Goat anti-Mouse IgG (H+L)	Thermo Scientific	A11001; RRID:AB_2534069
BMP2/BMP4 monoclonal IgG1 (100230) (neutralization)	Thermo Scientific	MA5-23764; RRID:AB_2609468
Mouse IgG1 isotype control (neutralization)	R&D Systems	MAB002; RRID:AB_357344
DAPI	Thermo Scientific	62248
Bacterial and virus strains		
Subcloning efficiency DH5α competent Cells	Thermo Scientific	18265017
Biological samples		
Human Melanoma Tumors Stage I/II	This study	N/A
Human Plasma from Healthy and Melanoma patients	This study	N/A
Chemicals, peptides, and recombinant proteins		
Recombinant Human/Mouse/Rat BMP2	R&D Systems	355-BM
Recombinant Human NOGGIN	R&D Systems	6057-NG
Recombinant Mouse Noggin	Peprotech	250-38
Recombinant Human/Mouse/Rat BMP2	MedChemExpress	HY-P7006
KU-60019	Selleck Chemicals	S1570
GSK126	Selleck Chemicals	S7061
β-Estradiol (E2)	Sigma Aldrich	E2758
Dihydrotestosterone (DHT)	Selleck Chemicals	S4757
Doxycycline Hyclate	TCI America	D4116
PLX4720	Selleck Chem	S1152
PD0325901 (Miradametinib)	Selleck Chem	S1036
Charcoal, Dextran coated	Millipore Sigma	C6241
Radio Immunoprecipitation Buffer (RIPA)	Cell Signaling	9806
BrdU	Peprotech	5911439
Difco Nobel Agar	BD Biosciences	214230
X-Gal	Selleck Chem	S6820
Fast SYBR Green Master Mix	Applied Biosystems	4385612
Antibody diluent	Agilent Technology	S080983-2
Bovine Serum Albumin, heat shock fraction, pH7	Millipore Sigma	A7906
AEC Substrate System	Abcam	ab64252

(*Continued on next page*)

Continued

REAGENT or RESOURCE	SOURCE	IDENTIFIER
Antigen Unmasking Solution, citrate based	Vector Labs	H-3300-250
Protein Block	Abcam	ab64226
Hydrogen Peroxide Blocking reagent	Abcam	ab133273
Streptavidin Peroxidase	Abcam	ab64269
Biotinylated Goat Anti-Rabbit IgG (H+L)	Abcam	ab64256
Hematoxylin solution (Mayer's modified)	Abcam	ab220365
Collagen 1 Rat Protein, Tail	Thermo Scientific	A1048301
Molecular Probes CellROX-Green	Thermo Scientific	C10444
Molecular Probes MitoSOX-Red	Thermo Scientific	M36008
Restore Western Blot Stripping Buffer	Thermo Scientific	21059
Sodium Bicarbonate 7.5%	Thermo Scientific	25080094
VectaMount AQ Aqueous mounting medium	Vector Labs	H-5501-60
Prolong Glass antifade mountant	Thermo Scientific	P36984
ECL Prime Western Blotting System	GE Healthcare	GERPN2232
Paraformaldehyde 16%, EM grade methanol free	Electron Microscopy Sciences	15710
AIN-76A Rodent Diet	Research Diets	D10001i
Critical commercial assays		
Pierce BCA Protein Assay kit	Fisher Scientific	23225
iScript cDNA synthesis kit	Bio-Rad	1708891
RNeasy kit	Qiagen	74004
DNeasy Blood & Tissue Kit	Qiagen	69504
Human BMP2 Quantikine ELISA kit (for conditioned media)	R&D Systems	DBP200
Human BMP2 ELISA kit (for plasma and sera)	Abcam	ab119581
Relative Human Telomere Length Quantification qPCR Assay Kit	ScienCell	8908
Total Antioxidant Capacity Assay kit	Sigma Aldrich	MAK187
Cell Meter Fluorimetric Intracellular Total ROS	AAT Bioquest	22901
Live/Dead Viability/Cytotoxicity Kit	Fisher Scientific	L3224
Proteome Profiler Human XL Cytokine Array kit	R&D Systems	ARY022B
Experimental models: Cell lines		
FS4	Webster et al.[98]	N/A
FS13	Webster et al.[98]	N/A
FS5	Webster et al.[98]	N/A
FS11	Webster et al.[98]	N/A
M93-047	Webster et al.[98]	RRID:CVCL_G298
FS14	Webster et al.[98]	N/A
WM1799	Webster et al.[98]	RRID:CVCL_A341
Yumm1.7	Meeth et al.[54]	RRID:CVCL_JK16
Yumm1.7-mCherry	Fane et al.[32]	N/A
BSC9AJ2	Kugel et al.[99]	N/A
BSC9AJ2-mCherry	This study	N/A
1205Lu	Kaur et al.[13]	RRID:CVCL_5239
WM983b	Kaur et al.[13]	RRID:CVCL_6809
WM164	Kaur et al.[13]	RRID:CVCL_7928
A2058	ATCC	CRL11147; RRID:CVCL_1059
WM793	Webster et al.[98]	RRID:CVCL_8787

(*Continued on next page*)

Continued

REAGENT or RESOURCE	SOURCE	IDENTIFIER
WM2664	Prof. Meenhard Herlyn, Wistar Institute	RRID:CVCL_2765
WM46	Prof. Meenhard Herlyn, Wistar Institute	RRID:CVCL_6803
HEK293T	Fane et al.[32]	RRID:CVCL_0063
1205Lu BRAFi Resistant	This study	N/A
WM983b BRAFi Resistant	This study	N/A
WM164 BRAFi Resistant	This study	N/A
Yumm1.7 BRAFi Resistant	This study	N/A
FS13-mCherry	Ndoye et al.[107]	N/A
FS13-WNT5A	Ndoye et al.[107]	N/A
FS4-WNT5A doxycycline-inducible repression	Fane et al.[32]	N/A
Young Male Fibroblast	Coriell Institute	2003-071-032
Young Male Fibroblast	Coriell Institute	2003-071-056
Young Male Fibroblast	Coriell Institute	TP-113
Aged Male Fibroblast	Coriell Institute	AG13004
Aged Male Fibroblast	Coriell Institute	GM13335
Aged Male Fibroblast	Coriell Institute	AG09157
Young Female Fibroblast	Coriell Institute	GM04390
Young Female Fibroblast	Coriell Institute	AG02674
Young Female Fibroblast	Coriell Institute	AG11732
Aged Female Fibroblast	Coriell Institute	AG08620
Aged Female Fibroblast	Coriell Institute	AG08517
Aged Female Fibroblast	Coriell Institute	AG11726
Aged Female Fibroblast	Coriell Institute	AG07757
Aged Male Fibroblast	Coriell Institute	AG07723
Aged Male Fibroblast	Coriell Institute	AG10047
Aged Male Fibroblast	Coriell Institute	AG05186
Aged Male Fibroblast	Coriell Institute	AG05192
Aged Male Fibroblast	Coriell Institute	AG04157
Aged Female Fibroblast	Coriell Institute	AG05275
Aged Female Fibroblast	Coriell Institute	AG05844
Aged Female Fibroblast	Coriell Institute	AG07714
Aged Female Fibroblast	Coriell Institute	AG07310
Aged Male Fibroblast	Coriell Institute	AG14048
Aged Male Fibroblast	Coriell Institute	AG13369
Aged Male Fibroblast	Coriell Institute	AG12587
Aged Male Fibroblast	Coriell Institute	AG13198
Aged Female Fibroblast	Coriell Institute	AG13246
Aged Female Fibroblast	Coriell Institute	AG12927
Aged Female Fibroblast	Coriell Institute	AG13358
Aged Female Fibroblast	Coriell Institute	AG13144
Experimental models: Organisms/strains		
C57BL/6 young (8 weeks) male mice	Charles River	556
C57BL/6 young (8 weeks) female mice	Charles River	556
C57BL/6 aged (>52 weeks) retired male breeder	Charles River	556
C57BL/6 aged (>52 weeks) retired female breeder	Charles River	556

(*Continued on next page*)

Continued

REAGENT or RESOURCE	SOURCE	IDENTIFIER
Oligonucleotides		
Primers for *18s*, *EZH2*, *BMP2*, *BMP4*, *BMP6*, *BMP7*, *GDF6*, *BMPR1A BMPR1B*, *BMPR2*, *NOG*, *BMPER*,	IDT Technology	Table S2
Recombinant DNA		
pLV[Exp]-EGFP/Puro-CMV>Stuffer300	Vector Builder	VB181209-1075efx
pLV[Exp]-Puro- EF1A>hBMP2[NM_001200.4]	Vector Builder	VB900131-8259aza
pLV[Exp]-mCherry/Neo-EF1A>ORF_Stuffer	Vector Builder	VB010000-9293ufr
pLV[Exp]-mCherry-EF1A>mBmp2	Vector Builder	VB900129-3383uyc
pLV[Exp]-Bsd-EF1A>mCherry	Vector Builder	VB180821-1150kqt
Software		
ImageJ	Schneider et al.[108]	https://imagej.nih.gov/ij/
Fiji	Schindelin et al.[109]	https://fiji.sc
QuPath v0.4.3	Bankhead et al.[110]	https://qupath.github.io
GraphPad Prism 9	https://www.graphpad.com/data-analysis-resource-center/#guides	https://www.graphpad.com/scientific-software/prism/
NIS Elements Advanced Research (AR) software	Nikon	N/A
Deposited Data		
Mendeley Data	Raw data for immunoblot panels	http://www.doi.org/10.17632/stdwp2tmy4.1

EXPERIMENTAL MODELS AND SUBJECT DETAIL

In vivo allograft assays

All animal experiments were approved by the Institutional Animal Care and Use Committee (IACUC) of the Johns Hopkins University (Protocol M019H421: Microenvironmental Regulation of Metastasis and Therapy Resistance) and were performed in an Association for the Assessment and Accreditation of Laboratory Animal Care (AAALAC)-accredited facility. The mice were housed in a vivarium maintained at 20 ± 2 °C, 42% humidity, with a 12-h light-dark cycle with free access to food and water. The maximum tumor size allowed under this protocol was 2000 mm^3, tumor size of 2 cm. Mice were euthanized prior reaching tumor endpoint if they showed any signs of distress. The young mice were utilized at 8 weeks, and the aged mice were >52 weeks (Charles River). Aged male mice were single housed as they were purchased as retired breeders, and young mice and aged female mice were housed in groups of no more than five per cage.

Young versus aged mice experiments

Yumm1.7, a male murine melanoma cell line and BSC9AJ2, a female murine melanoma line transduced with mCherry or Empty vector-mCherry (mEV-mCherry) or murine Bmp2 with mCherry tag (mBmp2-mCherry) where indicated were injected intradermally (2×10^5 cells) into young or aged C57Bl/6 mice (Charles River). For therapy resistance experiments, once tumors reached between 150 - 200mm^3, mice were randomized into treatment groups containing 200 mg/kg PLX4720 (BRAF inhibitor) and 7 mg/kg PD0325901 (MEK inhibitor) [BRAFi/MEKi] or control chow (Research Diets) and fed *ad libitum*.

Aged mice time course experiment

Aged (>52 weeks) male and female C57Bl/6 mice were injected intradermally (2×10^5 cells) with Yumm1.7-mCherry cells, and lungs were harvested after Day 10, Day 20 and Day 30 post-injection.

Recombinant Bmp2 treatment

Young male mice (8 weeks) were randomized into 2 groups and injected with 1 μg recombinant murine BMP2 (rmBMP2) (MedChemExpress in 50 μl PBS or the same volume of PBS (mock) every second day. Initially, rmBmp2 or PBS was injected subcutaneously around the tumor injection site for the first 7 days and then intratumor once tumors were palpable. For the rmBmp2 experiment in combination with BRAFi/MEKi therapy, young male mice (8 weeks) injected intradermally with Yumm1.7-mCherry (2×10^5 cells) cells were randomized to receive rmBmp2 or PBS as described above and further randomized to receive control chow or chow containing BRAFi/MEKi (Research Diets) once tumor volume reached between 150 - 200mm^3.

Recombinant Noggin treatment

Aged male C57Bl/6 mice (>52weeks) were injected intradermally with Yumm1.7-mCherry cells (2×10^5 cells) and randomized into 2 groups and injected with 2 μg recombinant murine Noggin (rmNoggin) (Peprotech) in 50 μl PBS or the same volume of PBS (mock) every second day. Initially, rmNoggin or PBS was injected subcutaneously around the tumor injection site for the first 7 days and then

intratumor once tumors were palpable. They were further randomized to receive control chow or chow containing BRAFi/MEKi (Research Diets) comprising four groups.

Bmp2 overexpression experiments

Yumm1.7 and BSC9AJ2 cells were transduced to express murine Bmp2-mCherry, or empty vector-mCherry (mEV-mCherry) control and sorted for mCherry expression. Melanoma cells were injected intradermally (2×10^5 cells) in young mice (8 weeks) and aged mice (>52 weeks) across both sexes. Once tumors reached between 150 - 200mm^3, mice were randomized to receive BRAFi/MEKi chow or control chow. Mice were assessed regularly, and tumors were measured routinely using digital calipers. Tumor volume was calculated using the formula 0.5 x length x (width).[2] Once tumors reached 1500mm^3 mice were euthanized, and the tumors and lungs were harvested for further analysis. All reagents injected in live mice were tested for endotoxin levels at the Johns Hopkins Cell Center Services using The Associates of Cape Cod LAL test.

Cell lines

Human melanoma cell lines FS4, FS13,[97,98] A2058 (ATCC) and murine melanoma cell line BSC9AJ2[99] were maintained in RPMI (Invitrogen), supplemented with 10% FBS and 100 U ml^{-1} penicillin and streptomycin. Lentiviral packaging cell line, HEK293T and human melanoma cell lines 1205Lu, WM983b, WM164, WM793, WM2664, and WM46 were maintained in DMEM (Invitrogen), supplemented with 10% FBS and 100 U ml^{-1} penicillin and streptomycin. Murine melanoma cell line Yumm1.7[54] was maintained in DMEM F-12 (HEPES–glutamine) supplemented with 10% FBS and 100 U ml^{-1} penicillin and streptomycin. Melanoma cell stocks were fingerprinted using an AmpFLSTR Identifier PCR Amplification Kit from Life Technologies at the Wistar Institute Genomics Facility. Human primary dermal fibroblast cell lines obtained from the biobank at the Coriell Institute for Medical Research and from healthy donors via the Baltimore Longitudinal Study of Aging[36] were maintained in DMEM, supplemented with 10% FBS and 100 U ml^{-1} penicillin and streptomycin. Atleast 3 biological replicates were used per age group and sex unless indicated. All cell lines were cultured at 37 °C in 5% CO_2, and the medium was replaced as required. Cell culture supernatants were tested routinely for mycoplasma contamination using a Lonza MycoAlert assay at the Johns Hopkins University Cell Center Services.

METHOD DETAILS

Treatments

To assess proliferation, senescence and signaling attributes, dermal fibroblasts were maintained in phenol-red free DMEM supplemented with 10% charcoal/dextran (Millipore Sigma) stripped FBS and 100 U ml^{-1} penicillin and streptomycin. Serum depletion of estrogen was performed based on the manufacturer's guidelines. Melanoma cells were treated with doxycycline hyclate (DOX) (TCI America) at a final concentration of 1 μg/mL for 48 hours. Conditioned media (CM) derived from fibroblast cells after 72 hours of incubation was spun at 4000 rpm, filtered through a 0.45 μm low protein binding PVDF filter, and frozen in aliquots. Prior to use, CM was normalized to fibroblast cell count before using on melanoma cells. For short-term signaling experiments, melanoma cells were treated with recombinant human/mouse BMP2 (R&D Systems, MedChemExpress) at indicated concentrations for 30 minutes or with 100 ng/ml for indicated time points. For long-term experiments, melanoma cells were treated with rBMP2 at 100 ng/ml for 16, 24 and 48 hours. Melanoma cells treated with recombinant human NOGGIN (rhNOGGIN) (R&D Systems) at 0.5 μg/ml or rBMP2 (100 ng/ml) or combination for 30 minutes. Long-term rhNOGGIN treatment experiment on melanoma cells was performed by co-treating aged male fibroblast CM or mock with rhNOGGIN at 1 μg/ml for 48 hours. Fibroblast treatment with EZH2 inhibitor, GSK126 at 5 μM (Selleck Chem) and ATM kinase inhibitor, KU-60019 (Selleck Chem) at 3 μM was performed in normal growth media at indicated timepoints. For any treatment longer than 48 hours, media with the inhibitors/drugs was replenished every 48 hours.

BrdU Incorporation Assay

Dermal fibroblasts were grown on coverslips at similar seeding densities for 2 days. Asynchronously growing fibroblast cells were given a 16 or 24 hours pulse of 20 μM BrdU (5-Bromo-2'-deoxyuridine, Peprotech) to determine cells in S phase as previously described.[100] For assessing CM effects, melanoma cells were plated on coverslips and subjected to fibroblast-derived CM (normalized by cell counts) for 48 hours and given a pulse of 20 μM BrdU an hour before fixation. Dermal fibroblasts and melanoma cells, where indicated, were treated with rBMP2 (100 ng/ml) or rhNOGGIN (500 ng/ml) for 48 hours and 20 μM BrdU was added 16 hours and 1 hour, respectively prior to fixation. Cells were fixed in cold 70% ethanol and stained with anti-BrdU antibody (Cell Signaling) as per manufacturer's guidelines and counterstained with DAPI (Thermo Scientific). Random fields of view were taken by first imaging for DAPI and then for BrdU for the same field of view on Nikon Eclipse Ti2 microscope. Quantification was done blind and data was represented as a percentage of BrdU-positive nuclei.

Senescence associated β-Galactosidase staining

Fibroblasts were plated into 12-well dishes at similar seeding densities and incubated for 48 hours. Subsequently, washed with PBS and fixed in 2% formaldehyde/0.2% glutaraldehyde prior to staining as described previously.[101] Cells were then incubated in staining solution containing 150 mM NaCl (Sigma), 2 mM $MgCl_2$ (Sigma), 5 mM $K_3Fe(CN)_6$ (Millipore), 5 mM $K_4Fe(CN)_6$ (Millipore), 40 mM Na_2PO_4 (Sigma) pH 6.0, 20 mg/ml X-Gal (Selleck Chem) at 37°C overnight in CO_2-free incubator. Stain was removed, and cells

were stored in 70% glycerol before imaging on Nikon Eclipse Ti2 microscope. Senescent cells were counted and represented as percentage β-Galactosidase positive cells.

ROS Detection Assay

Five thousand fibroblast cells were seeded in a 96-well plate with 8 wells per fibroblast line and incubated overnight. The cells were subjected to 2 mM hydrogen peroxide (Sigma) or PBS treatment in serum-free media for 30 minutes. After 30 minutes, media was replaced with growth media and cells were incubated for 24 hours. ROS levels were measured at 0 hours (mock), 0.5 hours (immediately after H_2O_2 treatment) and 24 hours after initial treatment using a Cell Meter Fluorimetric Intracellular Total ROS Kit (AAT Bioquest) according to the manufacturer's protocol. The plates were measured using a PerkinElmer EnVision Xcite Multilabel plate reader using the filters for excitation/emission (Ex/Em = 520/605 nm). The cell number was determined by DAPI (Thermo Scientific) and used to normalize the total fluorescence obtained from ROS staining.

Immunoblotting Analysis

Cells lysed in RIPA buffer supplemented with protease and phosphatase inhibitors (Cell Signaling). Total protein lysate was quantified using a Pierce BCA assay kit (Fisher Scientific), and 20 μg of protein for dermal fibroblasts or 30 μg of melanoma lysates was prepared in sample buffer, heated at 95°C and loaded into NuPAGE 4–12% or 12% Bis-Tris Protein Gels (Thermo Scientific) and run at 160 V. Proteins were then transferred onto a PVDF membrane using the iBlot system (Invitrogen) and blocked in 5% BSA–TBST for 1 hour. Primary antibodies were diluted in 5% BSA–TBST and incubated at 4°C overnight. The membranes were washed in TBST and probed with the corresponding HRP-conjugated secondary antibody (Cell Signaling). Proteins were visualized using ECL (GE Healthcare) and detected using G:BOX Chemi XRQ gel doc system (Syngene).

Immunohistochemistry

Human sections from stage I/II melanoma from age-matched male and female patients (>55 years), mouse tumor and lung tissue sections were paraffin-embedded and sectioned at 4 μm. Tissue sections were rehydrated through a series of xylene and different concentrations of alcohol, which was followed by a rinse in water and washing in PBS. Slides were incubated with antigen unmasking solution (Vector Labs) and steamed for 20 min. Slides were then blocked in a peroxide blocking buffer (Abcam) for 15 min, followed by protein block (Abcam) for 5 minutes, and incubated with the primary antibody of interest, which was prepared in antibody diluent (Dako). Slides were incubated overnight in a humidified chamber at 4 °C. Samples were washed with PBS and incubated in biotinylated anti-rabbit secondary antibody (Abcam), followed by streptavidin–HRP solution (Abcam) at room temperature for 20 min. Samples were then washed with PBS and incubated with AEC substrate (3-amino-9-ethylcarbazole, Abcam) for the appropriate amount of time after optimization. Slides were then washed with water and incubated in Mayer's hematoxylin (Abcam) for 1 min, rinsed with water, and mounted in Aquamount (Vector Labs). Slides were imaged using a Nikon Eclipse Ti2 microscope. Quantification of IHC staining was performed to determine nuclear positivity or H-Score using ImageJ or QuPath v0.4.3 using the positive cell detection feature and user defined threshold presets. Murine lungs were assessed for localization of mCherry-positive melanoma cells per high-power field (HPF) and quantified.

3-D Spheroid Assays

Melanoma cells (5000 cells/well) were plated in 1.5% agar, and spheroids were allowed to form for 3 days in a 96-well plate. Spheroids were embedded in rat-tail collagen I (Thermo Scientific) and subjected to recombinant protein treatment (rBMP2, rhNOGGIN) or CM (normalized by total cell count) from age and sex-stratified dermal fibroblasts. All spheroids were imaged at Day 0 and 24 hours post-embedding for 1205Lu, 48 hours post-embedding for WM164, WM793 and WM2664 and 72 hours post-embedding for WM983b melanoma cell lines. The spheroids were imaged using a Nikon Eclipse Ti2 inverted microscope. Quantitation of invasive surface area was performed using NIS Elements Advanced Research software and represented as percent invasion relative to 0 hours.

For therapy resistance analysis, embedded spheroids were subjected to CM or treatment with rBMP2 (100 ng/ml) and/or rhNOGGIN (500 ng/ml) in the presence or absence of BRAFi (PLX4720 (3 μM)) and MEKi (PD0325901 (500 nM)) inhibitors. Cell viability was measured using the Live/Dead viability/cytotoxicity kit (Fisher Scientific). Briefly, spheroids were washed with PBS and stained with calcein-AM (2 μM) and ethidium homodimer-1 (4 μM). The dyes were diluted in PBS, and 300 μL of the solution was added to the spheroid wells for 30 minutes at 37°C. The spheroids were washed in PBS and imaged using a Nikon Eclipse Ti2 inverted microscope. Quantitation of cell death (total intensity of ethidium homodimer-1) relative to spheroid area (calcein-AM) was performed using NIS Elements AR software and represented as relative cell death compared to DMSO treatment.

Lentiviral transduction

Lentiviral production was carried out as described in the protocol developed by the TRC library (Broad Institute). Briefly, HEK293T cells were co-transfected with shRNA vector or expression plasmids and third-generation lentiviral packaging plasmids (pMDLg/pRRE, pRSV-Rev, pMD2.G). Media was changed the following day, and the supernatant containing the virus was harvested at 48 hours and filtered through a 0.45 μm low protein binding PVDF filter. The cells were allowed to recover for 48 hours and then selected using puromycin or flow-sorted on MoFlo XDP (Beckton Coulter) for the selection marker (mCherry).

Quantitative real-time PCR and telomere length determination

RNA was extracted using RNeasy Mini kit (Qiagen), and cDNA was prepared using iScript cDNA synthesis kit (Bio-Rad). Gene expression was quantified using Fast SYBR green master mix (Applied Biosystems) method of qPCR on an ABI Viia7 real-time PCR system (Applied Biosystems) using fast conditions. Samples were normalized against the human *18s* housekeeping gene and normalized as relative expression. Primer sequences are listed in Table S3. DNA was extracted using DNeasy blood and tissue kit (Qiagen) and average telomere length was calculated using Relative Human Telomere Length Quantification qPCR Assay Kit (ScienCell) as per manufacturer's guidelines.

Immunofluorescence and Quantification

Cells were seeded on sterile glass coverslips in 12-well plates at 1×10^4 (melanoma cells) or 4×10^4 cells (fibroblasts) per well and incubated for indicated times. After the treatment, cells were fixed with 4% paraformaldehyde (PFA) (Electron Microscopy Sciences) diluted in PBS for 20 minutes at room temperature. Cells were permeabilized with PBS containing 0.25% Triton X (Sigma) for 10 minutes and washed with PBS prior to blocking in 2% BSA (Millipore Sigma) in PBS containing 0.1% Triton X for 1 hour. Primary antibodies were diluted per manufacturer's guidelines in blocking buffer and incubated overnight at 4 °C in a humidified chamber. Cells were washed in PBS and incubated with the appropriate Alexa Fluor conjugated secondary antibody (1:400, Thermo Scientific) for 1 hour at room temperature. Cells were then washed in PBS, counterstained with DAPI (Thermo Scientific) and mounted in Prolong Glass antifade mountant (Thermo Scientific). Images were captured on a Nikon Eclipse Ti2 microscope and quantified using ImageJ (NIH).

Cytosolic and mitochondrial ROS measurement

Cells were seeded in 12-well plates at 1×10^4 (melanoma cells) or 4×10^4 cells (fibroblasts) per well and subjected to treatment for 48 hours as indicated. Cells were washed with HBSS and incubated for 1 hour in growth media containing 5 μM CellROX Green for cytosolic ROS or for 10 minutes in HBSS containing 5 μM MitoSOX Red for mitochondrial ROS. Following dye removal, cells were washed three times in HBSS and imaged in HBSS on Nikon Eclipse Ti2 microscope. Cell images were analyzed with Fiji, the open-source processing program distribution of ImageJ (NIH) by measuring cell area and mean fluorescence intensity, along with the adjacent background. This was used to calculate the corrected total cell fluorescence (CTCF) using the formula CTCF = integrated density – (area of selected cell × mean fluorescence of background readings), as described previously.[102]

Proteomics

Fibroblasts were plated at an equal number and grown to 80% confluency in a 10-cm dish. They were washed once with PBS and five times with serum-free DMEM medium and grown for 16 hours in 10 ml serum-free DMEM medium. Conditioned medium was collected, centrifuged at a low speed to remove cells and debris, and filtered through a 0.45 μm low protein binding PVDF filter (Millipore Sigma). Protease inhibitors (PMSF, pepstatin A and leupeptin) were added and flash-frozen at −80 °C until ready. Fibroblasts from the 10-cm dish were disassociated and the number of cells were counted using a hemocytometer, and the protein concentration was determined using the Pierce BCA assay (Thermo Scientific). Conditioned medium was then concentrated using a 3K MWCO ultrafiltration concentrator (Millipore). Concentrated CM was quantified following silver staining on SDS gel, and proportional volumes were run into a short preparative SDS gel. The entire stained gel lanes were excised, digested with trypsin, labeled with TMT10plex reagents, mixed, and subjected to high-pH peptide fractionation. Fractions were analyzed by liquid chromatography-tandem mass spectrometry using a Q Exactive HF-X mass spectrometer (Thermo Scientific). Database was searched using MaxQuant v.1.6.0.16,[103] protein intensity levels were $\log_2$-transformed and undetected intensities were floored to a minimum detected intensity across all proteins and samples. An unpaired Student's two-sided t-test was used to estimate the significance of the difference between groups, and the false discovery rate was estimated.[104] Proteins that passed the criterion of a false discovery rate of less than 5% were considered significant, and the top changed proteins with nominal $P < 0.05$ were reported on a scatter plot and significantly altered proteins are indicated in Table S1.

Chemokine array

Conditioned medium from aged male and female fibroblasts (2 lines per cohort) were collected after 72 hours in normal growth medium and filtered through a 0.45 μm low protein binding PVDF filter. Harvested CM was normalized to the fibroblast cell count and incubated with membranes provided in the Proteome Profiler Human XL Cytokine Array kit (R&D Systems) according to the manufacturer's instructions. Membranes were imaged using G:BOX Chemi XRQ gel doc system (Syngene) and analyzed using ImageJ (NIH). Relative cytokine intensities were normalized in comparison to reference spots on the same membrane. Expression ratios between aged male and female CM membranes were calculated by comparing the signal intensities for each spot of the different cytokines and plotted on the heat map.

BMP2 neutralization assay

Equal number of aged dermal fibroblasts ($1x10^5$ cells per well) were plated in duplicates in a 6 well dish. Following day, fibroblasts were subjected to 15 μg/ml of BMP2 neutralization antibody (Thermo Scientific) or isotype control (R&D Systems) for 48 hours. Conditioned medium was collected and filtered through a 0.45 μm low protein binding PVDF filter and assessed for BMP2 neutralization.

BMP2 ELISA and Total Antioxidants assay

Conditioned medium from fibroblasts (3 - 4 lines per cohort) was collected after 72 hours in normal growth medium and filtered through a 0.45 μm low protein binding PVDF filter. Harvested CM was normalized to the fibroblast cell count and assessed for BMP2 using ELISA (R&D Systems) and total antioxidants (Sigma Aldrich) as per manufacturer's guidelines. Human serum from healthy male and female subjects (>55 years) and age-matched male melanoma patients was analyzed for BMP2 (Abcam) as per manufacturer's guidelines.

Generation of BRAFi-resistant cell lines

To generate BRAFi (PLX4720) resistant melanoma cell lines, BRAFi-sensitive cell lines were seeded at low density and exposed to 1–5μM PLX4720 (SelleckChem). After approximately eight weeks of continuous BRAFi exposure, we derived 'resistant' cell clones that were maintained on BRAFi (1μM for WM983b; 1 μM for WM164; 3μM for 1205Lu; 5 μM for Yumm1.7).

TCGA and cBioportal analysis

RNA-seq data from skin cutaneous melanoma (SKCM) was downloaded from the TCGA database using cBioportal (http://www.cbioportal.org). Individual gene expression values for genes of interest were retrieved as normalized RNA-seq by expectation maximization (RSEM) read counts processed through the TCGA cBioportal. The data were then transformed to represent a standardized z-score for each gene and further transformed such that the gene of interest (WNT5A) was separated into two groups based on the top 25 percentile and bottom 25 percentile of gene expression within the samples from patients with melanoma ($n = \sim 120$). A Student's two-sided t-test (unpaired) was then performed on each gene in the dataset to individually analyze the difference in average z-score in low- versus high-percentile melanoma samples. Data are presented as a heat map based on high (red, 0.5) and low (blue, −0.5) z-scores and associated P values. Significance was taken at $P < 0.05$.

QUANTIFICATION AND STATISTICAL ANALYSIS

For *in vitro* studies, images and immunoblots were organized and analyzed using ImageJ, QuPath v0.4.3 and Microsoft Excel. For *in vivo* studies, the indicated sample size for each experiment was designed to have 80% power at a two-sided α of 0.05 to detect a difference of large effect size of about 1.25 between two groups on a continuous measurement. A linear mixed effect model followed by chi-square test was used for tumor growth comparison with recombinant protein and BRAFi/MEKi therapy.

For analysis of mBmp2-mCherry and mEV-mCherry tumor growth experiment with BRAFi/MEKi therapy, the statistical analysis was aimed at capturing the differences between respective means of two unpaired groups, labeled A (mEV-mCherry on control chow), B (mEV-mCherry on BRAFi/MEKi chow), C (mBMP2-mCherry on control chow), D (mBMP2-mCherry on BRAFi/MEKi chow), (mean(A) – mean(B) versus mean(C) – mean(D)). The focus is to capture the temporal dynamics of tumor volume progression, aimed at predicting the days required to achieve the average tumor volumes across these groups within the same cohort.

A curve-fitting method was applied to model the relationship between the days (as the response variable) and tumor volumes (as the explanatory variable) of mice that survived until the endpoint of the study for each group. The fitting process utilized the monotone Hermite spline method,[105] applying on the latter monotonic segments of tumor volume progression and corresponding time points. We set our null hypothesis as follows. With all the other conditions fixed, the difference of days between mEV-mCherry on BRAFi/MEKi Chow and mEV-mCherry control chow is no larger than the difference in days between mBMP2-mCherry BRAFi/MEKi Chow and mBMP2-mCherry control chow. To test this hypothesis, we implemented a bootstrap method,[106] accounting for the potential non-normality of day distributions. This involved three steps:

1. Bootstrapping groups C and D independently to estimate their mean differences.
2. Adjusting group B by adding the bootstrapped mean difference between C and D to each of B's elements, thus transforming the hypothesis testing framework to compare two groups with equal means.
3. Pooling groups A and the adjusted B for bootstrapping, followed by *p*-value computation to assess statistical significance.

All statistical analysis was performed with the Prism 9.0 software (GraphPad Software, San Diego, CA, USA) using unpaired Student's t-test, one-way or two-way ANOVA followed by Tukey's test and Dunnett's test, respectively. The p-values ≤ 0.05 were considered significant. Data are represented as mean ± SEM or before-after (paired Student's t-test) as indicated. Significance was designated as follows: *$P < 0.05$; **$P < 0.01$; ***$P < 0.001$.

Supplemental figures

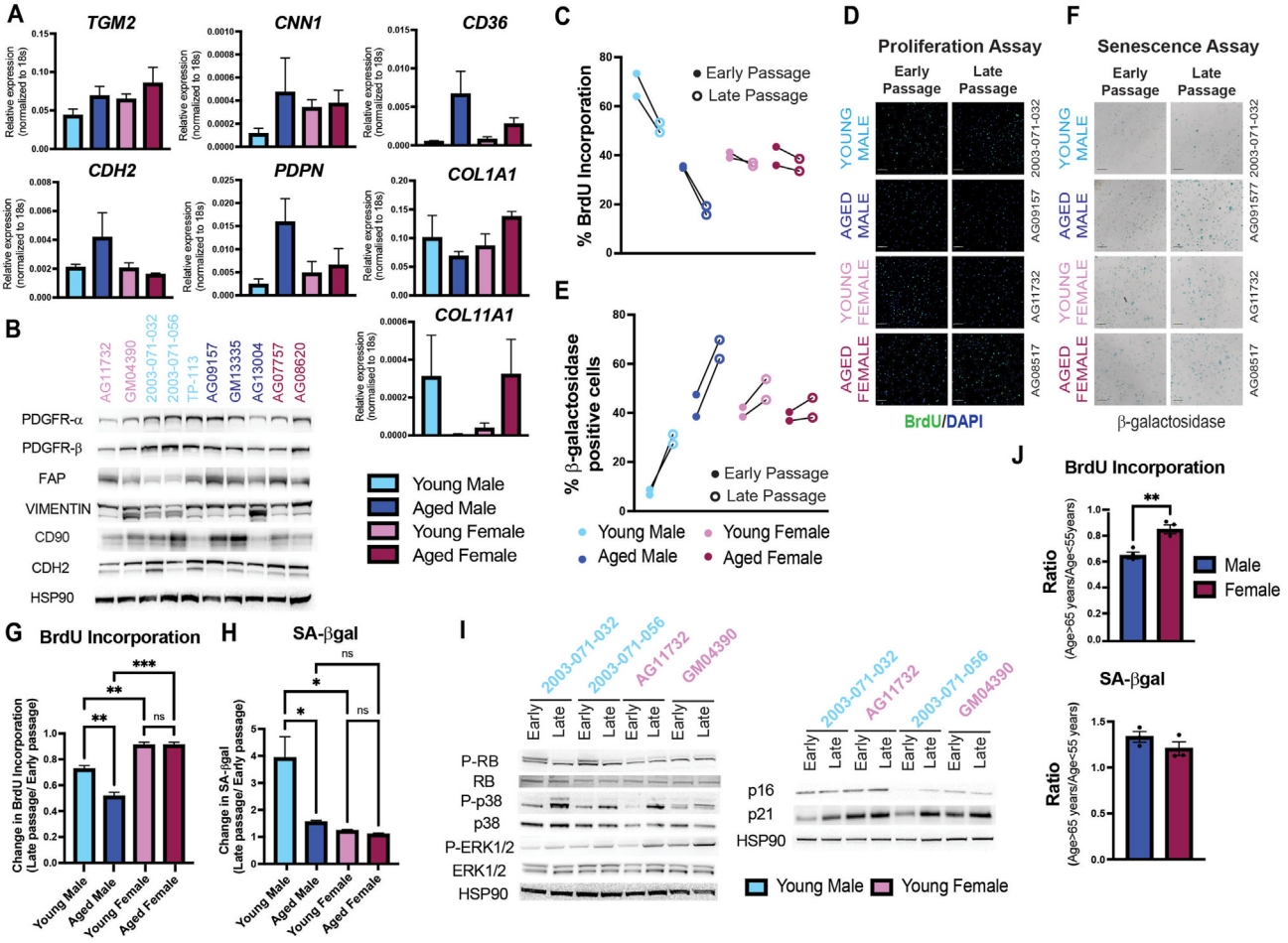

Figure S1. Age-associated replicative senescence in primary dermal fibroblasts is sex-dependent, related to Figure 1

(A) Relative gene expression (RT-qPCR) of markers associated with reticular (*TGM2*, *CNN1*, *CD36*, *COL11A1*, *CDH2*, and *COL1A1*) and papillary (*PDPN*) dermis in age- and sex-stratified fibroblasts, normalized to *18s* ($n = 3$).

(B) Immunoblot analysis of proteins associated with cancer-associated fibroblast (CAF) markers in age- and sex-stratified fibroblasts. HSP90 was used as loading control.

(C) Quantification of BrdU-positive nuclei in age- and sex-stratified fibroblasts during early vs. late passage (10 serial passages from early passage) represented as paired analysis (before and after) ($n = 2$).

(D) Representative images of BrdU assay from (C). Scale bars show 100 μm.

(E) Quantification of SA-βgal cells in age- and sex-stratified fibroblasts during early vs. late passage (after 10 serial passages) represented as paired analysis (before and after) ($n = 2$).

(F) Representative images of SA-βgal assay from (E). Scale bars show 100 μm.

(G) Quantification of BrdU data in (C) as ratio of late passage vs. early passage (***$p < 0.001$, **$p < 0.01$, $n = 2$).

(H) Quantification of SA-βgal in (E) as ratio of late passage vs. early passage (*$p < 0.05$, $n = 2$).

(I) Immunoblot analysis of senescence phenotype-associated markers in sex-stratified young fibroblasts during early vs. late passage fibroblasts. HSP90 was used as loading control.

(J) Quantification of BrdU incorporation and SA-βgal represented as ratio >65 and <55 years in genetically identical fibroblasts from the same donor stratified by sex (**$p < 0.01$, $n = 2$).

Values are presented as mean ± SEM.

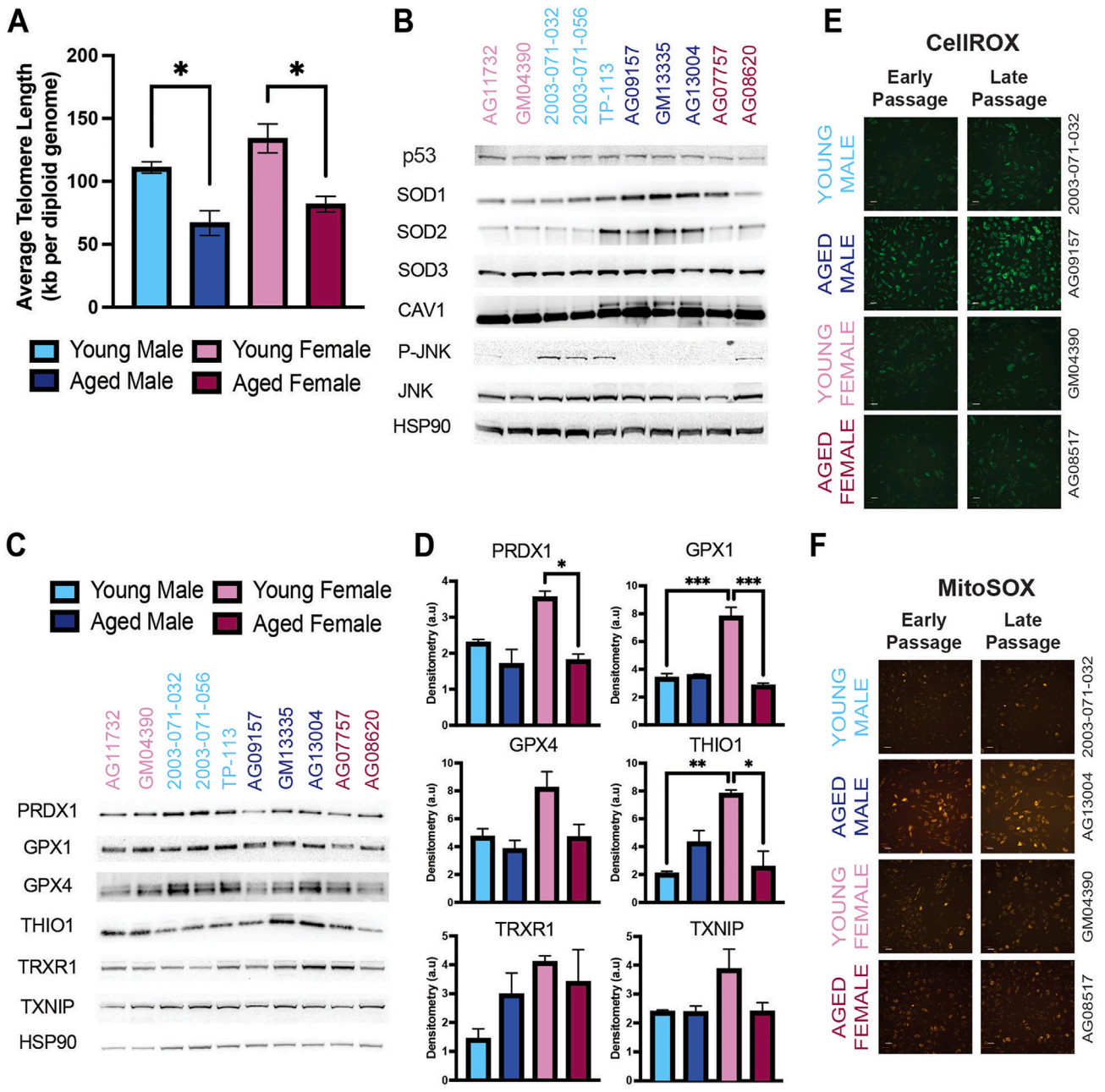

Figure S2. Elevated oxidative stress in aged male dermal fibroblasts promotes acquisition of an SASP, related to Figure 2

(A) Average telomerase length in age- and sex-stratified fibroblasts (*$p < 0.05$, $n = 3$).

(B) Immunoblot for stress response proteins in age- and sex-stratified fibroblasts. HSP90 was used as loading control.

(C) Immunoblot for redox proteins in age- and sex-stratified fibroblasts. HSP90 was used as loading control.

(D) Densitometry (arbitrary units [a.u.]) of immunoblots from (C) relative to HSP90 (***$p < 0.001$, **$p < 0.01$, *$p < 0.05$).

(E) Representative images of CellROX-green in early vs. late passage (10 serial passages from early passage) fibroblasts stratified by age and sex ($n = 2$). Scale bars show 100 μm.

(F) Representative images of MitoSOX-red in early vs. late passage fibroblasts stratified by age and sex, measured as corrected total cell fluorescence ($n = 2$). Scale bars show 100 μm.

Values are presented as mean ± SEM.

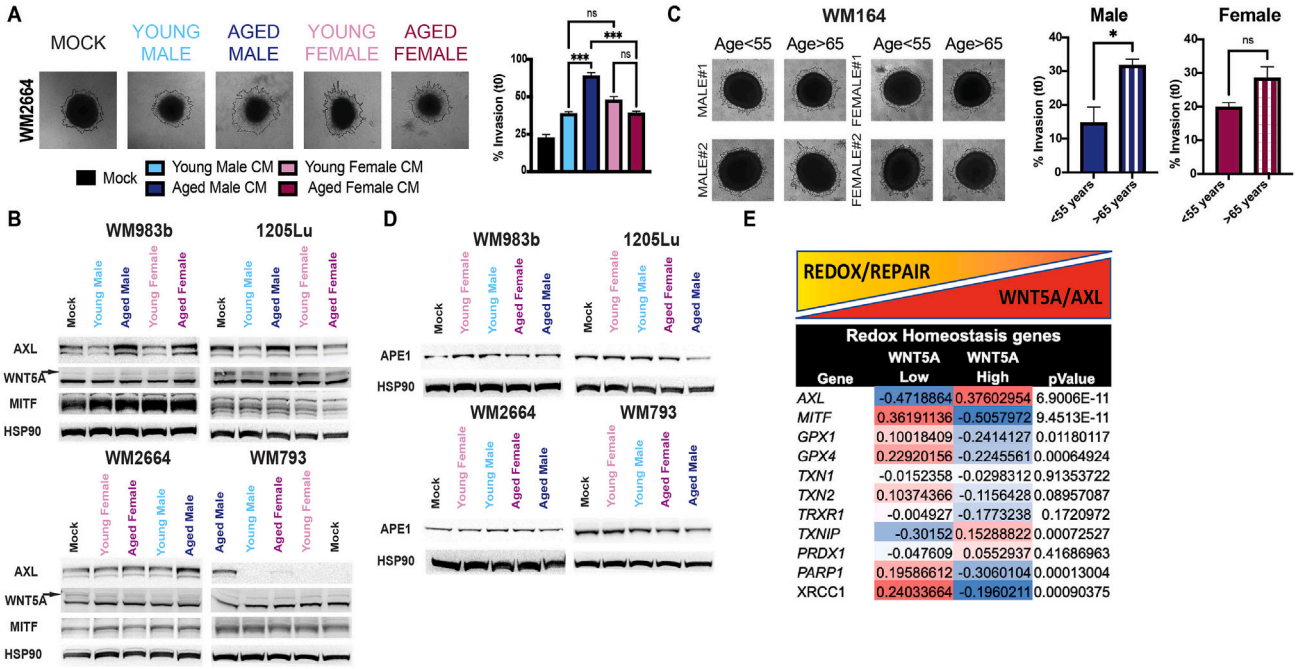

Redox Homeostasis genes

Gene	WNT5A Low	WNT5A High	pValue
AXL	-0.4718864	0.37602954	6.9006E-11
MITF	0.36191136	-0.5057972	9.4513E-11
GPX1	0.10018409	-0.2414127	0.01180117
GPX4	0.22920156	-0.2245561	0.00064924
TXN1	-0.0152358	-0.0298312	0.91353722
TXN2	0.10374366	-0.1156428	0.08957087
TRXR1	-0.004927	-0.1773238	0.1720972
TXNIP	-0.30152	0.15288822	0.00072527
PRDX1	-0.047609	0.0552937	0.41686963
PARP1	0.19586612	-0.3060104	0.00013004
XRCC1	0.24033664	-0.1960211	0.00090375

Figure S3. Aged male fibroblasts promote maximal invasion and oxidative stress in melanoma cells, related to Figure 3

(A) Representative images of spheroid assay on WM2664 melanoma cells subjected to conditioned media from age- and sex-stratified fibroblasts for 48 h. Invaded area is outlined in black. Quantified as percent invasion relative to 0 h (***$p < 0.001$, $n = 3$). Scale bars show 100 μm.

(B) Immunoblot of phenotype switch signature (AXL, MITF, WNT5A [indicated by black arrow]) in melanoma cells subjected to conditioned media from age- and sex-stratified fibroblasts for 48 h. HSP90 was used as loading control ($n = 2$).

(C) Representative images of spheroid assay on WM164 melanoma cells subjected to conditioned media from genetically identical fibroblasts from the same donor (<55 and >65 years) stratified by sex for 48 h. Invaded area is outlined in black. Quantified as percent invasion relative to 0 h (**$p < 0.01$, $n = 3$). Scale bars show 100 μm.

(D) Immunoblot of APE1 in melanoma cells subjected to conditioned media from age- and sex-stratified fibroblasts for 48 h. HSP90 was used as loading control ($n = 2$). APE1 was probed on the same blot as (B) for WM983b, 1205Lu, and WM793.

(E) Analysis of the skin cutaneous melanoma (SKCM) TCGA dataset (all samples) for redox genes on tumor samples stratified into the top ($WNT5A^{high}$) and bottom ($WNT5A^{low}$) 25^{th} percentile of WNT5A expression and presented as a heatmap of the average *Z* score. An unpaired two-sided t test was performed to estimate the significance of the difference between conditions; $p < 0.05$ was considered significant ($n = 120$ per group).

Values are presented as mean ± SEM.

See also Data S1.

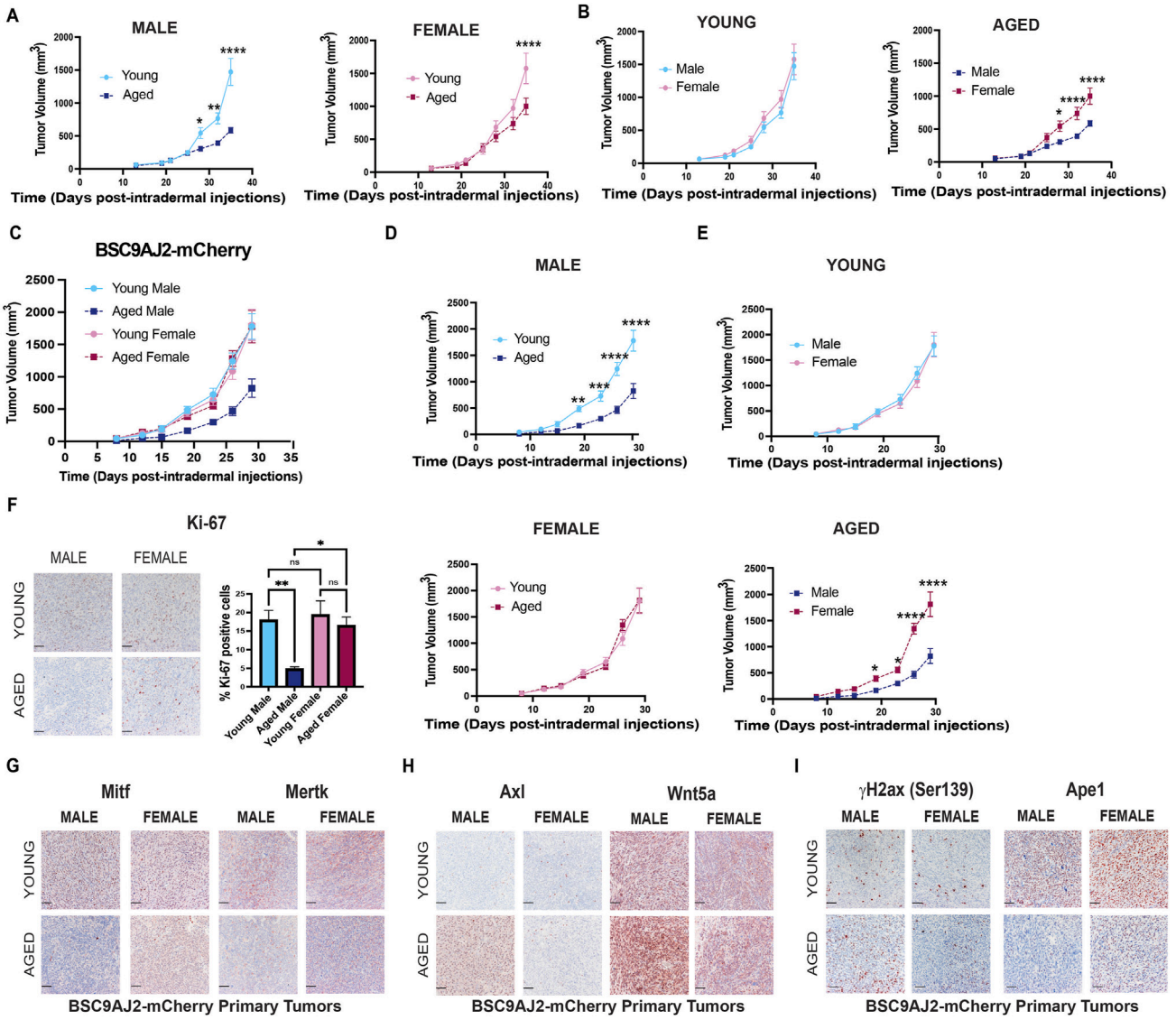

Figure S4. Age and sex of the host microenvironment regulate melanoma growth *in vivo*, related to Figure 4

(A) Tumor growth measurement stratified by sex for Yumm1.7-mCherry injected intradermally in immunocompetent C57BL/6 mice young (8 weeks) and aged (>52 weeks) across both sexes (****$p < 0.0001$, **$p < 0.01$, *$p < 0.05$, n = 7–8 mice per group).

(B) Tumor growth measurement stratified by age for Yumm1.7-mCherry injected intradermally in immunocompetent C57BL/6 mice young (8 weeks) and aged (>52 weeks) across both sexes (****$p < 0.0001$, *$p < 0.05$, n = 7–8 mice per group).

(C) Tumor growth measurement of female murine BSC9AJ2-mCherry injected intradermally in immunocompetent C57BL/6 mice young (8 weeks) and aged (>52 weeks) across both sexes (n = 8–10 mice per group).

(D) Tumor growth measurement stratified by sex for BSC9AJ2-mCherry injected intradermally in immunocompetent C57BL/6 mice young (8 weeks) and aged (>52 weeks) across both sexes (****$p < 0.0001$, ***$p < 0.001$, **$p < 0.01$, n = 8–10 mice per group).

(E) Tumor growth measurement stratified by age for BSC9AJ2-mCherry injected intradermally in immunocompetent C57BL/6 mice young (8 weeks) and aged (>52 weeks) across both sexes (****$p < 0.0001$, *$p < 0.05$, n = 8–10 mice per group).

(F) Histological examination of Ki-67 (brown) in BSC9AJ2-mCherry primary tumors and quantified as percentage Ki-67 positive nuclei (**$p < 0.01$, n = 5 tumors per group). Scale bars show 50 μm.

(G) Representative images of BSC9AJ2-mCherry primary tumors stained for Mitf and Mertk expression (n = 4 tumors per group). Scale bars show 50 μm.

(H) Representative images of BSC9AJ2-mCherry primary tumors stained for Axl and Wnt5a expression (n = 4 tumors per group). Scale bars show 50 μm.

(I) Representative images of BSC9AJ2-mCherry primary tumors stained for γH2ax (Ser139) and Ape1 expression (n = 4 tumors per group). Scale bars show 50 μm.

Values are presented as mean ± SEM.

See also Data S1.

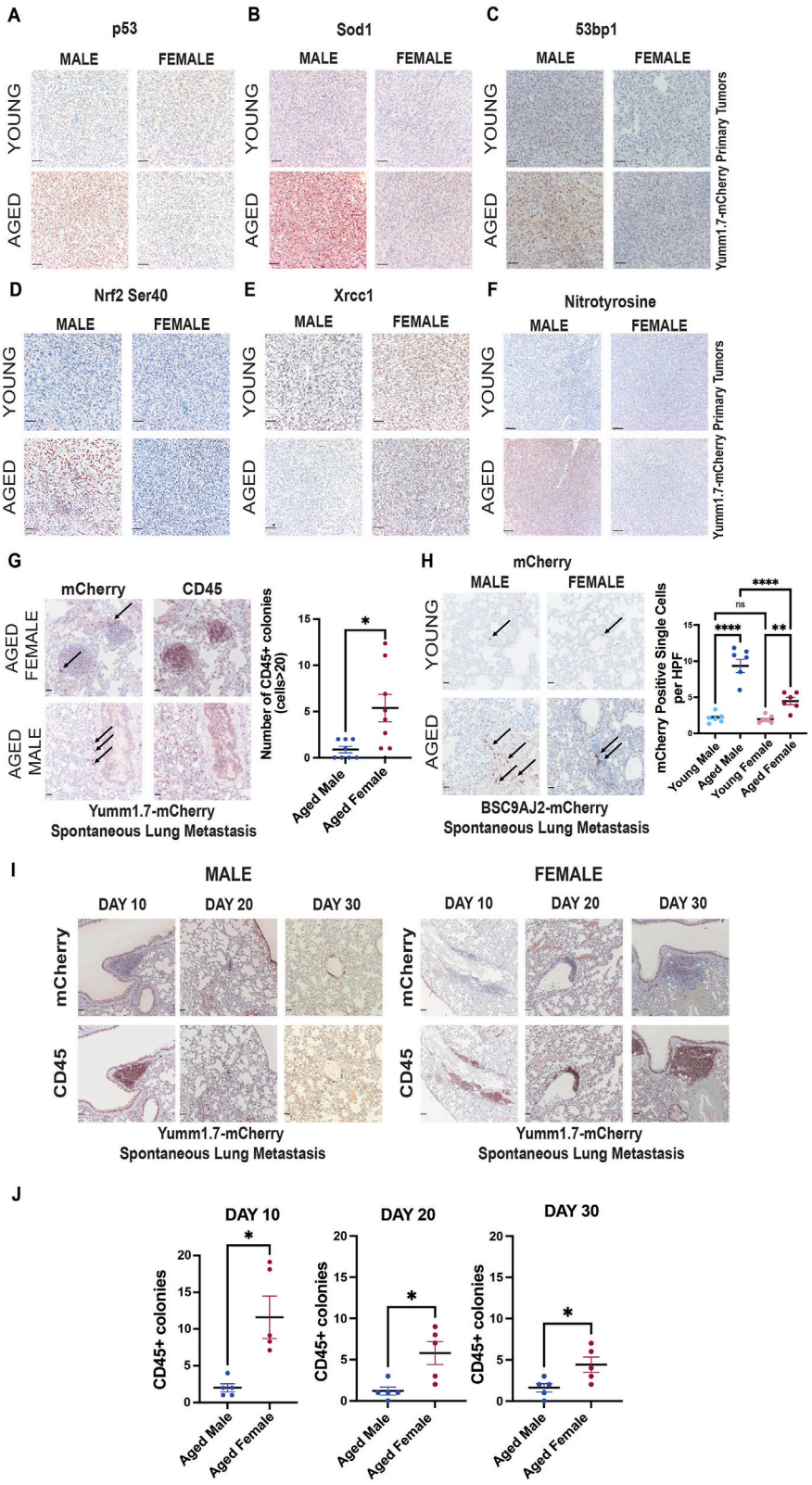

(legend on next page)

Figure S5. Age and sex of the host microenvironment regulate melanoma metastasis *in vivo*, related to Figure 4

(A) Representative images of Yumm1.7-mCherry primary tumors stained for p53 expression (n = 4 tumors per group). Scale bars show 50 μm.
(B) Representative images of Yumm1.7-mCherry primary tumors stained for Sod1 expression (n = 4 tumors per group). Scale bars show 50 μm.
(C) Representative images of Yumm1.7-mCherry primary tumors stained for 53bp1 expression (n = 4 tumors per group). Scale bars show 50 μm.
(D) Representative images of Yumm1.7-mCherry primary tumors stained for Nrf2 (Ser40) expression (n = 4 tumors per group). Scale bars show 50 μm.
(E) Representative images of Yumm1.7-mCherry primary tumors stained for Xrcc1 expression (n = 4 tumors per group). Scale bars show 50 μm.
(F) Representative images of Yumm1.7-mCherry primary tumors stained for nitrotyrosine expression (n = 4 tumors per group). Scale bars show 50 μm.
(G) Representative images of mCherry and CD45 stained lungs in aged (>52 weeks) male and female C57BL/6 mice at 5 weeks post-intradermal injection of Yumm1.7-mCherry cells. Black arrow indicates mCherry-positive cells. Scale bars show 50 μm. Quantification of CD45 stained colonies (with >20 cells/colony) ($^*p < 0.05$, n = 8 mice per group).
(H) Representative images of lung metastasis stained with mCherry at 5 weeks post-intradermal injection of BSC9AJ2-mCherry cells in young (8 weeks) and aged (>52 weeks) C57BL/6 mice across both sexes. Black arrow indicates mCherry-positive cells. Scale bars show 50 μm. Quantification of melanoma pulmonary metastasis as single mCherry-positive cells per high-power field (HPF) ($^{****}p < 0.0001$, $^{**}p < 0.01$, n = 6 mice per group).
(I) Representative images of mCherry and CD45 stained lungs in aged (>52 weeks) male and female C57BL/6 mice at days 10, 20, and 30 post-intradermal injections of Yumm1.7-mCherry cells. Scale bars show 50 μm.
(J) Quantification of CD45 stained colonies (with >20 cells/colony) from (Q) ($^*p < 0.05$, n = 5 mice per group).
Values are presented as mean ± SEM.
See also Data S1.

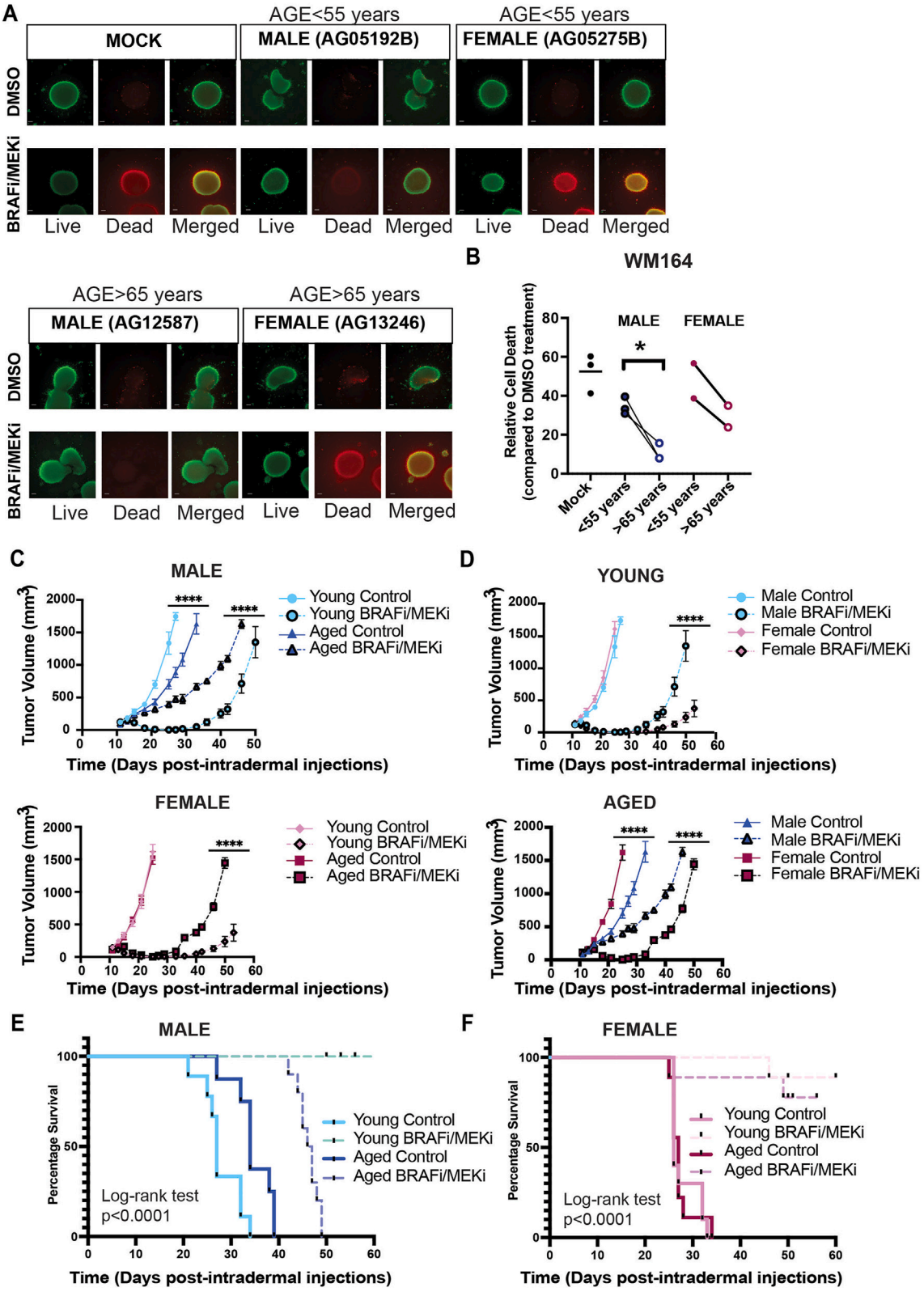

(legend on next page)

Figure S6. Age and sex of the host microenvironment regulate therapy response and resistance, related to Figure 5

(A) Viability assay on WM164 melanoma spheroids treated with conditioned media from age- and sex-stratified genetically identical fibroblast lines in the presence of 3 μM PLX4720 (BRAFi) and 500 nM PD0325901 (MEKi) or DMSO (mock) for 48 h. Viability was assessed by staining with calcein-AM (green) and ethidium homodimer-1 (red/orange), indicating live and dead cells, respectively. Scale bars show 100 μm.

(B) Quantification of cell death (total intensity of ethidium homodimer-1) relative to spheroid area (calcein-AM) following BRAFi/MEKi treatment is represented as relative cell death compared with DMSO treatment with paired analysis (*$p < 0.05$, $n = 2$ for females and $n = 3$ for males).

(C) Tumor growth measurement stratified by sex for Yumm1.7-mCherry injected intradermally in immunocompetent C57BL/6 mice young (8 weeks) and aged (>52 weeks) across both sexes. Mice were randomized to receive diet containing control chow (control) or BRAFi/MEKi chow (200 mg/kg PLX4720 and 7 mg/kg PD0325901) *ad libitum* (****$p < 0.0001$, $n = 7$ mice per control chow group and $n = 8$ mice per BRAFi/MEKi chow group).

(D) Tumor growth measurement stratified by age as above across both sexes. Mice were randomized to receive diet containing control chow (control) or BRAFi/MEKi chow (200 mg/kg PLX4720 and 7 mg/kg PD0325901) *ad libitum* (****$p < 0.0001$, $n = 7$ mice per control chow group and $n = 8$ mice per BRAFi/MEKi chow group).

(E) Kaplan-Meier survival curves for male mice treated in (C), indicating the time taken for the tumor to reach a defined size of tumor volume 1,500 mm^3 or death with a day 50 cutoff, by which all aged male mice were euthanized.

(F) Kaplan-Meier survival curves for female mice treated in (C), indicating the time taken for the tumor to reach a defined size of tumor volume 1,500 mm^3 or death with a day 50 cutoff, by which all aged male mice were euthanized based on tumor volume.

Values are presented as mean ± SEM.

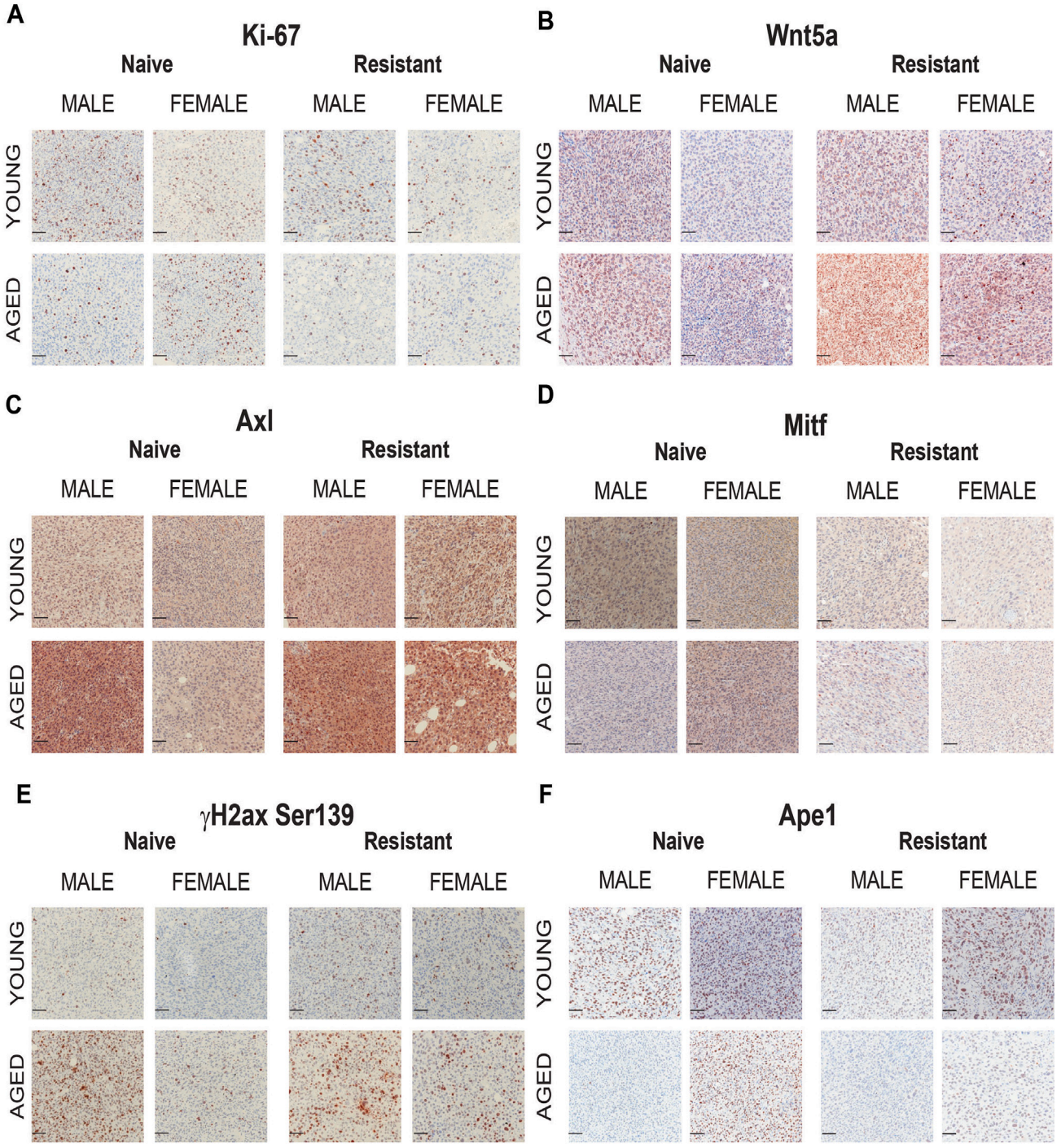

Figure S7. Age and sex of the host microenvironment regulate therapy response and resistance, related to Figure 5

(A) Representative images of Yumm1.7-mCherry primary tumors from mice fed control chow (naive) or BRAFi/MEKi chow (resistant) stained for Ki-67 (n = 4 tumors per group).

(B) Representative images of Yumm1.7-mCherry primary tumors from mice fed control chow (naive) or BRAFi/MEKi chow (resistant) stained for Wnt5a (n = 4 tumors per group).

(C) Representative images of Yumm1.7-mCherry primary tumors from mice fed control chow (naive) or BRAFi/MEKi chow (resistant) stained for Axl (n = 4 tumors per group).

(D) Representative images of Yumm1.7-mCherry primary tumors from mice fed control chow (naive) or BRAFi/MEKi chow (resistant) stained for Mitf (n = 4 tumors per group).

(legend continued on next page)

(E) Representative images of Yumm1.7-mCherry primary tumors from mice fed control chow (naive) or BRAFi/MEKi chow (resistant) stained for γH2ax (Ser139) (n = 4 tumors per group).
(F) Representative images of Yumm1.7-mCherry primary tumors from mice fed control chow (naive) or BRAFi/MEKi chow (resistant) stained for Ape1 (n = 4 tumors per group).
Scale bars show 50 μm. See also Data S1.

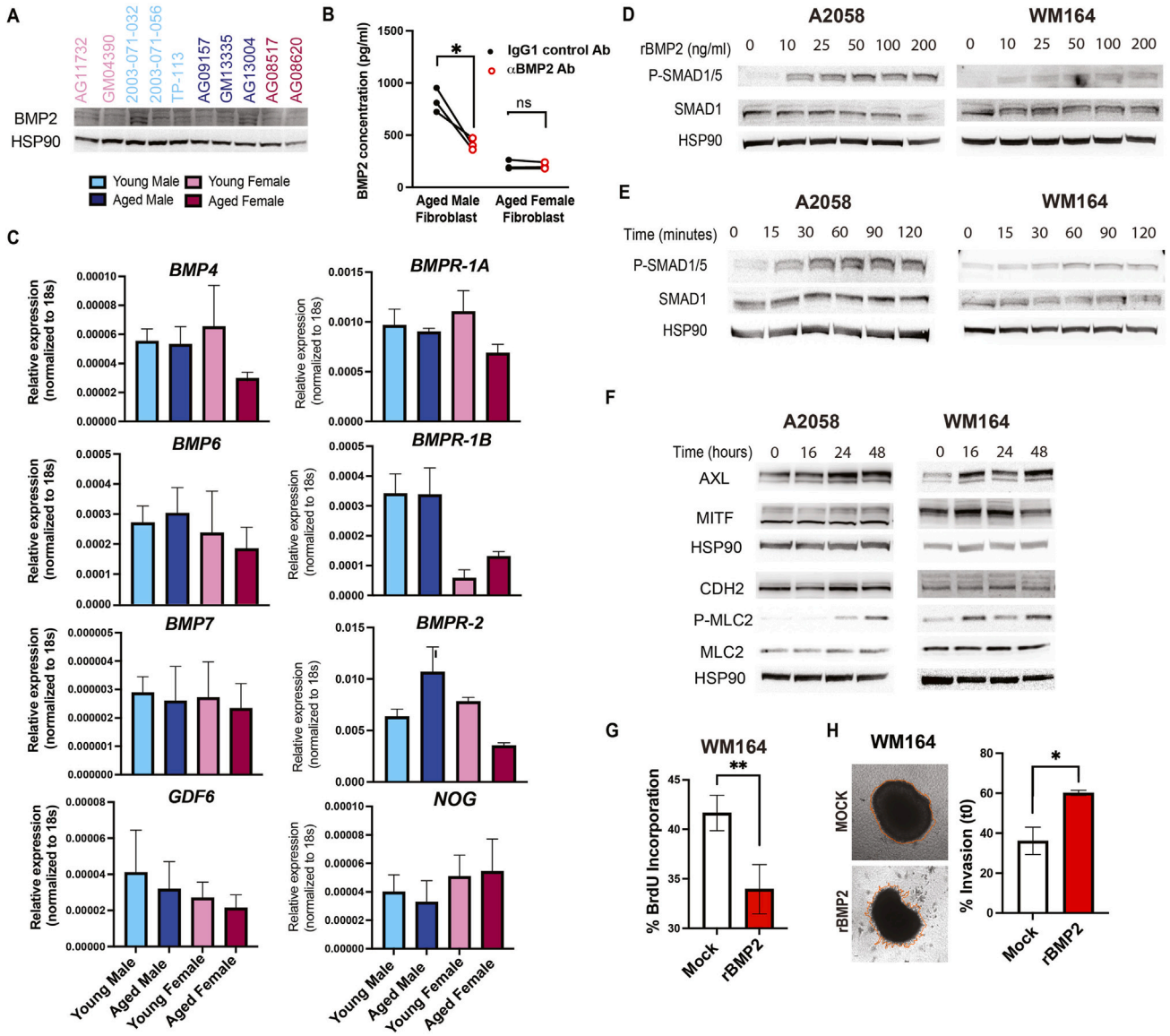

Figure S8. BMP2 in the aged male dermal microenvironment promotes melanoma invasion, related to Figure 6

(A) Immunoblot analysis of BMP2 in age- and sex-stratified fibroblasts. HSP90 was used as loading control.

(B) Relative gene expression of BMP family ligands (*BMP4*, *BMP6*, *BMP7*, and *GDF6*), BMP2 cognate receptors (*BMPR-1A*, *BMPR-1B*, and *BMPR-2*), and BMP2 antagonist (*NOG*) in age- and sex-stratified fibroblasts, normalized to *18s* ($n = 3$).

(C) BMP2 ELISA on conditioned media derived from aged male and female fibroblasts subjected to BMP2 neutralization (aBMP2 Ab) or isotype control (IgG1 control) antibody for 48 h, quantified based on fibroblast cell count ($^*p < 0.05$, $n = 3$).

(D) Immunoblot for recombinant BMP2 (rBMP2) treatment in A2058 and WM164 melanoma lines at indicated concentrations (for 30 min). HSP90 was used as loading control.

(E) Immunoblot for recombinant BMP2 (rBMP2) treatment in A2058 and WM164 melanoma lines at indicated time points (100 ng/mL). HSP90 was used as loading control.

(F) Immunoblot for proliferative (MITF), invasive (AXL, p-MLC2), and mesenchymal (CDH2) markers in A2058 and WM164 melanoma cells treated with rBMP2 (100 ng/mL) or PBS (mock) at indicated time points. HSP90 was used as loading controls.

(G) Quantification of BrdU incorporation in WM164 melanoma cells treated with rBMP2 (100 ng/mL) or PBS (mock) for 48 h ($^{**}p < 0.01$, $n = 3$).

(H) Representative images of spheroid invasion in WM164 melanoma cells following rBMP2 (100 ng/mL) or PBS (mock) treatment for 48 h. Invaded area is outlined in red. Quantification of spheroid invasion represented as percent invasion relative to 0 h ($^{**}p < 0.01$, $n = 3$). Scale bars show 100 μm.

Values are presented as mean ± SEM.

Data S1

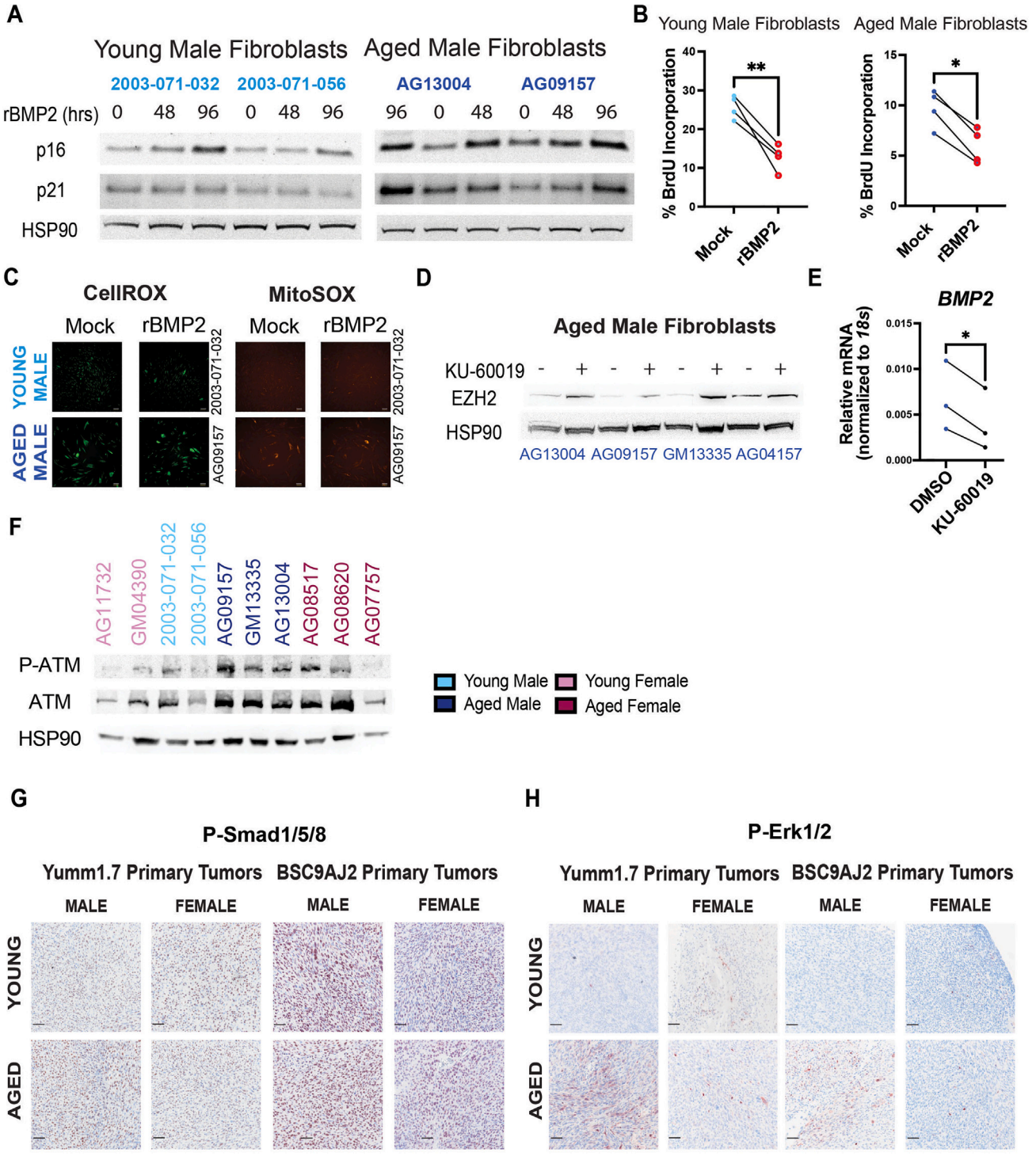

Figure S9. BMP2 in the aged male dermal microenvironment promotes fibroblast senescence, related to Figure 6

(A) Immunoblot for p16 and p21 on young and aged male dermal fibroblasts treated with rBMP2 (100 ng/mL) for indicated time points. HSP90 was used as loading control.

(B Quantification of BrdU incorporation in young and aged dermal fibroblasts treated with rBMP2 (100 ng/mL) or PBS (mock) for 96 h. Represented as percent BrdU-positive nuclei (**$p < 0.01$, *$p < 0.05$, $n = 4$).

(C) Representative images of CellROX and MitoSOX on young and aged male fibroblasts treated with rBMP2 (100 ng/mL) or PBS (mock) for 96 h. Scale bars show 100 μm.

(D) Immunoblot for EZH2 in aged male dermal fibroblasts treated with ATM inhibitor (KU-60019 at 3 μM) or DMSO for 8 days. HSP90 was used as loading control.

(legend continued on next page)

(E) Relative gene expression (RT-qPCR) of *BMP2* in aged male dermal fibroblasts treated with ATM inhibitor (KU-60019 at 3 μM) for 8 days.
(F) Immunoblot for P-ATM (Ser1981) and ATM in age- and sex-stratified fibroblasts. HSP90 was used a loading control.
(G) Representative images of pSmad1/5/8 in Yumm1.7-mCherry and BSC9AJ2-mCherry primary tumors (n = 4 mice per group). Scale bars show 50 μm.
(H) Representative images of P-Erk1/2 in Yumm1.7-mCherry and BSC9AJ2-mCherry primary tumors (n = 4 mice per group). Scale bars show 50 μm.
Values are presented as mean ± SEM.
See also Data S1.

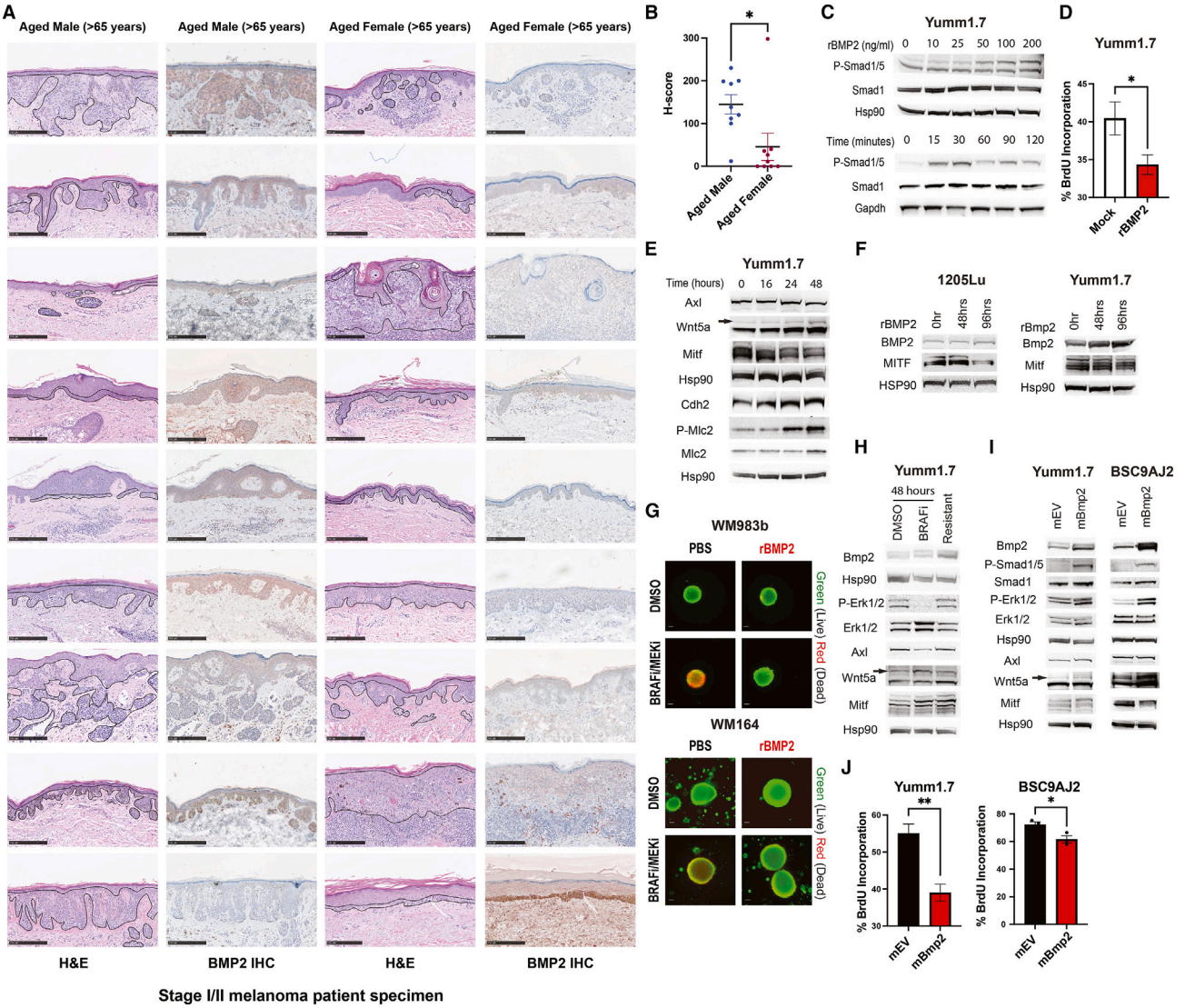

Figure S10. Modulation of BMP2 levels regulates tumor growth and therapy resistance, related to Figure 7

(A) Histological analysis and immunohistochemistry for BMP2 in age-matched stage I/S2 human melanoma patients (>55 years) stratified by sex. Melanoma *in situ* region is outlined in black in corresponding H&E sections. Scale bars show 250 μm. See Table S2 for patient information.

(B) Quantification of BMP2 immunostaining from (A) represented as H score.

(C) Immunoblot for pSmad1/5 and Smad1 in Yumm1.7 melanoma line at indicated concentrations (for 30 min), top and at indicated time points (100 ng/mL), and bottom following recombinant BMP2 (rBMP2) treatment. Hsp90 or Gapdh was used as loading control.

(D) Quantification of BrdU incorporation in Yumm1.7 melanoma line treated with rBMP2 (100 ng/mL) or PBS (mock) for 48 h (*$p < 0.05$, $n = 3$).

(E) Immunoblot for proliferative (Mitf), invasive (Axl, Wnt5a [indicated by black arrow], p-Mlc2), and mesenchymal (Cdh2) markers in melanoma cells treated with rBMP2 (100 ng/mL) or PBS (mock) at indicated time points. Hsp90 was used as loading control.

(F) Immunoblot analysis of long-term treatment with rBMP2 (100 ng/mL) treatment in 1205Lu and Yumm1.7 cells promotes positive feedback for BMP2 and reduction in MITF.

(G) Representative images of analysis shown in Figure 7H for spheroids from WM983b and WM164 melanoma cell lines pretreated with rBMP2 (100 ng/mL) or PBS prior to BRAFi/MEKi or DMSO treatment for 48 h. Dead cells stained red with ethidium homodimer-1. Scale bars show 200 μm.

(H) Immunoblot showing of Bmp2, Erk1/2 reactivation and invasive signature (Axl, Wnt5a [indicated by black arrow]) in BRAFi (PLX4720) resistant Yumm1.7 melanoma line maintained in PLX4720 for over 8 weeks in comparison with DMSO control and PLX4720 treatment (48 h). HSP90 was used as a loading control.

(I) Immunoblot for Bmp2, Erk1/2, and Smad1/5 activation and proliferative (MITF) and invasive (AXL, Wnt5a [indicated by black arrow], p-Mlc2) markers in Yumm1.7 and BSC9AJ2 melanoma lines transduced to express Bmp2-mCherry (mBmp2) or empty vector-mCherry (mEV). HSP90 was used as loading control.

(J) Quantification of BrdU incorporation in Yumm1.7 and BSC9AJ2 cell lines transduced to express Bmp2-mCherry (mBmp2) or empty vector-mCherry (mEV). Represented as percent BrdU-positive nuclei (**$p < 0.01$, *$p < 0.05$, $n = 3$).

Values are presented as mean ± SEM.

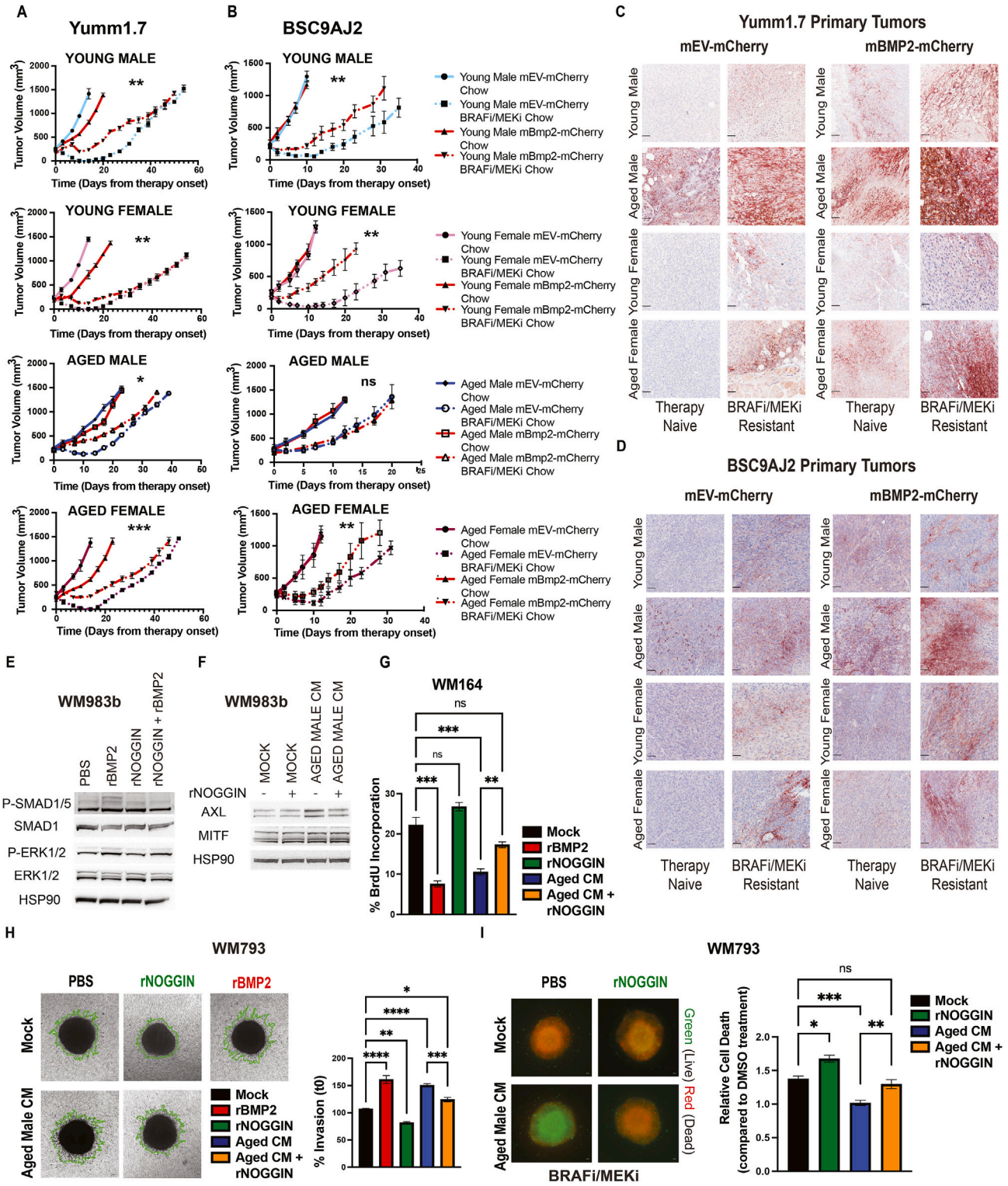

Figure S11. Aged dermal microenvironment or Bmp2 overexpression drives intrinsic resistance to targeted therapy, related to Figure 7

(A) Tumor growth measurement following therapy onset in immunocompetent C57BL/6 young (8 weeks) and aged (>52 weeks) male and female mice injected intradermally with Yumm1.7-mBmp2-mCherry cells or Yumm1.7-mEV-mCherry cells. Mice were randomized to receive diet containing control chow (chow) or BRAFi/MEKi chow *ad libitum* (***$p < 0.001$, **$p < 0.01$, *$p < 0.05$, $n = 6$ mice per group).

(legend continued on next page)

(B) Tumor growth measurement following therapy onset in immunocompetent C57BL/6 young (8 weeks) and aged (>52 weeks) male and female mice injected intradermally with BSC9AJ2-mBmp2-mCherry cells or BSC9AJ2-mEV-mCherry cells. Mice were randomized to receive diet containing control chow (chow) or BRAFi/MEKi chow *ad libitum* (**$p < 0.01$, $n = 6$ mice per group).

(C) Representative images of Bmp2 in primary tumors from (A). Scale bars show 50 μm.

(D) Representative images of Bmp2 in primary tumors from (B). Scale bars show 50 μm.

(E) Immunoblot for SMAD1/5 and ERK1/2 activation in WM983b treated with PBS, rBMP2 (100 ng/mL), rhNOGGIN (0.5 μg/mL), or both for 30 min. HSP90 was used as loading control.

(F) Immunoblot for WM983b melanoma cells assessed for phenotype switch markers (AXL and MITF) following treatment with aged male-conditioned media or normal growth media (mock) in the presence of rhNOGGIN (1 μg/mL) or PBS for 48 h. HSP90 was used as loading control.

(G) Quantification of BrdU incorporation in WM793 melanoma line subjected to PBS (mock), rBMP2 (100 ng/mL), and rhNOGGIN (1 μg/mL) in normal growth media or conditioned media from aged male fibroblasts alone or in combination with rhNOGGIN for 48 h (***$p < 0.001$, **$p < 0.01$, $n = 3$).

(H) Representative images for WM793 spheroid invasion following treatment with PBS (mock), rhNOGGIN (1 μg/mL), and rBMP2 (100 ng/mL) in normal growth media, aged male fibroblast-derived conditioned media alone, or in combination with rhNOGGIN for 48 h. Invaded area is outlined in green. Quantification of melanoma spheroids shown as percent invasion relative to 0 h (****$p < 0.0001$, ***$p < 0.001$, **$p < 0.01$, $n = 4$). Scale bars show 100 μm.

(I) Viability assay on WM793 melanoma spheroids treated with normal growth media or aged male fibroblast-conditioned media in combination with rhNOGGIN or PBS in the presence of 3 μM PLX4720 (BRAFi) and 500 nM PD0325901 (MEKi) or DMSO (mock) for 48 h. Viability was assessed by staining with calcein-AM (green) and ethidium homodimer-1 (red/orange), indicating live and dead cells, respectively. Graph representing relative cell death (total intensity of ethidium homodimer-1 to spheroid area) following BRAFi/MEKi treatment compared with DMSO treatment (***$p < 0.001$, **$p < 0.01$, *$p < 0.05$, $n = 6$). Scale bars show 50 μm.

Values are presented as mean ± SEM.